3-6-2007

Characterization of Intercalated Graphite Fibers for Microelectromechanical Systems (MEMS) Applications

Bryan W. Winningham

Characterization of Intercalated Graphite Fibers for Microelectromechanical Systems (MEMS) Applications

THESIS

Bryan W. Winningham, Captain, USAF

AFIT/GE/ENG/07-25

DEPARTMENT OF THE AIR FORCE
AIR UNIVERSITY

AIR FORCE INSTITUTE OF TECHNOLOGY

Wright-Patterson Air Force Base, Ohio

The views expressed in this thesis are those of the author and do not reflect the official policy of the United States Air Force, Department of Defense, or the United States Government

AFIT/GE/ENG/07-25

Characterization of Intercalated Graphite Fibers for Microelectromechanical Systems (MEMS) Applications

THESIS

Presented to the Faculty

Department of Electrical and Computer Engineering

Graduate School of Engineering and Management

Air Force Institute of Technology

Air University

Air Education and Training Command

In Partial Fulfillment of the Requirements for the

Degree of Master of Science in Electrical Engineering

Bryan W. Winningham, B.S.E.E.

Captain, USAF

March 2007

AFIT/GE/ENG/07-25

Characterization of Intercalated Graphite Fibers for Microelectromechanical Systems (MEMS) Applications

Bryan W. Winningham, B.S.E.E.
Captain, USAF

Approved:

/signed/	6 Mar 2007
Maj LaVern A. Starman, Ph.D (Chairman)	date
/signed/	6 Mar 2007
LtCol James A. Fellows, Ph.D (Member)	date
/signed/	6 Mar 2007
Dr Guna S. Seetharaman (Member)	date

AFIT/GE/ENG/07-25

Abstract

Research was accomplished to characterize the electrical and physical characteristic changes of the Thornel® P-100 carbon fiber when intercalated with 96 % sulfuric acid. This research incorporated the use of microelectromechanical systems (MEMS) structures for testing purposes. MEMS were used to allow the testing of carbon fibers in an isolated micro-scale environment with mathematically proven physical models. The MEMS structures simplified the mathematics to characterize the carbon fibers' physical movement. Six fiber variants were tested during this research. The original fiber was one of the samples and was desized at 400 °C for 30 minutes in air. The rest of the fibers came from the desized original fiber and were modified in different ways. Three lengths of fiber tow were oxidized in 1 M nitric acid at 0.5 Amps for 30 seconds, 1 minute, and 2 minutes. Two other samples were detreated at 1150 °C in a vacuum for one hour prior to their nitric acid treatments of 1 and 2 minutes.

Sulfuric acid is a very corrosive agent and reacts to most materials. Throughout this research, that has been the key issue. The fibers were to be mounted onto a MEMS die, placed into a chip carrier, sulfuric acid added, the chip carrier sealed and testing accomplished. The methods and approaches that were accomplished to complete this task are discussed. Many methods of mounting carbon fibers to withstand sulfuric acid ended with limited degrees of success. Some testing of fibers in sulfuric acid was completed. MEMS structures created using the PolyMUMPs process, were designed with an inset trench that 10 μm diameter carbon fibers could be mounted into for testing, this reduced the amount of coverage required to bind the fiber in place. The original and five anodically oxidized fibers were inspected with a scanning electron microscope (SEM), studied with Raman spectroscopy, and small signal responses were measured from 20 Hz to 1 MHz.

Acknowledgements

With respect to completing this research there are many people that I owe a debt of gratitude. My thesis advisor, Maj LaVern Starman, who has been a great sounding board and aid to my research. Maj Glenn Kading with whom I have worked closely and has taught me a lot. Dr. Daniel Felker, who's knowledge of chemistry has assisted me in many ways and protected me from my own zealousness and naivety. Dr. Peter Sherwood and Dr. Tiejun Wang of Oklahoma State University for the treatment of the carbon fiber samples for this research. I would also like to thank Benji Maruyama, of the Air Force Research Lab (AFRL) for his support and assistance in coordinating the use of resources at the AFRL Materials lab. I must also thank Bill Tropp, Richard Patton, and Kevin Leedy for their help in the laboratory making it possible for me to forward my research.

Bryan W. Winningham

Table of Contents

Page

List of Figures

List of Tables

List of Acronyms

Characterization of Intercalated Graphite Fibers for Microelectromechanical Systems (MEMS) Applications

I. Introduction

The military and industry at large are always looking for viable options to use microelectromechanical systems (MEMS) in electronic devices to reduce both weight and power consumption. Graphite, which is a form of carbon, is a highly researched material; however, the intercalation of carbon, its effect on force and impedance has received limited research. Carbon has an extremely high heat tolerance and its resistance can be altered with intercalation, the embedding of ions in its atomic structure. When graphitic carbon is intercalated, it is often referred to as graphite intercalation compounds (GIC) [1]. L. Vogel wrote an article describing carbon fibers intercalated with antimony pentaflouride achieving conductances that were more than 40 times greater than the original pristine fibers and 70 % greater than copper [2].

Through the process of completing this thesis, research was accomplished to characterize the electrical and physical characteristic changes of intercalated carbon fibers and incorporated the use of MEMS structures for testing purposes. The use of MEMS allowed the testing of carbon fibers in an isolated micro-scale environment with mathematically proven physical models that simplified the mathematics to characterize the carbon fibers. To accomplish this research, an electrolysis voltage was applied to the carbon fibers using sulfuric acid as an intercalant to create GICs. These GICs were then biased by a small signal voltage to examine the induced effects, i.e. physical alteration and electrical characteristics.

Successful characterization of intercalated graphite opens several research initiatives by providing a building block for multiple Air Force Research Labs (AFRL)

and Air Force Institute of Technology (AFIT) research efforts. This thesis provides the Air Force with an advanced understanding of intercalated graphite material which has yet to be fully appreciated in the military or commercial sector. Little imagination is required to see their usefulness in space assets, unmanned aerial vehicles, and aircraft sub-components.

1.1 Graphite

Graphite is one of three forms of carbon: diamond, graphite, and fullerenes. The structures of diamond and graphite are closely related. Diamond has four carbon to carbon covalent bonds per atom, i.e. sp^3 (tetrahedral) hybridization, which holds the structure together with great strength and rigidity. Whereas, graphite has three carbon to carbon covalent bonds per atom, i.e. sp^2 (triganol) hybridization, with the fourth electron forming a π-bond that causes a weak van der Waals force between the layers of graphene sheets. These bonds result in carbon atoms that are arranged in a 2-dimensional hexagonal pattern, as shown in Figure 1.1. The atomic distance between carbon atoms (d_{c-c}) on the same plane in graphite is 142 pm while the interplanar distance, d_o, is 335 pm. The interplanar distance makes it easy to remove graphite in layers and allows the two neighboring planes to slide over each other. The graphite structure also results in a material that can conduct both electrically and thermally along the 2-D a-plane, i.e. along the a_1 and a_2 plane shown in Figure 1.1. However, orthogonal to this plane, the electrical resistance is high with reduced thermal conductivity. Electrically, carbon is an amphoteric, type four element and is able to accept and donate electrons during reactions with other elements, altering its conductivity [1, 3]. Carbon fibers have many ways in which they are oriented but the one being researched, the `Thornel`® P-100 has its a-plane oriented radially from the fiber core similar to the radius of a circle [4]. Fullerenes are made up of carbon atoms bonded together into a spherical, egg or tubular shape and include carbon nanotubes and buckyballs.

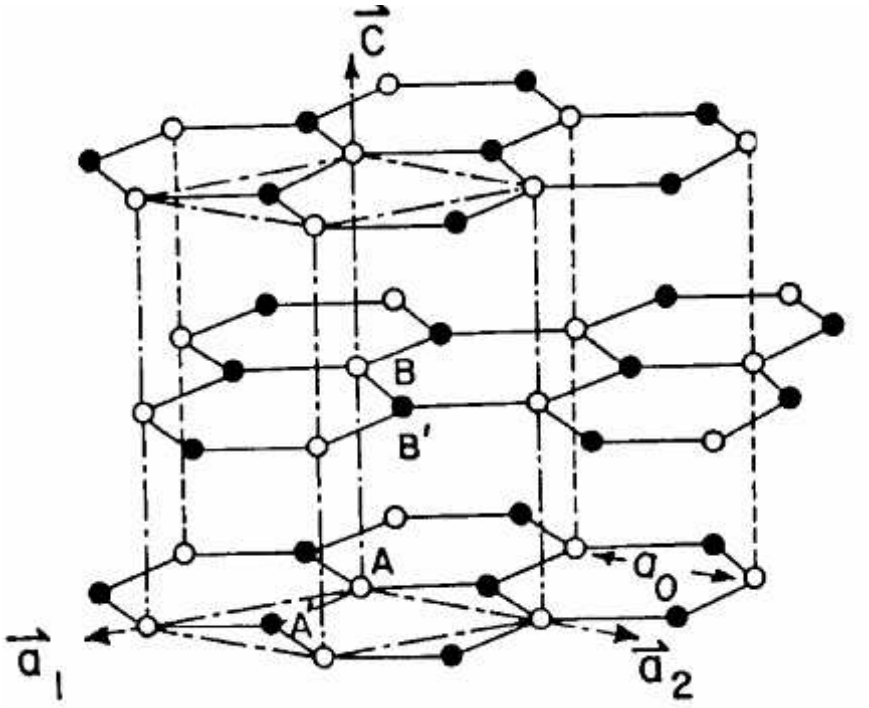

Figure 1.1: Hexagonal graphite. The a_1 and a_2 vectors define the plane where the graphite layers exist, the c-vector represents the direction on which the layers of graphene are stacked and the layers are stacked in a ABAB type pattern, i.e. the layers alternate in the positioning of the carbon atoms [5].

1.2 Graphite Intercalation

The most common form of graphite, hexagonal graphite, has an atomic layer pattern of ABAB in the XY plane as shown in Figure 1.1. There are alternate forms of graphite but will not be discussed further. The covalent bonds between the planar carbon atoms, a-plane of Figure 1.1, are extremely hard to break. Thus, one method to create graphite compounds after the graphite structures are already constructed is through intercalation. Intercalation modifies the p-bonds between planar layers, along the c-vector. Graphite is an ideal 2D host for the intercalation of various materials which causes molecular changes in the lattice structure [1, 5].

Intercalation occurs when guest atoms or molecules enter a layered host material and ionically or covalently bond with them creating interstitial pocketed layers of guest. Ionic intercalation is the most studied area and allows for the greatest

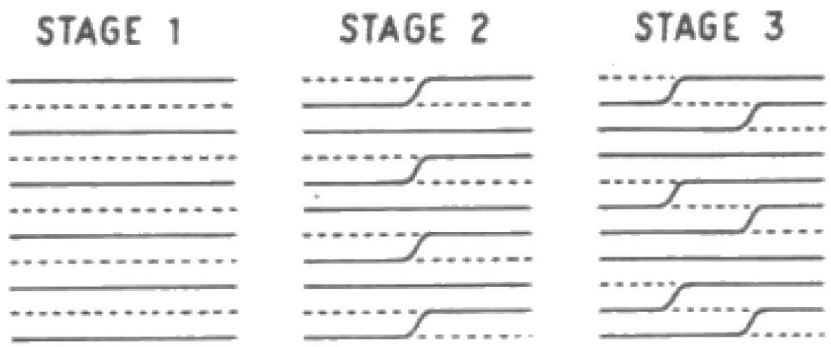

Figure 1.2: Stage 1 through 3 carbon intercalation, note the layers of carbon (solid lines) between each layer of intercalant (dashed lines) which are located in galleries [1]

flexibility in modification of graphite's electrical conductivity by altering the Fermi energy of the graphite. In the case of carbon, there are many materials and methods that can be used to cause carbon to intercalate with other substances. Intercalation often occurs spontaneously for various intercalants with no additional energy being injected into the system. It can also be induced, endothermically, by almost any process that causes enough energy to be put into the system that is large enough to cause carbon and another material to interact, i.e. donate and receive electrons. This paper is limited in scope to the latter, endothermic reactions [1].

Intercalation is often referred to by the stage of the intercalation. A stage is the number of layers of carbon located between pockets of the guest molecules or atoms. The lower the stage number, the more energy has been applied and the fewer layers of carbon exist between intercalants. Figure 1.2 shows stages ranging from 1 to 3, the solid lines represent graphite layers and the dashed lines are the guest materials located in galleries. When graphite is between stages of intercalation, the atomic structures of the guest material are loosely packed and disorganized. As the energy is increased and approaches the next stage, the guests molecules shift within the graphite and fill the gallery for the next stage. One widely held belief is that when the material transitions between stages, the guest material is forced out of the graphite and must re-enter in the appropriate layer for the next stage. Several

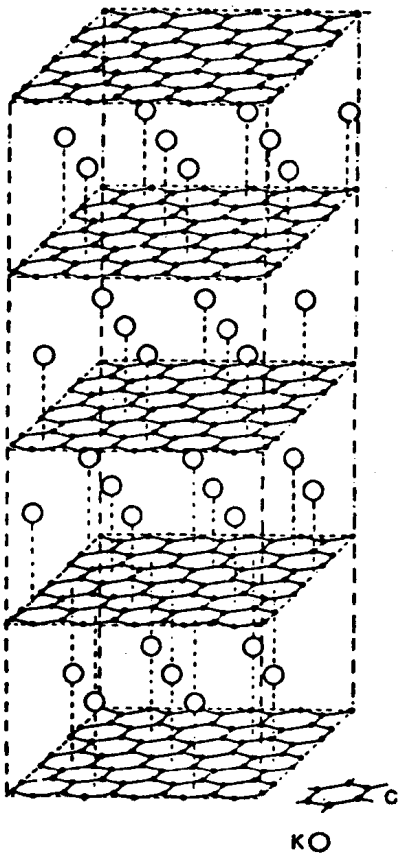

Figure 1.3: Stage 1 intercalation of potassium (K) into layers of carbon, hollow spheres represent potassium atoms and the hexagonal structure is comprised of carbon atoms [5]

experiments were accomplished that tested this theory and proved that intercalants do not leave the carbon material to transition between stages. Thus, reorganization takes place internally during the transition between stages [1]. A 3D portrayal of potassium stage-1 intercalation is represented in Figure 1.3.

1.3 Summary of Relevant Research

Minimal investigation has been accomplished into the use of intercalated carbon as an actuator. Koyama performed research on highly oriented pyrolytic graphite pillars using lithium as an intercalant and experienced a peak strain of 6.7 % with

a 10 MPa load in the *c*-plane direction. His research also provided insight into how changes in load effect the strain that is experienced in graphite intercalants [6].

G. Kading performed electrolytic intercalation of H_2SO_4 (sulfuric acid) into individual carbon fibers and calculated the strain induced into these fibers based on the voltage and current applied. He also performed some initial electrical impedance testing of these fibers using electrolysis and a small signal (AC) voltage. His scope was limited to determining if further research was warranted into the potential use of intercalated carbon as a MEMS actuator [7].

In 1997, research was accomplished on a "graphite-bromine residue compound based on highly oriented pyrolytic graphite" (HOPG) and was intercalated to stage 2 in air at room temperature with bromine vapor. The sample was then exposed to a 150 W light bulb through a fiber optic cable. This stimulation resulted in uniform expansion in the c-plane [8]. Salib's experiment required the intercalation of the intercalant prior to the test with no further addition of intercalant during the experiment. Although Salib's results were not consistent, they further demonstrated the potential applicability of intercalated carbon material as an actuator.

1.3.1 Carbon Nanotube Actuators. Carbon nanotubes (CNTs) are another material that holds potential as a MEMS actuator. Single-walled CNTs have a diameter of 0.4 to 3 nm and multi-walled CNTs have outer diameters of 2 to 100 nm. At this point, most of the research into the use of CNTs as actuators is limited to large macro devices made up of hundreds to thousands of fibers that are formed on a matte and is referred to as "buckypaper." In 1999, the first actuator made from buckypaper was cited by Baughman when he submerged two sheets of buckypaper bonded together by double sided tape into 1 M NaCl and biased the two sides with a few volts [9]. Since then, a lot of research has been accomplished and advancements have been made. Now carbon fibers are being bonded together with polymers and larger deflections are being reported as can be seen in Figure 1.4.

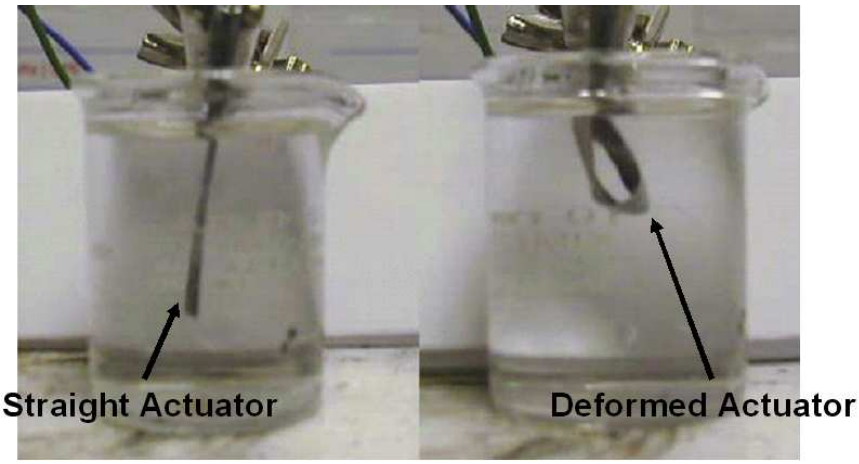

Figure 1.4: Two layers of single walled CNTs bonded with epoxy and separated by an insulating material and submerged in 2 M NaCl solution. The left side picture was taken before 10 volts was applied between the layers, after several minutes irreversible movement of the actuator as seen on the right side occurred [10].

1.4 Assumptions

From the outset of this research, certain assumptions were made. First, all carbon fibers were identical and came from the same production run. James Gaeier stated in 1988 "that pitch based fibers from a single batch have homogenous properties within a few percent" but that this is not necessarily true between fibers from different production runs [11, 12]. This assumption reduced the amount of data collection on pristine de-sized fibers throughout this process. Sizing is a material applied to a fiber that holds all of the fibers in a tow i.e. a bundle of carbon fibers. Second, the carbon fibers used for this research are unaffected by the mounting process required in preparation for testing.

1.5 Scope

The scope of this research is limited to the mesophase pitch based Thornel P-100 carbon fiber currently produced by Cytec and formerly produced by BP Amoco. The carbon fiber was provided by the AFRL. Some of the fiber was sent to Oklahoma State University where five different fiber treatments were accomplished. The fibers were to then be intercalated with H_2SO_4 to study the DC and small signal impedance

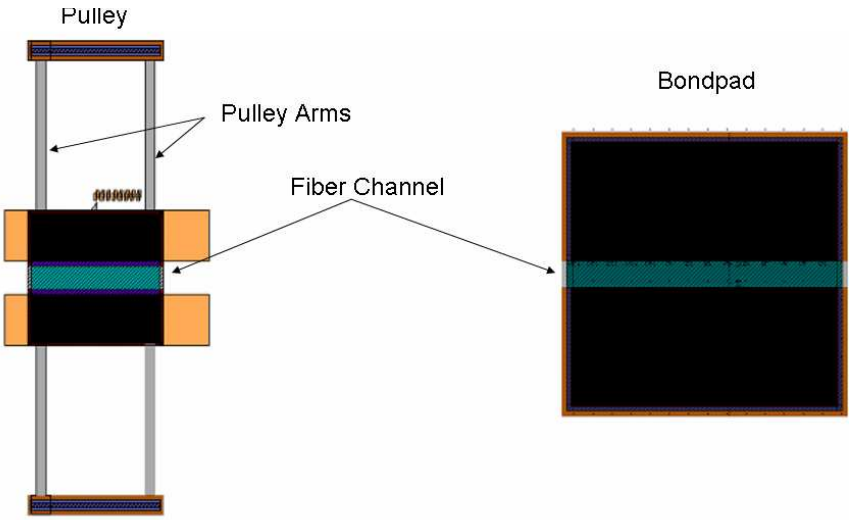

Figure 1.5: Pulley and bondpad testing system for Thornel P-100 carbon fiber. The middle layer is a channel for the fiber to set in and is cupped into the surface

characteristics of each fiber. The testing was conducted at room temperature under normal air pressure.

1.6 Methodology

The original intent of this research was to utilize test structures in which individual carbon fibers could be mounted onto and tested using the MEMSCAP corporations polysilicon multi-user MEMS Processes (PolyMUMPs) to create them. The PolyMUMPs process is a "three-layer polysilicon surface micromachining process" that has two releasable structural layers [13]. Two types of structures were designed for testing the samples. First, a force device consisting of a pulley and a bond pad shown in Figure 1.5. This would provide a means to measure the pulley displacement as a result of the fiber intercalation and then calculate the force produced. Calculations using the device design and material properties along with basic mechanics were used to calculate the force generated by the carbon fiber. The second device had four conductive contacts equally spaced from each other for a four-point probe test. This device was designed to provide the data needed to calculate the impedance

of intercalated carbon fibers with an applied electrolysis voltage and a small signal (AC) voltage.

Once the PolyMUMPs wafers returned from MEMSCAP, the carbon fibers were to be secured onto the test devices with conductive silver epoxy and permanently mounted with metal. The wafer was then to be placed in a chip carrier and wire bonded to the external pins to improve testing efficiency. The intercalant material would be inserted into the chip carrier then the chip carrier sealed making the fibers ready for testing and data collection. This would have led to the use of both Coventorware for mechanical modeling and other computer software programs to determine the mechanical force and impedance models for the `Thornel`® P-100 carbon fibers intercalated with H_2SO_4.

1.7 Research Limitations

This research endeavor had numerous limitations. First, the results of this research might only be applicable to the fibers tested. This is due to the use of commercial carbon fibers. Carbon fiber manufacturing is not regulated or controlled and there is no requirement that manufacturers announce process changes as they are highly guarded industrial secrets. Even if the production process was not altered, fibers from different production runs are not necessarily identical [11]. Second, long term duration tests were not accomplished, i.e. how long the fibers remain intercalated and the resulting effectiveness decay rate.

1.8 Main Results

Many efforts were made to identify a procedure to mount these fibers onto MEMS structures in a reliable and repeatable manner that could withstand the effects of sulfuric acid. Standard photolithography techniques were applied and produced the best results but still did not achieve repeatability. This thesis covers the different methods that were performed to try and secure the fibers in place without being released when exposed to 96 % H_2SO_4. `Epo-Tek`® H-27D conductive epoxy was used

throughout this process to bond fibers but is reactive to sulfuric acid. Many of the methods attempted were meant to protect the epoxy from the acid.

This research resulted in the testing of six types of Thornel® P-100 carbon fibers. One of the fibers was as received from AFRL and was the base from which all the other fibers came. These original fibers were de-sized by being heated to 400 °C for thirty minutes in air. The other fibers were anodically oxidized in nitric acid from thirty seconds to two minutes and some were heat treated in a vacuum to 1150 °C to detreat, i.e. remove manufacturer's carbon fiber coatings, prior to the anodic oxidation. These fibers were studied using a scanning electron microscope to observe the treatments effect on the fiber surface. These fibers were then studied with Raman spectroscopy to identify the differences between the fibers. The anodically oxidized fibers showed signs of a decreased crystal structure symmetry. This loss of symmetry was attributable to the fibers treatment. The fibers were then tested with a resistance, capacitance and inductance meter in a four point probe type measurement to identify the impedance of the fibers when driven with a frequency from 20 Hz to 1 MHz. All of the fibers had fairly stable phase shifting of the AC signal. The resistivity of each fiber at the tested frequencies were calculated.

1.9 Summary

This chapter provided a general discussion of carbon intercalation and briefly touched on carbon structure and reasons for its high conductivity. A brief summary of relevant research was also accomplished. Then some specifics about the research process were discussed, such as the assumptions, scope, methodology, research and limitations, culminating in the research results. Chapter two will provide a literature review of carbon and MEMS actuators. Chapter three covers graphite intercalation and more importantly intercalation of carbon fibers. Chapter four will discuss the modeling, simulation, design and fabrication. The results and analysis are presented in Chapter 5. The final chapter, will discuss the conclusions and recommendations.

II. Literature Review of Carbon and MEMS Actuators

Microelectronic components require the use of micrometer-size actuators that are capable of providing significant force and are reversible. This thesis will explore the response of a Thornel® P-100 carbon fiber with 6 different types of surface treatments to sulfuric acid as an intercalant modeling the electrical response of these fibers over a broad range of frequencies.

2.1 Scope of the Review

The intercalation of carbon had great research interest from the 1970s to 1991. After that point, only minimal research was accomplished. This dropoff can be partially explained by the discovery of carbon nanotubes by Iijima [14]. The literature review includes some research that explored the use of GICs as actuators or related areas such as their ability to expand or contract.

2.2 Methodology

Research will be accomplished experimentally by using individual carbon fibers that will be mounted onto silicon wafers with surface micromachined structures. Surface micromachining is defined as "building up and patterning thin film layers to realize the desired structure on the surface of the wafer" [15]. This micromachining process will be accomplished using the Polysilicon Multi-Users MEMS Process (PolyMUMPs) through MEMSCAP [13].

2.3 Micro-Electro-Mechanical Systems (MEMS) Actuators

Micro-Electro-Mechanical System (MEMS) actuators are divided into two categories: thermal and electrostatic. Thermal actuators use material expansion as a means to cause movement and apply a force. Electrostatic actuators use the attraction between two materials with opposite electric charge to drive movement, eg. a micromirror. These two actuator types have different characteristics and apply different forces. The thermal actuator uses low voltage and high currents to heat the structure causing expansion and deformation around a pivot point. The electrostatic

(a.) Single arm thermal actuator

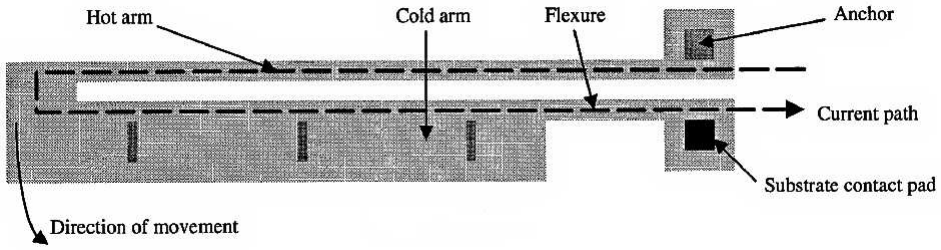

(b.) Dual arm thermal actuator

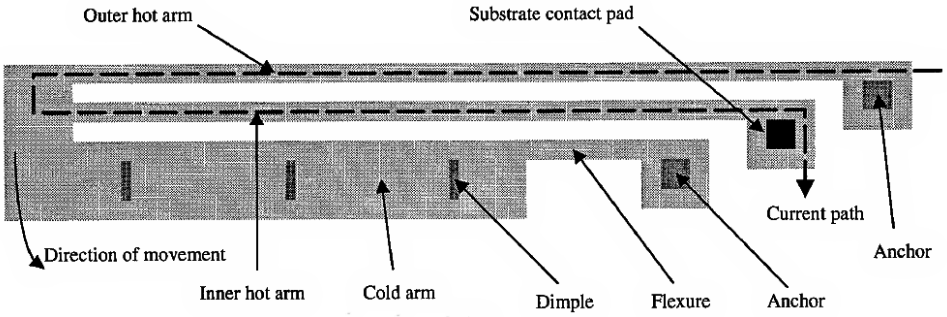

Figure 2.1: (a) Diagram of single armed horizontal thermal actuator components, (b) Diagram of dual armed horizontal thermal actuator components. In both diagrams, the hot arms carry a high current density due to their cross-sectional area and the cold arms have a low current density for the same reason and so don't become as hot [16]

actuator uses a high voltage but virtually no current and causes the two surfaces to draw toward each other depending on the voltage and actuator design [16]. These are introduced here to identify currently employed methods of actuation in MEMS.

2.3.1 Thermal Actuator. Thermal actuators can be designed either vertically or horizontally. In the horizontal style, the movement is in a lateral direction from side to side and can consist of a single or double hot arm horizontal actuator as pictured in Figure 2.1. Movement is stimulated by the flow of current through the hot arm which creates heat, due to the small cross sectional area. This heat causes expanding or lengthening of the hot arm which applies a force to the cold arm causing movement around the flexure. In the single arm actuator, the cold arm

is much wider than the hot arm. Although, the flexure in Figure 2.1 does not make this clear, the flexure must also have a greater cross sectional area than the hot arm to ensure that the current density through it is not too high causing excessive heating and damage. This problem is avoided in the dual arm actuator since current no longer flows through the flexure; but it has other needs that must be accounted for. In both cases, the cold arm has to be kept wide so that it remains stiff so that all the bending force is transferred to the flexure [16]. The double arm actuator produces about 80 % more force and has a higher frequency response than the single arm actuator. The devices constructed by Burns were able to produce 11.5 μN for single arm and 20.5 μN for double arm actuators. The difference in force is partially explained by the lack of heating in the flexure since no current flows through it. In Figure 2.2, a single arm horizontal actuator can be seen where the expansion of the hot arm is easily observed and the arm is deflected approximately 5 μm. The vertical thermal actuator operates in a similar manner and will not be covered any further.

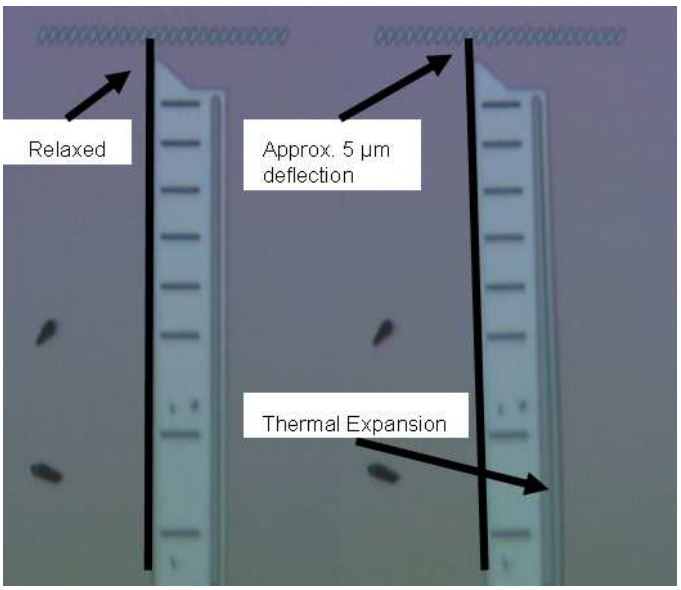

Figure 2.2: Microscope image of 250 μm single arm thermal actuator in motion. The left side shows the actuator at rest and the right image shows the actuator after displacement of approximately 5 μm.

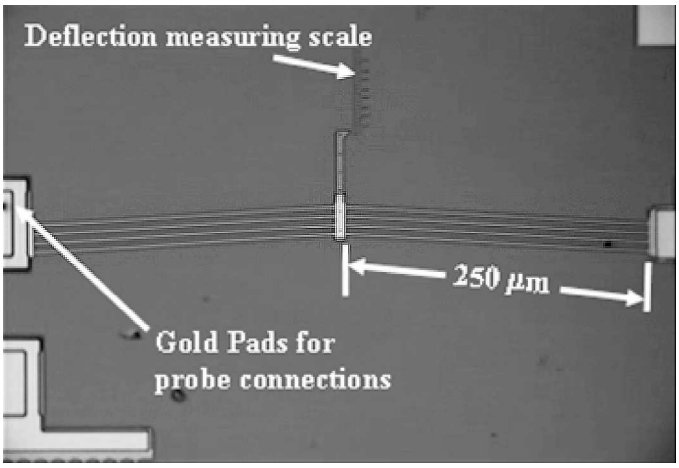

Figure 2.3: PolyMUMPs actuator with arms made up of four 250 μm long chevrons [17].

Another method to activate a thermal actuator is through the use of intense light, i.e. a laser, to heat the arms causing movement. Figure 2.3 shows a thermal actuator that can be activated by applying either an electrical current or laser. When used electrically, this actuator operates like the other thermal actuators by running the current through the arms between the anchors located on either side of the device. If the device to be actuated is sensitive to electricity, a laser can be focused on the actuator arms causing them to heat up and expand. This device consists of an actuator body surrounded by two sets of four 250 μm long chevron shaped arms which are anchored to the substrate at the gold contacts [17].

2.3.2 Electrostatic Actuators. Electrostatic actuators act like parallel plate capacitors. When a voltage potential is applied to two separate conductive plates separated by a dielectric, such as air, nitrogen, or nitride they are attracted. Allowing them to approach each other is a method to actuate a device, although the goal is to keep them from touching. It is not uncommon for these devices to require several hundred volts to operate. Another issue with electrostatic actuators arises from their non-linearity. After the mobile layer has traveled one third of the distance from its resting position toward the fixed plate, the non-linear magnetic force causes the

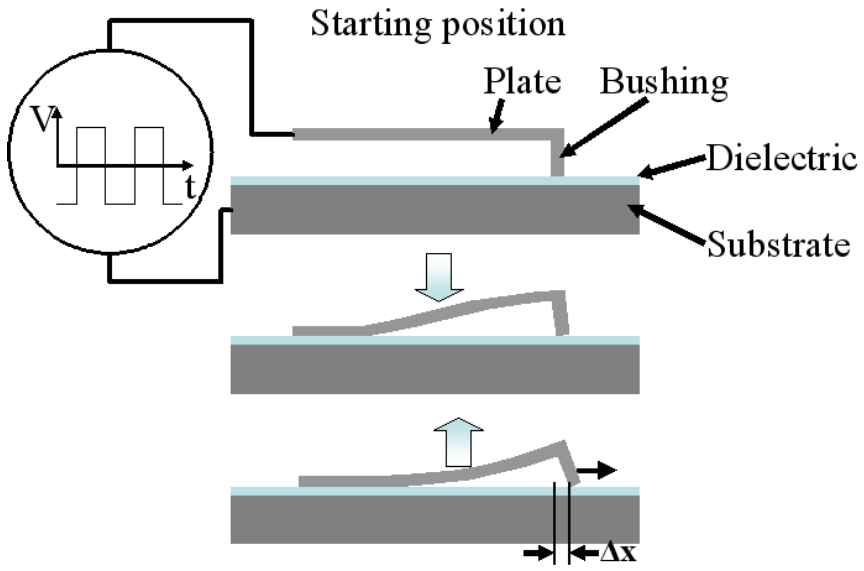

Figure 2.4: Scratch drive actuators operates when driven with an alternating square wave which is applied to the plate and substrate that are isolated by a dielectric surface. The electrostatic force causes the plates attraction and release from the dielectric surface causing the bushing to pull the structure forward by Δx per pulse cycle [16].

two surfaces to attract each other very quickly [15]. Types of electrostatic actuators include micromirrors, comb drives, cantilevers and scratch drives. A scratch drive actuator uses an applied square wave voltage to operate, as shown in Figure 2.4. A potential between the substrate and plate is increased causing the plate to pull down toward the substrate and forces the bushing forward. After peaking, the potential decreases, allowing the plate to momentarily relax pulling away from the substrate. The bushing then contracts on the non-conductive surface, pulling the actuator forward by a distance Δx. As the voltage changes polarity, the scratch drive actuator repeats the proces again [16].

2.4 Related Carbon Actuators Using Intercalation

Currently, minimal research is being published that uses carbon fiber intercalation as a component of microelectronics or MEMS. Three citeable cases of research can be applied to MEMS and all of them created actuators with carbon but only one used carbon fibers. The latest research by Koyama involved highly-oriented pyrolytic graphite and the intercalation of lithium [6]. The most applicable work was completed at AFIT by Kading and explored the possibility of using the intercalation of carbon fibers as a MEMS actuator [7]. The final article was written by Salib on "Optomechanical actuation using intercalated graphite" [8].

2.4.1 Electrochemical Intercalation of HOPG. In 2006, an article was produced that intercalated lithium into highly oriented pyrolytic graphite (HOPG) and studied the percent strain in the *c*-plane as defined in Figure 1.1 with different loads and voltage potential. Koyama created pillars of HOPG by laser etching a HOPG sample: reference Figure 2.5 for the following device description. Lithium is highly anisotropic in its intercalation into HOPG and goes into the space between layers of graphene slowly. To speed the reaction, Koyama created pillars in the HOPG with laser etching. Due to system limitations, the product was 700 μm wide at the

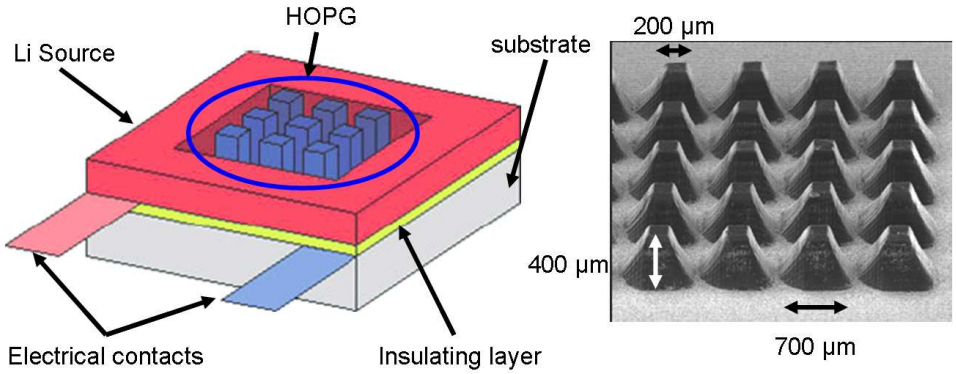

Figure 2.5: Bulk HOPG laser etched into pillars attached to an aluminum oxide substrate by Cu foil and surrounded by a non-aqueous, liquid electrolyte providing contact to the lithium source. The HOPG pillars support the entire load during testing [6].

base, 400 μm tall, and 200 μm wide at the top. His final structure consisted of a vast array of these structures that were mounted on a copper foil onto an aluminum oxide substrate. An insulator was then placed around the HOPG array on the substrate and a lithium source bonded down. A non-aqueous electrolyte solution was placed inside the Li source so as to surround the HOPG pillars [6].

For his experiments, Koyama applied several different fixed loads on top of the pillars and the HOPG was charged and discharged to identify the induced strain. Figure 2.6 shows the results for both the 10 MPa and 100 MPa load. The 10 MPa load test starts with the HOPG charged without intercalation occurring. The polarity is reversed and the HOPG is allowed to discharge at a 10 mV rate up to the dashed line at approximately 24 hours. At that point, the voltage was measured as an open circuit at 0.1 V showing that the HOPG was not saturated with lithium. The voltage polarity was reversed and the system charged at a 0.5 V rate for an additional

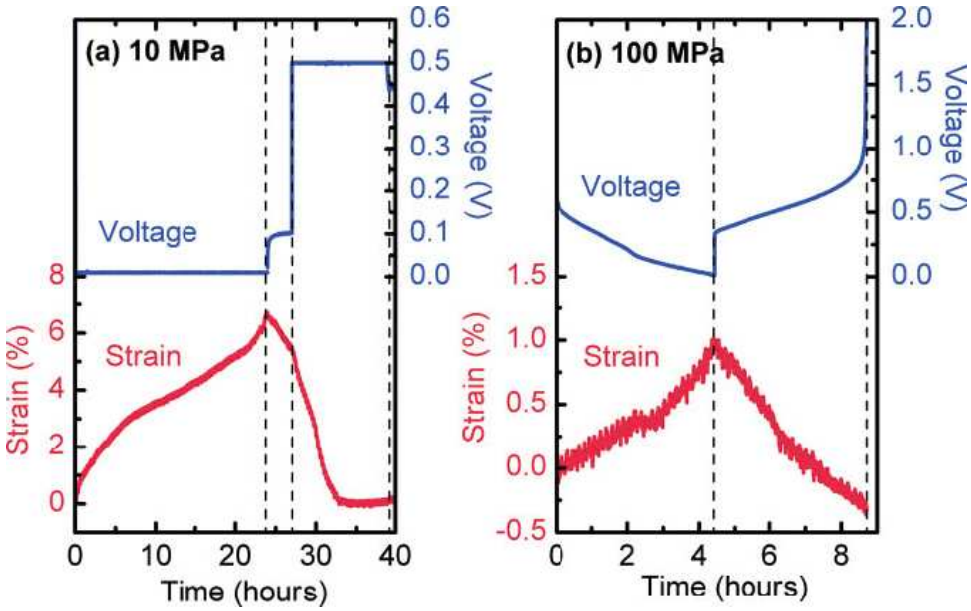

Figure 2.6: Strain versus time and voltage of two samples when discharged and recharged. (a.) Device was allowed to discharge at a constant voltage of 10 mV resulting in the peak strain of 6.3 %. (b.) The test structure was discharged with a constant current, resulting in higher voltages and a faster ramping of the strain which peaked at 1.3 % [6].

10 hours driving the lithium out of the sample and reducing the strain. The peak strain observed was 6.7 %. The 100 MPa load was tested differently, utilizing a current limited discharge. This appears to have sped the process up by allowing the voltage to drop more quickly and resulted in a strain of 1.3 %. When the system was recharged the strain became negative. Koyama tried numerous load forces on his samples, Table 2.1 shows the applied forces and the resulting strain that was observed.

Table 2.1: Maximum percent of strain achieved from lithiated graphite [6]

Load stress	percent strain (%)
10 MPa	6.7
30 MPa	4.3
50 MPa	3.5
100 MPa	1.3
200 MPa	0.7

The data collected delivered a peak of 54.6 % of the theoretical charge capacity of the HOPG when loaded with a 10 MPa stress. This percentage decreased as the load was increased and leaves plenty of room for improvement but is a good step forward into the potential of using HOPG as a *c*-plane actuator. This means that the intercalant spacing within the structure is used to increase the height of the stacked graphene planes.

2.4.2 Carbon Fiber Research. Kading used electrochemical stimulation to drive the intercalation of H_2SO_4 into `Thornel`® P-100 carbon fibers [7]. The research of Metrot and Vogel led him to learn of the Piezo Electro-Chemical Transducer (PECT) effect on carbon during intercalation [18]. Kading then initiated testing on his own to verify this prior research. He went through the process of characterizing the resistance response of `Thornel`® P-100 carbon fibers partially submerged in H_2SO_4 as it was intercalated at voltages from 0 to 1.4 V and frequencies from 40 Hz to 1 MHz. The resistance was stable from 40 Hz to 10 KHz. After that point, the

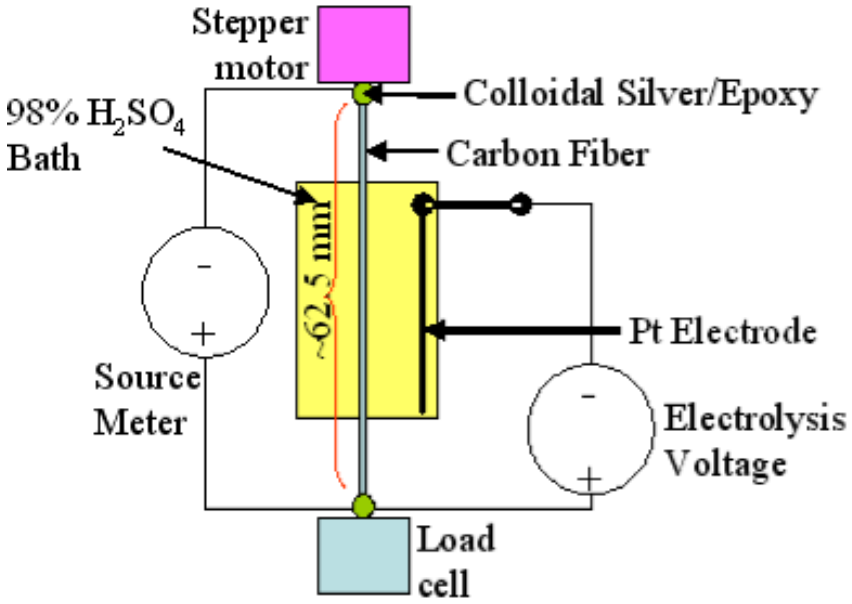

Figure 2.7: Strain test setup for Thornel® P-100 carbon fiber with 32.5 mm of carbon fiber length submerged in H_2SO_4 with a source meter and an applied electrolysis voltage [7].

resistance increased as the frequency increased and experienced a resistance dip after 0.7 V to approximately 1.2 V where the resistance began to rise again.

After this, Kading intercalated Thornel® P-100 carbon fibers with an applied voltage and current in H_2SO_4 to measure the mechanical force. His experiment set-up is shown in Figure 2.7. He used a 62.5 mm Thornel® P-100 carbon fiber but submerged 32.5 mm of it in an H_2SO_4 bath. Due to limitations in the mechanical test set-up, only a portion of the carbon fiber was submerged. Other devices used during the experiment included a load cell that was used to measure the force applied by the intercalated carbon fiber, a stepper motor for removing any slack in the fiber, a platinum electrode to complete the electrical circuit from the fiber, and a source meter to measure the resistance of the carbon fiber [7].

The results of Kading's experiments were promising. When compared to the most efficient MEMS thermal actuators, his PECT device was able to obtain more than ten times the strain per volt. To model his system, he used polysilicon thermal

actuator strain given by

$$\varepsilon \simeq \frac{\alpha V^2}{12\rho K} \text{ (unitless)} \tag{2.1}$$

where the following assumptions were made for the characteristics of the polysilicon. The coefficient of thermal expansion, α, is approximately $2.33x10^{-6}/K$, resistivity, ρ, is approximately $2.3x10^{-5}$ $\Omega{\cdot}m$, and the thermal conductivity, K, has a value between 31 $W/(m{\cdot}K)$ and 100 $W/(m{\cdot}K)$. By assuming constant capacitance, he was able to use

$$\varepsilon \simeq \frac{V\varepsilon_0\varepsilon_r}{d_{ij}EL_0} \text{ (unitless)} \tag{2.2}$$

for piezoelectrics to estimate the strain caused by thermal expansion of the carbon fiber, where E is the Young's Modulus, ε_0 and ε_r are air and material permittivities, d_{ij} is the piezoelectric modulus of the material, and L_0 is the original length of the material in question and in this case is 32.5 mm. Figure 2.8 compares the voltage and strain per volt for the carbon fiber actuator and many of the more common substances in use today. As illustrated, the carbon fiber exceeds all of them. The

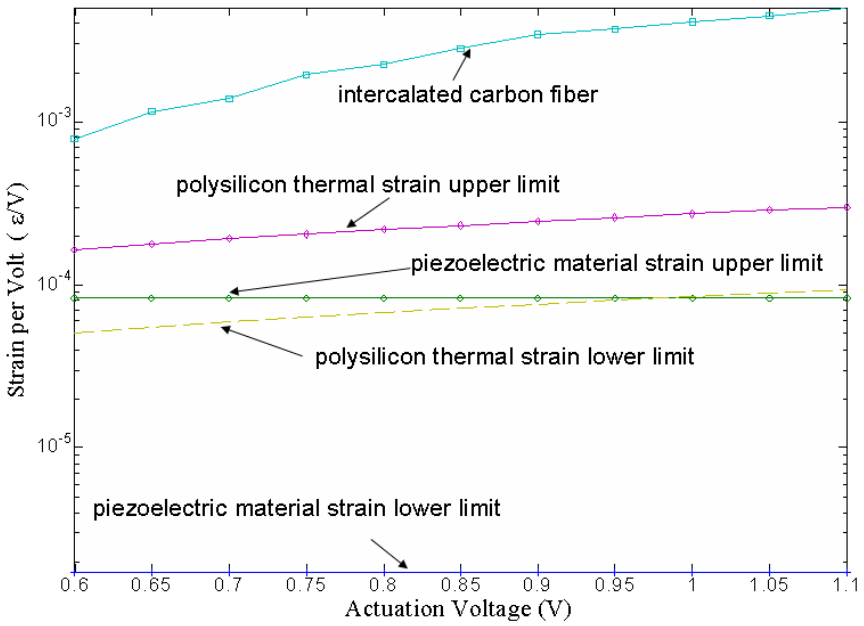

Figure 2.8: Strain versus voltage for test device (PECT) and common actuation materials [7].

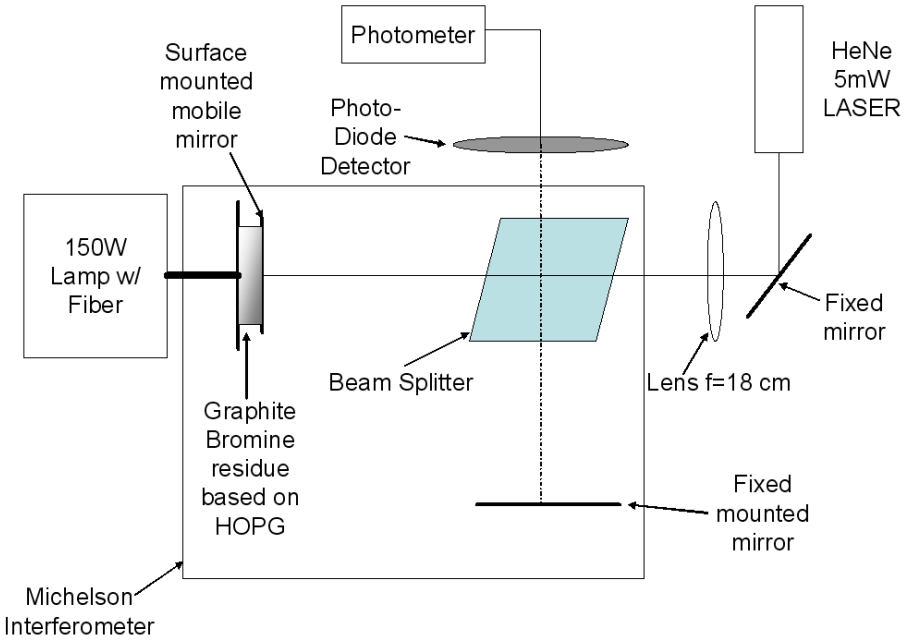

Figure 2.9: Salib Br_2 intercalated HOPG optomechanical testing apparatus [8].

results were most likely skewed down since the entire carbon fiber was not exposed to the sulfuric acid, potentially reducing the effectiveness of the intercalation [7].

2.4.3 Optomechanical HOPG Research. Salib approached his research from another direction and was interested in stimulating his device by optomechanical means. Salib used a rectangular piece, 4.2 x 3.3 x 1.0 mm, of highly-oriented pyrolytic graphite (HOPG) and intercalated it with bromine vapor at room temperature to attain stage 2 intercalation with 19 mol % Br_2. Salib was hoping to show his technique's viability as a switch and obtaining consistent results was a high priority. Therefore, he was careful to ensure that he did not overdrive his carbon and destroy it. Salib's test apparatus (Figure 2.9) included a 150 W tungsten halogen light bulb with a 3 mm diameter fiber optic cable directing the light onto the surface of the block of intercalated carbon with an effective light energy of 400-500 mW. On the opposite side of the carbon, a light weight flexible mirror was placed on the surface. A 5 mW He-Ne laser was used as a light source for the mirror to allow an

interferometer to measure the interference fringes and calculate the change in HOPG thickness [8].

Salib was successful in his endeavors to cause the carbon to expand on the c-plane, i.e. the plane perpendicular to the carbon layers, by approximately 4 μm with a rise/fall time of 15 s. He observed that the mirror remained flat; implying that the carbon expanded uniformly even though the light source did not illuminate the entire test sample. He also observed that with identical light input cycles the expansion was not consistent, as shown in Figure 2.10. This led him to conclude that optomechanical stimulation of his device was not fast enough or consistent enough to become a viable option as a switch. One of his final statements included a commentary that if a larger expansion or a quicker response was desired, apply an electromechanical stimulation.

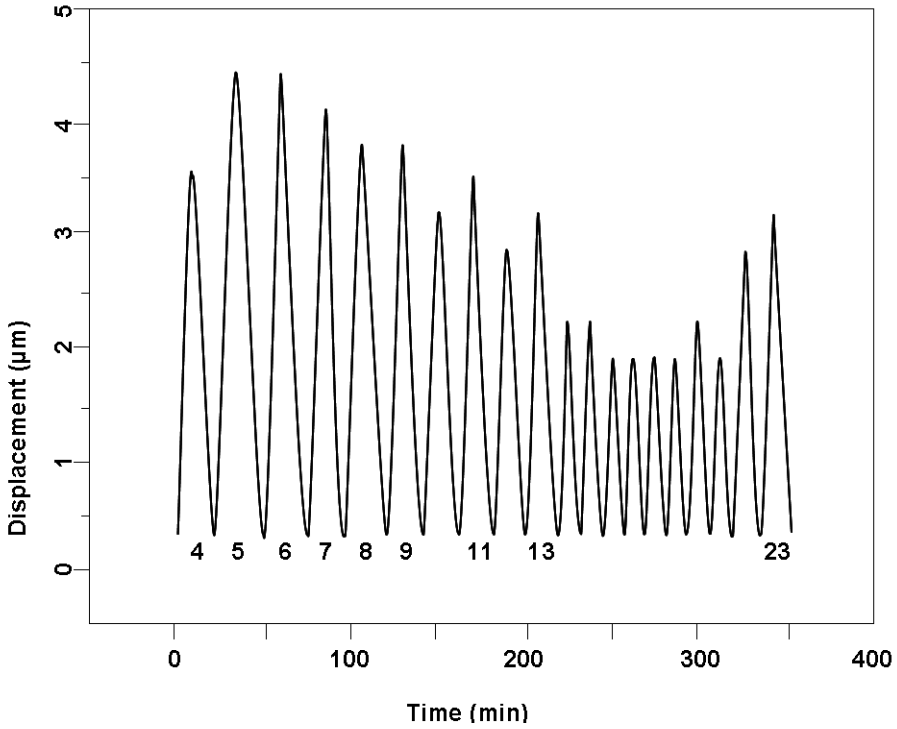

Figure 2.10: Br_2 intercalated HOPG optomechanical testing results shows that with identical input the material could not duplicate the previous results from cycle to cycle [8].

2.5 Electroactive Polymers

Electroactive polymers (EAP) have really taken off since the 1990s and consist of many types of materials including carbon nanotubes (CNTs) and carbon nanofibers (CNFs). EAPs react to electrical stimulation by altering their shape or size and behave in a manner similar to regular muscles. There are two types of EAP, ionic and electronic. The ionic EAP requires from 1 to 7 V to actuate. While the electronic EAP materials require 10 to 150 V/μm. Currently EAPs suffer from a low actuation force, 0.1 to 40 MPa and lack robustness. Speed is one benefit that they offer, having the capability to react in microseconds to minutes from stimulation and consume low power in the milliwatts range [19]. Of the electroactive polymers, the ones that most closely resemble carbon fibers are ionic type and include carbon nanotubes and nanofibers.

2.5.1 Carbon Nanotube Actuators. Carbon nanotubes are made up of cylindrical structures of carbon and are like rolled up sheets of graphene, a pure form of carbon. Carbon nanotubes were first identified as helical microtubules by Iijima in 1991. He observed that these "graphitic carbon needles" formed on the anode of a carbon electrode during DC arc discharge evaporation of carbon in argon at 1.3 atmospheres [14]. They come in two general forms as single-walled and multi-walled carbon nanotubes as shown in Figure 2.11.

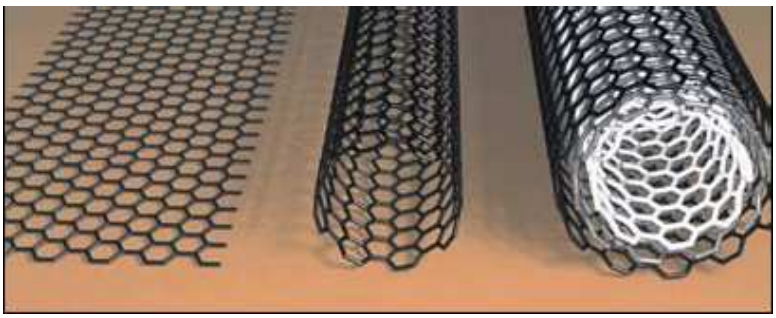

Figure 2.11: (left) graphene sheet, (middle) single-walled carbon nanotube, (right) multi-walled carbon nanotube [20].

Carbon nanotube characteristics are determined by the rolling of the graphene sheet in terms of the graphene lattice vectors a_1 and a_2 which reference the honeycomb pattern of carbon atoms in a sheet as shown in Figure 2.12. The line from the origin is called the chiral vector [n,m] where n is an integer in the direction of a_1 and m is in the a_2 direction. The meaningful information to be gained from this diagram are the numbers in brackets which provide all of the information required to further evaluate the physical and electrical properties of each carbon nanotube. Included in Figure 2.12 is an example chiral vector n and m with a vector of (3,3). Three varieties of carbon nanotubes exists; zig-zag, armchair, and chiral. The armchair structure [n,n], where n is the same are always metallic and acts as a metal contact. The zig-zag structure is [n,0]. The chiral type can have any combination of [n,m] that does not fall into either the armchair or zig-zag category. The chiral [n,m]

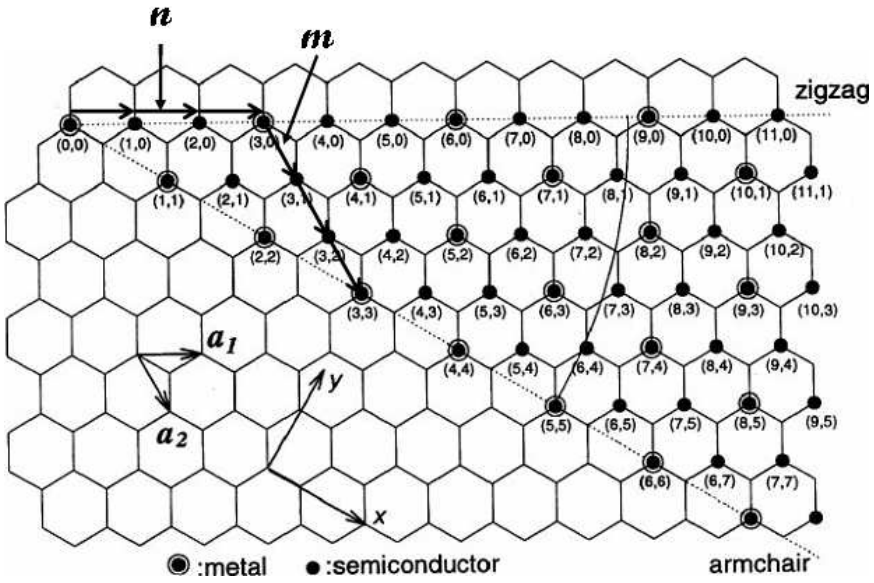

Figure 2.12: Chiralty of CNTs based on vectors a_1 and a_2, n and m are integer values for the direction vectors and represent the vector addition for a [3,3] metallic armchair CNT. n and m are equivalent for armchair CNTs which are metallic. Zigzag CNTs are along the [n,0] line and chiral CNTs, [n,m], are all the nanotubes that aren't considered armchair or zigzag types. Both the zigzag and chiral are metallic when the sum of [n,m] divided by three is an integer otherwise they are semiconductor types [21].

and zig-zag nanotubes [n,0] can be either semi-conducting or metallic. The CNT is metallic when the vector components, n and m are summed then divided by three and results in an integer, otherwise they are semi-conducting. The zig-zag structure vector is used as the axis from which the chiral angles are derived for CNTs. Thus the chiral angles are 0° for zig-zag and ± 30° for armchair. Chiral CNTs have chiral angles that are not 0° or 30° [21, 22]. CNFs are similar to MWNTs but consist of conical shaped rings of carbon that build upon each other as seen in Figure 2.13 [10].

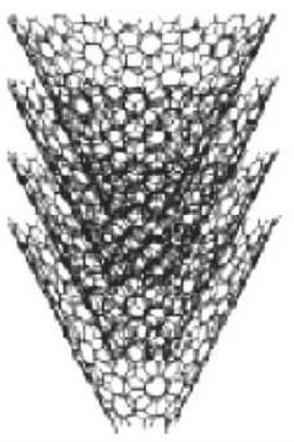

Figure 2.13: Carbon nanofiber structure is similar to multi-walled CNT, but is made up of conical rings of carbon atoms embedded into one another [10].

Numerous articles have been written which address the mechanical movement of ionically treated carbon nanotube sheets with or without a bonding polymer. The first carbon nanotube actuator experiment was published in 1999 and involved electromechanical actuation of single-walled carbon nanotubes (SWNTs) that were entangled and bonded together by van der Waals forces in a mat, "buckypaper," see Figure 2.14. It was theorized that when a potential was applied to a CNT that was submerged into an electrolyte and biased, a double layer of charge would form, reference Figure 2.15. One charge stays on the CNTs surface and another charge is in the electrolyte, creating an electrostatic effect. This had the effect of changing the bond length of the covalently bonded carbon atoms in the CNT. This resulted

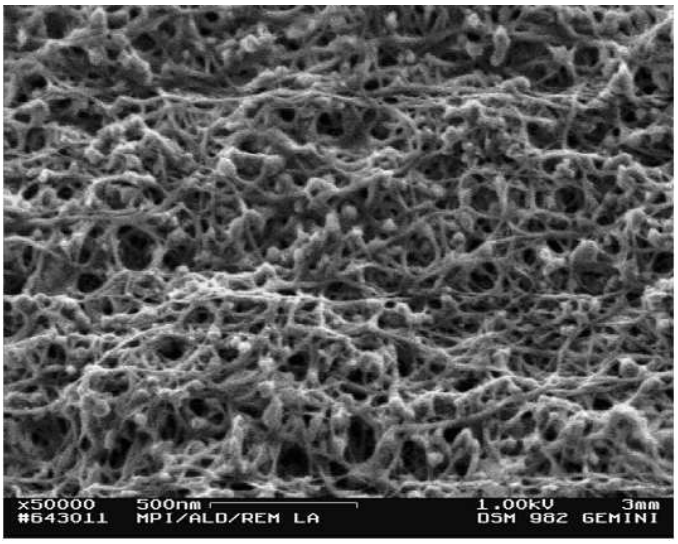

Figure 2.14: Surface of CNT sheet from scanning electron microscope [23].

in an expansion of d_{c-c} when electrons were added to the CNT and contraction when electrons were removed. To further demonstrate this, they created a two-sided device separated by an insulator and made up of two SWNT mats and applied an electrical voltage between them. This caused the device to deflect toward the side

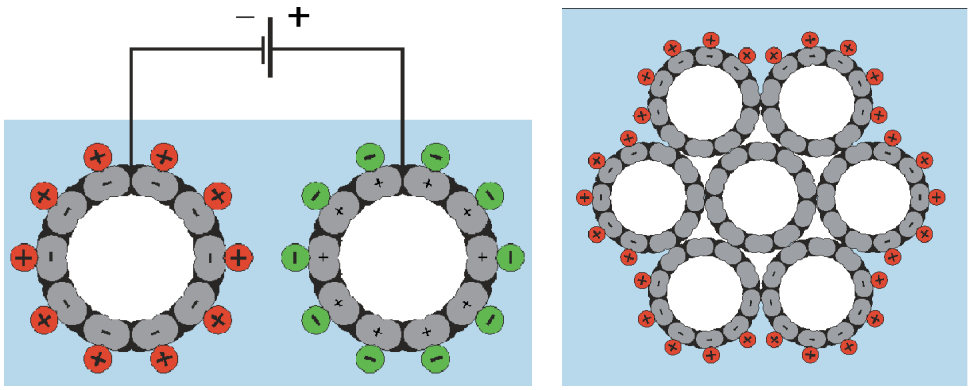

(a) (b)

Figure 2.15: (a) SWNT surface charging when a voltage is applied to two SWNTs submerged in an electrolyte. The charges on the nanotubes are offset by the charges on their surface from the electrolyte, (b) Ions can only react to the exposed surface area of bundled SWNTs [9]

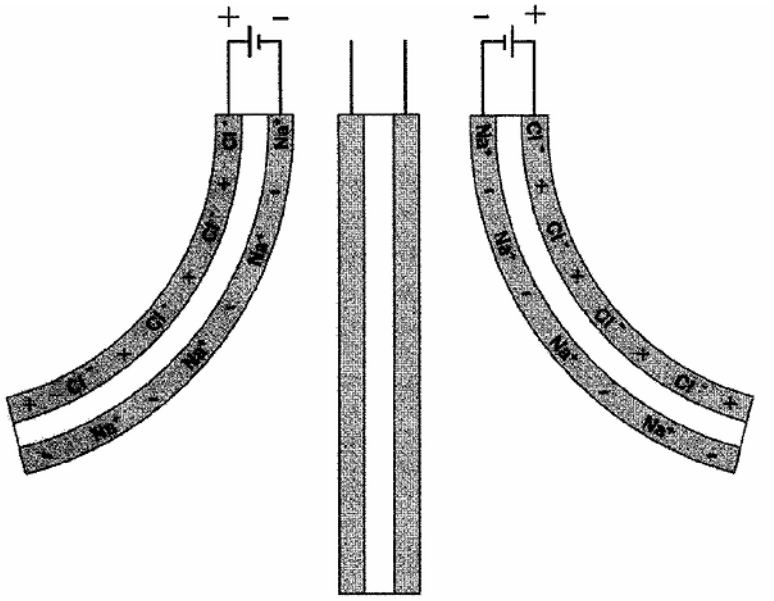

Figure 2.16: SWNT actuator deflection based on applied voltage polarity when submerge in NaCl electrolyte [9].

with the positive lead of the power supply and when the leads were reversed the device deflected in the other direction, reference Figure 2.16 [9].

Baughmans research involved using SWNT buckypaper without any type of bonding agent or polymer to keep the CNTs bundled up. This resulted in a potential reduction in actuator movement. The tubes in buckypaper could shift without providing any force to the actuator movement [9]. Since then, research has moved forward into creating buckypaper coated with polymers to bond them together and try to combine the energy that each CNT has to offer. Research into carbon nanofibers (CNFs) and multiwalled nanotubes have also been adapted and forwarded as well.

The University of Cincinnati is deeply involved in CNT and CNF research and has published many related articles. Their latest publication described three electrochemical actuators. Two of which were submerged in a 2 M NaCl solution and consisted of buckypaper with epoxy (CNT-epoxy) and a CNF sheet with polymethyl methacrylate on 3M tape (PMMA) polymer (CNF-PMMA). The final device was made to actuate in air using CNF sheets separated by a solid polymer electrolyte

(SPE) based on PMMA (CNF-SPE). The SPE was created with different mole ratios of "ion exchange materials."

The different devices were tested with a square wave input to observe the response amplitude and speed. The wet CNF-PMMA submerged in 2 M NaCl proved to be the most responsive showing approximately 0.5 mm of movement with 10 V at a frequency of 5 Hz. The CNT-epoxy actuator responded with approximately 0.17 mm of travel with 10 V applied at a rate of 1 Hz. Finally, the CNF-SPE returned a deflection of 0.28 mm with ±4 V at 0.5 Hz. The dry actuator reacts at a slower rate because of the inability of the ions to flow freely around the actuator as it does in the solution. Examples of the movement in the solution can be observed in Figure 2.17. The pictured CNT-epoxy actuator is not representative of normal operation. This picture was taken after 10 V was applied for several minutes and was irreversible.

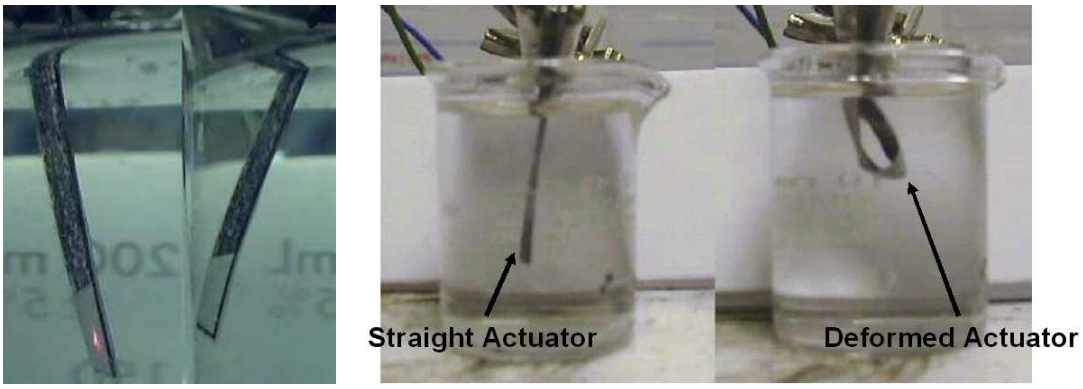

(a) (b)

Figure 2.17: (a) Composite strip of carbon nanofibers embedded in polymethyl methacrylate (PMMA) polymer, deformation occured after electrochemically driven in a 2 M NaCl solution, (b) single walled CNTs bonded with epoxy before and after 10 volts applied for several minutes in a 2 M NaCl solution [10]

2.6 Literature Review Summary

Currently, MEMS structures utilize electrostatic and thermal properties for actuation. Both of which have benefits and drawbacks. The thermal actuators are bulky and use low voltage and relatively high current to operate and produce around 20 μN of force per device. To create substantially more force, a large number of actuators would be required, consuming a lot of power and crucial design space. The electrostatic actuators are a staple in MEMS and would be difficult to replace with graphite fibers

Kadings results were useful. They showed that when intercalation occurred between 0.7 and 1.3 Volts, the electrical resistance of the fiber was reduced. This brought the resistance closer to metallic levels and could allow the use of GICs as conductors. He also explored the strain per volt characteristics of the intercalated carbon fibers. His results showed that a carbon fiber partially submerged in H_2SO_4 demonstrated a greater strain per volt than any MEMS thermal actuator.

The results of Salib provide insight into the intercalation of Br_2. Salib's research led to the discovery of works by James Gaier who has spent many years studying the intercalation of Br_2, particularly its stability in air and methods for improved intercalation [12, 24, 25]. Salib's results showed that his intercalated highly oriented pyrolytic graphite (HOPG) was able to decrease the number of carbon layers between intercalant layers without any further addition of intercalate. This is important, Br_2 is very stable in air and if the GIC can be stimulated to alter its structure without the addition of any further intercalant then the device that uses this GIC would not necessarily have to be sealed from the environment.

Carbon nanotubes and nanofibers show great potential but the devices that have been designed thus far have low force and are macroscopic devices. The devices are created with randomly ordered fibers and tubes that in their disorder are not guaranteed to contribute forces in the desired direction. Research into single CNTs and CNFs as actuators will become more prolific as the ability to determine the chiralty of CNTs becomes more precise. This will open an opportunity to create

nanoactuators that produce a great force to weight ratio. For now, the use of CNTs as actuators is still in its infancy and is not a viable option to create micron scale actuators

This area of study is not without risks. The carbon fibers that will be used in this research are industrial materials and are created by a corporation that has no responsibility to announce when they change their production process. The results from this work might not translate to an identical experiment on fibers that were produced from another production run. Fiber quality also varies from batch to batch without any alteration to its preparation process [11]. The intent is to use this research as a stepping stone to move forward the research with HOPG. Further problem areas include the creation of GICs that react to the environment and can release toxic materials when exposed to air. It would be quite beneficial to use a GIC that is stable in air and provides the desired forces with minimal degradation and risk.

As stated earlier, the military and industry are both seeking to reduce power and weight taken up by switches and actuators. The work of Kading and Salib suggests that GICs have the potential to fit this need. The goal of this research was to intercalate six different samples of `Thornel`® P-100 fibers each having a different surface treatment with H_2SO_4 to study the DC and small signal impedance characteristics of each fiber and if possible observe the contraction of the fiber that occurs during the process. Many trials were made to mount fibers but they would often break during the production process or delaminate when exposed to sulfuric acid. A few fibers survived and were tested and produced limited data.

III. Graphite Intercalation Theory

M.S Dresselhaus stated graphite intercalation compounds (GICs) were first discovered in 1841 by Schaffäutl. Further research on GICs occurred in the 1930s due to the development of X-ray diffraction techniques to complete staging measurements. In the 1940s, work concentrated on the physical properties of intercalation compounds leading to the explosion of research starting in the late 1960s and running until 1991 when carbon nanotubes were discovered and received the brunt of the research effort [26].

3.1 Graphite Intercalation

Intercalation occurs in materials that have a very strong intraplanar and a much weaker interplanar bonding strength as described in Figure 1.1. Materials that fit this description include graphite, transition metal dichalcogenides, some silicates, metal chlorides, clays, polymers and gels. Graphite intercalation has been researched in depth because of the usefulness of the products along with the planar order that can be achieved. Graphite intercalation compounds (GICs) can be tailored to highlight desired traits and hundreds of intercalant species have been identified with various characteristics [27]. Electrical, thermal and magnetic properties are just some of the characteristics that can be altered by intercalation [26]. There are several approaches to intercalate graphite structures and effective intercalation is limited by the graphitization of the host material. The greater the graphitization the more homogenous and complete the intercalation.

There are two types of graphite intercalation compounds, covalent and ionic, named for the type of intercalant bonding present. The covalently bonded GICs are non-conductive and also causes the graphene layers to ripple. The rippling is from the conversion of the carbon bonds from triganol (sp^2) to tetrahedral (sp^3). These GICs include graphite oxide, carbon monoflouride, and tetracarbon monoflouride. Although some research has been completed on covalent GICs they are not as highly regarded as the ionic type. The ionic GICs are made up of all intercalants that

don't produce a covalent bond, but does not necessarily mean that they are strongly ionic. Most of the intercalants in this group maintain there own chemical identity even embedded within the graphite. Ionic intercalants include Br_2, IBr, ICl, K, Rb, Cs, HNO_3, $FeCl_3$, SbF_5 where these materials can be intercalated spontaneously as a liquid or vapor into graphite given a long enough period of time. Another method of intercalation is to use electrochemical cell materials such as NH_3, H_2SO_4, H_2F_2, H_3PO_4, and HNO_3 [3]. By no means is this a complete list as there are well over one hundred intercalants.

3.1.1 Intercalation Process. As stated in Section 1.1, carbon has four electrons that are available for bonding to other atoms. Graphite as a material has three carbon to carbon covalent electron bonds, σ, per atom (2s, $2p_x$, $2p_y$) with the final electron ($2p_z$) forming a π-bond that's between the layers of graphene sheets (reference Figure 3.1.) These π-bonds are weak and allow for the carbon planes to slide across each other. They also provide a prime location for other molecules or ions to occupy by pushing the carbon atom layers apart, creating strain. This results in a material that is similar to an electrical heterojunction superlattice [27].

Ionic GICs are further divided based on the action of the intercalant into two sub-divisions, donor and acceptor. Donor GICs are created by the movement of negatively charged donor intercalants in between the layers of a graphite host. At this point, the donor intercalant then passes an electron off to a carbon atom, resulting in the intercalant becoming positively charged. This positive charge attracts electrons to the interface and places an electron on the graphite side at the graphite/intercalant interface providing an electron conduction path. Acceptor GICs are very similar to the donor type except the electrons transfer from the adjacent carbon layer into the intercalant that has moved into the graphite host. Although, the transfer of electrons in acceptor GICs is not as efficient as experienced by donor GICs, they still provide increased conductance over pristine graphite. The concentration of holes in the carbon layers quickly decrease as you move further away from the intercalant

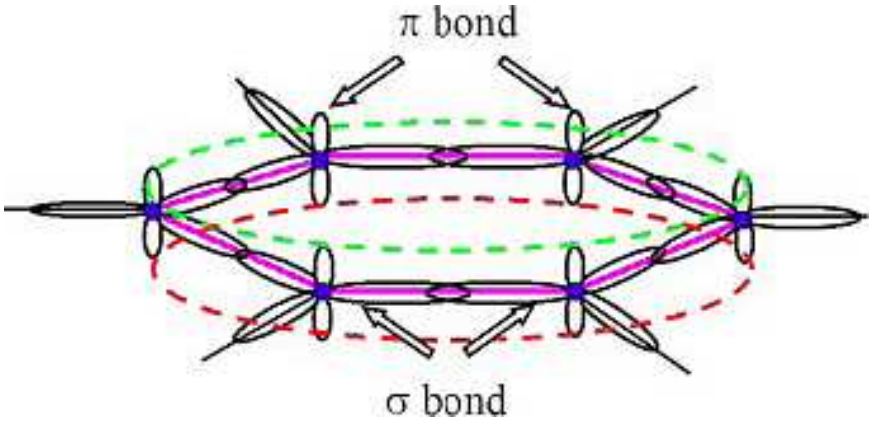

Figure 3.1: Vertical Π bonds interconnect the graphene layers of carbon while the horizontal σ, covalent bonds, hold the graphene plane together [28].

layer. Therefore, in either a donor or acceptor GIC the conduction occurs along the graphite intercalant junction in the graphene plane irregardless of whether the carriers are holes or electrons [5, 27].

3.1.2 Intercalation Structural Effects. When a graphite material is intercalated, the intercalant materials are brought in through the edges of the material. Intercalation, forces both a separation and shifting of graphene sheets, this requires an intercalant vapor pressure, P_t, on the graphite surface. The threshold pressure is dependent on the graphite sample thickness and type. For example M.S. Dresselhaus summarized works of Hooley and Bartlett to conclude "P_t is lowest for single crystal flakes, higher for HOPG host material and yet higher for carbon fibers" [26]. After the initial intercalation-deintercalation cycle, less P_t is required for intercalation because the first cycle causes cracks in the surface to form from the planes movement and a corresponding reduction in bond strength between the layers π-bonds.

Graphite intercalation compounds (GICs) are also referenced by their materials stage. The stage, n, is the number of layers of graphite that exist between each layer of intercalant, Figure 1.2. The lower the number, the fewer layers of graphite between intercalant layers. The highest degree of intercalation is stage one and the lowest is stage ten. The location that a pocket of intercalants resides within the graphite

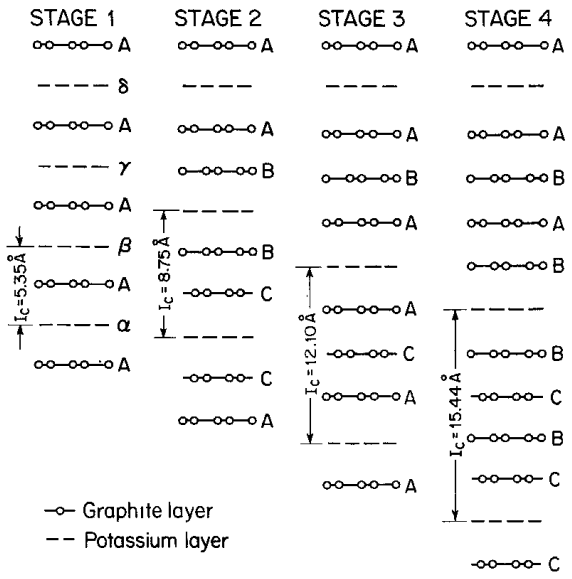

Figure 3.2: Staging describes the number of graphene layers between each layer of intercalant, thus this figure illustrates stages 1-4 of potassium intercalated graphite. I_c represents the compounds structural repeat distance. This diagram also shows the differences in layer structure between various stages which can be accounted for by the shifting of the intercalant during transitional periods between stages [27].

host is called the gallery. As the GIC advances through the stages more energy is required to move the graphite layers and shift the galleries within each layer to transition between stages. Figure 3.2 shows how the different layers of graphene are shifted as potassium is intercalated and I_c, the thickness of the GIC before a layer structure is repeated. I_c can be calculated from

$$I_c = d_s + (n-1)c_o \text{ (Å)} \tag{3.1}$$

where n is the stage index, c_o is the gap between pristine graphene layers and $d_s = d_i + c_0$ where d_i is the height of the intercalant molecule. In this case d_s=5.35 Å and thus d_i= 2.00 Å [27].

The graphene layer separation resulting from intercalation can be of use as mentioned in Sections 2.4.1 and 2.4.3. Where Koyama and Salib used the planar expansion of intercalated graphite to create strain. Graphite structures also contract

and expand in the a-plane as referenced in Figure 1.1 and mentioned in Section 2.4.2. The contraction is due to a change in the d_{c-c}, in plane carbon to carbon atom distance. The d_{c-c} increases with donor intercalation and decreases when acceptor intercalation occurs [29, 30, 31]. Chan acknowledges that Nixon and Parry were the first to make the connection between charge transfer and the change in the carbon-carbon bond distance. Since then, several authors have shown that the contraction between the carbon atoms is dependent on the gain and loss of electrons.

Pietronero and Strässler (PS) derived equations for the bond length change using the tight bonding method originally applied by Kakitani. Defining $u(s)$ as the change in d_{c-c} that resulted from intercalation to stage s. Their derivation culminated in

$$u(1) = 0.157 f_c + 0.146 |f_c|^{3/2} + 0.236 f_c^2 \text{ (Å)} \tag{3.2}$$

for stage 1 where f_c is the charge per carbon atom for a layer of charged atoms. Equation 3.2 assumes that $f_c \gtrsim 0.01$ and $f_c \leq 1/6$. The observed expansion and contraction of d_{c-c} from donor and acceptor intercalation is caused by the linear leading term. PS then expanded upon their calculations to include lower stage GICs with two assumptions. First, the charge transferred was restricted to the adjacent carbon layers. Second, that the induced strain must be equally shared between all the layers. It was accepted that the first assumption was not entirely accurate but since the total energy was being considered, it was applicable. For stages greater than 1, the change in d_{c-c} is given by [29].

$$u(s) = (2/s)u(1) \text{ (Å)}, \; s \; \geqq \; 2 \tag{3.3}$$

Data experimentally gathered and plotted in Figure 3.3 shows a slight deviation from the linearity which increases the likelihood of f_c remaining fairly constant. To validate their equations PS used previous experimental values for d_{c-c} to calculate the charge transfer per carbon atom, f_c. They then compared their results to previous methods and showed good correlation [29].

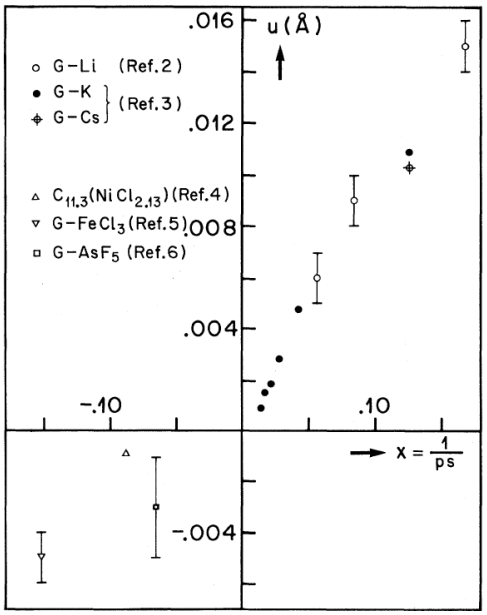

Figure 3.3: Experimental values measuring changes in bond length, u, based on original length of 1.421 Å. The x-scale is dependent on the ratio of intercalant molecules to carbon atoms which is derived from the general equation CA_x, where A is the intercalant molecule. x=1/ps and is dependent on the stage, s, and the ratio of intercalant molecules to carbon atoms, p [29].

Ames laboratory has published a couple of documents that have studied the C-C bond distance change due to charge transfer and have modeled their results [30,31]. In their original work, they worked under the premise that any electron that enters into the reaction is transferred between the intercalant and graphite. Kamitakahara, Zarestky and Eklund electrochemically intercalated HOPG with D_2SO_4 to observe the change in d_{c-c} and compared their results to PS. As shown in Figure 3.4, they found that their results deviated from PS when f_c reached 0.21 but were respectably close. The shaded areas represent pure stage regions, from left to right (stage-3, stage-2, and stage-1). The open circles and open triangle in the plot are D_2SO_4 and stage-2 $SbCl_5$, respectively. The horizontal bar is from stage-1 H_2SO_4 collected data [30].

In following up Kamitakahara, Zarestky and Eklunds research, Chan and others compared the charge density of a donor GIC and pristine graphite to identify a factor

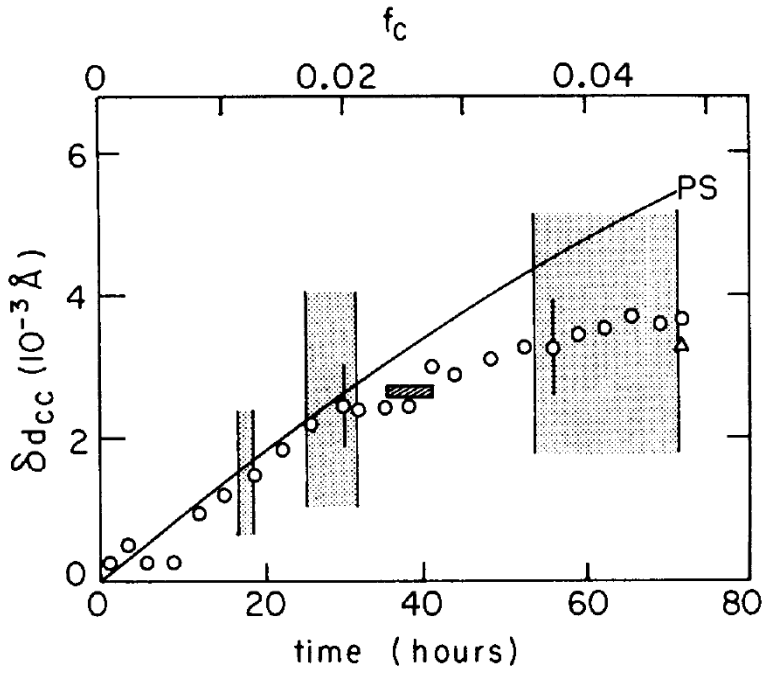

Figure 3.4: HOPG intercalated with D_2SO_4 results showing the d_{c-c} change over time versus the value f_c, charge transfer per atom. The solid line represents PS calculations. The open circles and open triangle are D_2SO_4 and stage-2 $SbCl_5$, respectively. The shaded areas represent pure stage regions, from left to right (stage-3, stage-2, and stage-1) [30].

that was not taken into account by PS. The movement of an electron from the σ to the π orbital, which weakens the carbon to carbon bond and allows the d_{c-c} to increase in donor type GICs. Through their calculations they determined that the d_{c-c} length variation was almost linear for donors but non-linear and smaller for acceptors. With the assumption that each electron that flowed into the HOPG as it was electrochemically intercalated with H_2SO_4 resulted in a one for one transfer from the HOPG to the intercalant. They used the chemical formula to create an equation that would calculate p and thus f_c:

> ...chemical formula $C_p^+(HSO_4)^-(H_2SO_4)_x$, where x has been determined from weight-uptake measurement to lie between 2.0 and 3.2, depending on p. The oxidation number p and the charge transfer per C atom f_c=p^{-1} are completely determined by the mass of the starting graphite and the total charge $Q = it$ which has flowed in the external circuit.

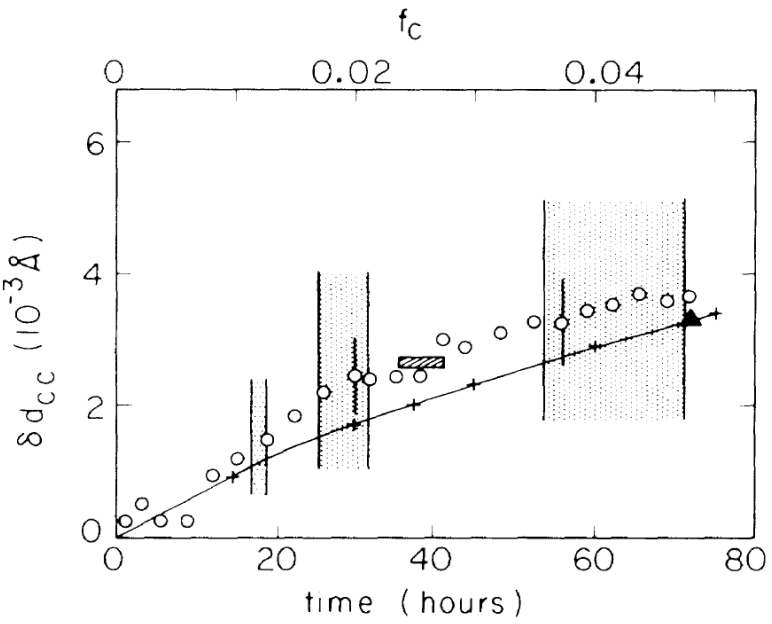

Figure 3.5: HOPG intercalated with D_2SO_4 results showing the d_{c-c} change over time versus the value f_c, charge transfer per atom. The solid line represents the updated model calculations. The open circles and open triangle are D_2SO_4 and stage-2 $SbCl_5$, respectively. Currently calculated model is consistently lower then the actually measured results but are within the experimental uncertainty [31].

> If the constant current i is in microampere and the intercalation time t in hours, then one finds p via $p = 2230.4m/it$, where m is the starting graphite mass in milligrams. [31]

They then plotted the experimental and calculated values against each other as shown in Figure 3.5. The solid line is based on their updated model and showed a good correlation but the expected values undershot actual results but was within the "experimental uncertainty" of the data, providing yet another more refined model for acceptor intercalants. The open circles and open triangle are D_2SO_4 and stage-2 $SbCl_5$, respectively. The shaded areas represent pure stage regions, from left to right (stage-3, stage-2, and stage-1) [31].

3.1.3 Graphite Intercalation Methods. Graphite intercalation is accomplished by several means and the best method is dependent on the intercalant and type of graphite and includes: two-zone vapor transport, one zone method, and

electrochemical techniques. There are many variations and alternative processes to create GICs but these are all that will be discussed here. The critical factors in intercalation are temperature, vapor pressure, intercalant properties and graphite host characteristics. The thickness, general size, and type of the graphite plays a substantial role in the process. Most GICs will react and degrade when exposed to the environment; thus, they are processed in encapsulated chambers and stored in inert gases [27]

Two-zone vapor transport takes place in a two zone furnace where the graphite and intercalant material are placed at opposite ends of a sealed reaction tube. The tube must keep the two materials from making contact, as this process requires that only the vapor from the intercalant react with the graphite sample. Both sides of the chamber are then heated to different temperatures, T_g, the graphite temperature drives the intercalation rate and T_i, the intercalant temperature determines the vapor pressure. T_g must always be greater than T_i to ensure that the intercalant does not condense onto the surface of the sample. The staging of the resulting GIC is determined by (T_g-T_i), the greater the difference, the lower the staging. Isobars are graphs that show the expected staging results when the intercalant is held at a constant temperature, producing a constant intercalant pressure, and the graphite temperature is varied changing the reaction rate. The results are still dependent on the graphite host type, size, and defects but when done correctly produces a well staged GIC [26, 27].

Liquid intercalation involves the placement of graphite and a liquid intercalant into a reaction tube in a one zone furnace allowing the two components to contact. The temperature of the cylinder is kept uniform to maintain consistent staging throughout the GIC. There are two main approaches to using this technique, one requires that excess intercalant be placed into the cylinder and heated, the other method places an exact amount of intercalant into the chamber so that all of it will be consumed during the reaction. Once the chamber is heated, the time and temperature determine the staging of the resulting GIC [27].

The electrochemical method submerges a graphite sample held in a non-reactive clip in an aqueous or non-aqueous electrolyte, an ionic conductor. Two electrodes, graphite and platinum, are placed in the solution and are electrically biased as shown in Figure 3.6. This creates two half reactions that produce ions at each electrode.

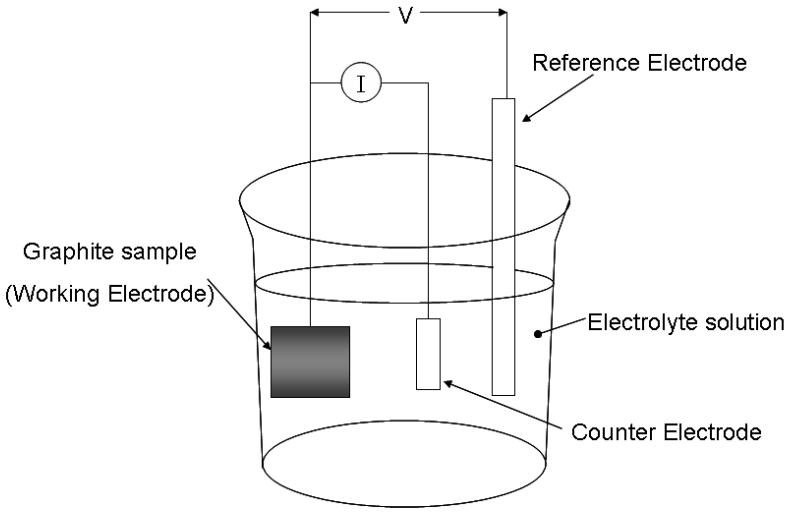

Figure 3.6: Electrochemical intercalation occurs in an electrolytic solution with a working electrode (graphite sample) a counter electrode (platinum) and an optional reference electrode to measure the voltage at the working electrode from a fixed reference [26].

In the graphite case, the ion is not just deposited on the surface but drawn into the structure and intercalated. Generally there are three electrodes placed in the solution to include the working, counter and reference electrodes. The working electrode is the anode or cathode, whichever one has the graphite sample attached and depends on whether an acceptor or donor GIC is to be created. The counter electrode, platinum, is the electrode where the second half of the electrochemical reaction takes place opposite the working electrode. Finally, the reference electrode is non-reactive to the electrolyte and has a constant potential. This potential is used as a reference for the voltage on the working electrode. The two main electrodes, working and counter, are more commonly referred to as the cathode and anode. The anode is where chemical reduction occurs, i.e. the material provides an electron to the

electrolyte. The cathode is where oxidation occurs, i.e the electrons are released from the electrolyte and transferred to the cathode. The anode is connected to the positive terminal of a power supply and the cathode to the negative side. When an acceptor GIC is to be created the graphite is an anode and a cathode for donor GICs. The reference electrode although not required provides a portion of the information required to determine the rate of ion flow [26, 27, 32]

3.2 Carbon Fibers

Originally invented by Thomas Edison in his pursuit of a long lasting light filament, carbon fibers have experienced a long period of growth and research [5]. Carbon fibers are any fibers that have been created and are over 92 wt% carbon. Carbon fibers are similar to other forms of carbon but are normally not as graphitic. Therefore, they can be intercalated but not as well as other forms of graphite. This can be partially overcome by heat treating the fiber anywhere from 2000 °C to 3000 °C which causes the graphite islands in the *c*-plane within the fiber to grow, reducing defects and increasing conductivity. The required temperature and the amount of benefit is dependent on the type of fiber.

3.2.1 Production. Carbon fibers are constructed from many pre-cursor materials to include Polyacrylonitrile PAN, pitches (isotropic, mesophase, and pre-mesophase pitch), and rayon. Carbon fibers created from these materials are all processed differently but the overarching process is similar. The original pre-cursor is processed and broken down into a more refined product. This product is then spun into a fiber form and a stabilization treatment occurs. This involves heating the fiber up to as much as 600 °C to prevent the fiber from melting. The carbonization process follows, the fiber is then heated to a range of temperatures but is between 1200-1600 °C to remove almost all of the non carbon impurities. This is technically a carbon fiber but has poor mechanical traits, i.e Young's modulus and tensile strength. These are improved by the final heating stage, graphitization, which causes the graphite pockets to interconnect. Graphitization takes place between 2500

and 3300 °C. The fibers developed from the above pre-cursors also require that some form of pulling stress be applied at a specific point in their production process which causes the carbon atoms to align. Without this stress the heat treatments would have little affect on the fiber structure and the resulting fibers would not have the mechanical properties that industry requires [33, 34].

In "Carbon Fibers," Donnet referenced several articles that highlighted the reduced resistance of various forms of carbon fibers when heat treated from 1000 to 3000 °C [33]. One article sponsored by the Air Force Material Lab completed an intense scrutinization of random and radial fibers heat treated from 500 to 3000 °C and concluded that at higher temperatures the resistivity was reduced and higher graphitization was achieved [35]. The fibers heat treated at 500 °C had a resistivity that was so high that it was not included in Figure 3.7. 1700 °C was the pivotal temperature for increased graphitization. After that point, graphitization became more apparent because of the increased width of graphene sheets and the decreased

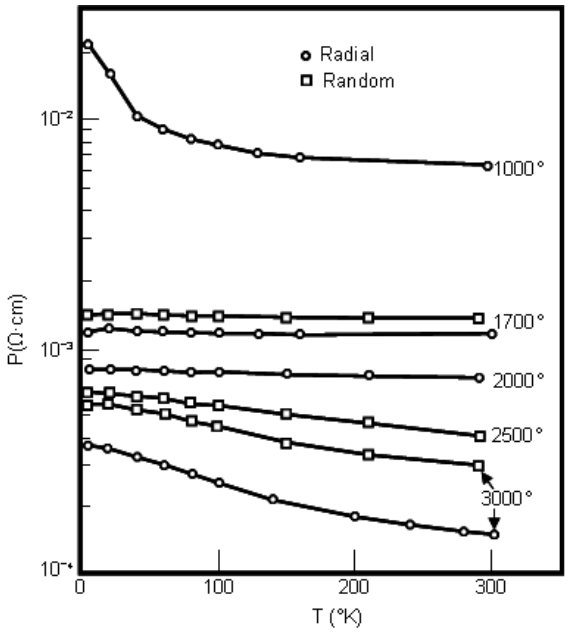

Figure 3.7: Radial and random ordered pitch based carbon fibers show reduced resistivity with increased heat treatment, although the radial fiber has the lowest resistivity [35].

distance between carbon atoms in the same plane, d_{c-c}. The d_{c-c} continued to approach the standard value of 0.335 nm as the temperature increased with the radially structured fibers having the best results as shown in, Figure 3.8.

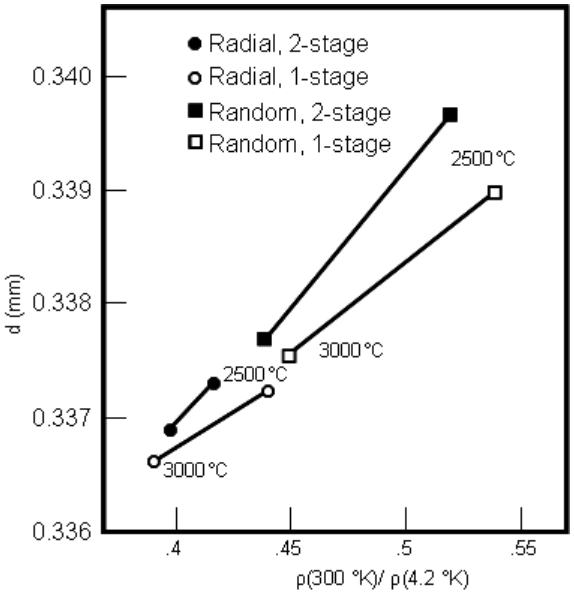

Figure 3.8: Radial and random ordered pitch based carbon fibers show improved graphitization by reducing the C-C distance that approaches the ideal value for d_{c-c} [35].

3.2.2 Types. Carbon fibers are divided into five types based on their mechanical values, i.e. Young's modulus and tensile strength to Young's modulus ratio. Table 3.1 provides the Young's modulus for each of the different fiber types. The stiffest fibers are ultra-high modulus (UHM) fibers and mostly consist of mesophase pitch based fibers. The next stiffest, high modulus (HM) fibers have a Young's modulus that ranges from 300 to 600 GPa and a tensile strength to Young's modulus ratio of 0.001. Intermediate modulus (IM) and high tensile (HT) fibers have similar Young's modulus but they differ in their tensile strength to stiffness ratio, the IM has a ratio of 0.01 and the ratio for HT fibers is greater then 0.015. Finally, the low modulus (LM) fibers have both a low Young's modulus and tensile strength.

Table 3.1: Recommended breakdown of carbon fiber types as recommended to IUPAC in 1995 [33, 34]

Carbon Fiber Types	
Fiber type	**Young's Modulus**
Ultra-high modulus (UHM)	>600 GPA
High Modulus (HM)	>300 GPa
Intermediate Modulus (IM)	275 to 350 GPa
High Tensile (HT)	150 to 300 GPa
Low-Modulus (LM)	>100 GPa

LM fibers have an isotropic structure because they were not hot-stretched during production [33, 34].

3.3 Research Specific Information

The electrochemical method is used for graphite-sulfuric acid intercalation. The carbon fiber sample acts as the anode (working electrode) and is held in place with a non-reactive material (Au) in the sulfuric acid electrolyte. The cathode (counter electrode) (Pt or Au) is placed in solution. A positive voltage is applied to the working electrode and the negative terminal is connected to the counter electrode, causing a current to flow through the acid. Two half reactions occur within the electrolyte at each electrode. H^+ accumulates at the counter and HSO_4^- builds around the working electrode and enters along with H_2SO_4 between layers of graphene. The general stoichiometric chemical equation for H_2SO_4 intercalation from stage 8 through stage 1 is

$$mC + 3.5H_2SO_4 \rightleftarrows C_m^+ HSO_4^- (H_2SO_4)_{2.5} + H^+ + e^- \ (\text{m}\approx 24) \tag{3.4}$$

where m represents the number of carbon molecules required to balance the equation [1]. The staging of the graphite can be determined by the use of a reference electrode and current measurement between the working and counter electrode.

Some unpublished work was previously accomplished at AFIT under the direction of Dr. Kladitis. In this research, conductivity tests were performed on a `Thornel`® P-100 carbon fiber. The fiber was mounted on an Agilent 4284 LCR meter and electrochemically intercalated with H_2SO_4 using an external DC power supply, reference Figure 3.9 for the equipment setup. The fiber was then intercalated with a cathode voltage of 0.0 V to 1.4 V provided by an Agilent 6624A DC Power Supply, while conductivity measurements were taken with the 4284A Precision LCR Meter from 20 Hz to 1 MHz. The carbon fiber was placed across the test fixture and clamped into place on top of a glass slide. The glass slide was required to ensure the equipment would not be exposed to the sulfuric acid. The fibers were approximately

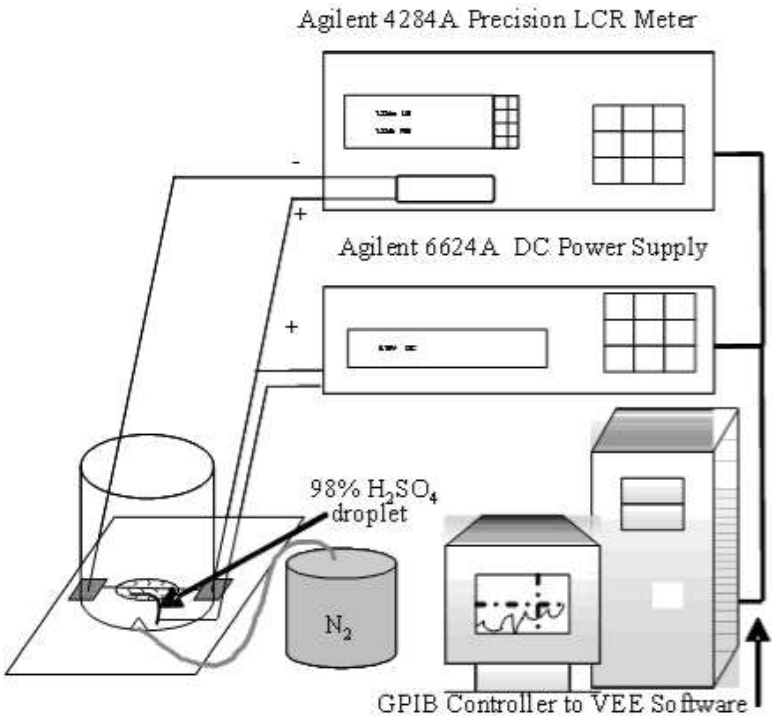

Figure 3.9: Experimental set-up for partial carbon fiber intercalation. A fiber is connected in series with the Agilent 4284A, the positive terminal of the Agilent 6624A power supply is attached to the fiber and the negative terminal contacts the platinum cathode. Nitrogen is pumped into the beaker to keep the acid from absorbing moisture and diluting .

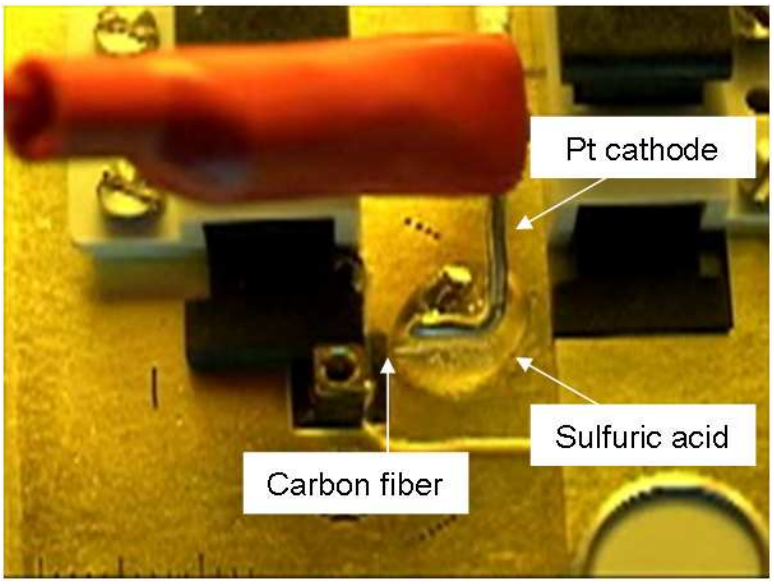

Figure 3.10: Picture of Thornel® P-100 fiber being intercalated with sulfuric acid. Hydrogen bubbles are seen between the carbon fiber and the platinum cathode and appears as a white line in the sulfuric acid

2 cm long with about half of that being exposed to the acid, as shown in Figure 3.10 to view the experiment in progress.

Although the results seen in Figure 3.11 were impressive. They do not represent the whole picture and thus must be questioned. The fiber was not completely exposed to the sulfuric acid so the point where the intercalation stopped is an unknown. Therefore, further research needs to be completed such that the entire fiber is completely submerged in the acid.

3.4 Graphite Intercalation Summary

This chapter provided a more in depth look into the graphite intercalation theory to include the types of intercalant compounds such as ionic or covalent. The ionic intercalants were further delineated into donors and acceptors. The donors provide electrons to the graphite when they are intercalated and acceptors do the opposite. Although it may seem counter intuitive, acceptor type graphite intercalation compounds (GICs) contract in the a-plane when intercalation occurs because of

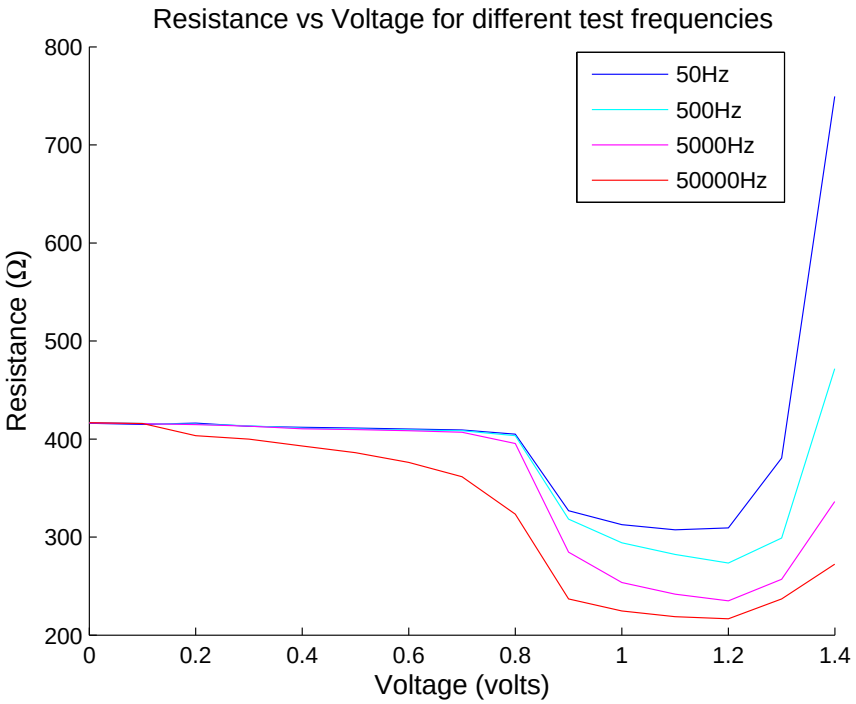

Figure 3.11: Radial and random ordered pitch based carbon fibers show improved graphitization by reducing the C-C distance that approaches the ideal value for d_{c-c} [35].

electron transfer. Donors on the other hand expand and do so more linearly than the acceptor type GICs. Changing length is one of two important reactions that occur with intercalation. The second possible benefit is a change in conductivity. There are numerous techniques to intercalate graphite and includes two zone heating, electrochemical, and liquid submersion and heating. Carbon fibers were discussed which included the methods of production for the three different material types: PAN, pitches, and rayon. Fibers are further broken down by their construction characteristics such as Young's modulus and maximum temperature treatment. Finally, the research to be completed was reviewed and information that related specifically to it was discussed.

IV. Modeling, Simulations, Design and Fabrication

4.1 PolyMUMPS Process

The Polysilicon Multi-User MEMS Process (PolyMUMPs) creates three layers of micromachined polysilicon surfaces. The MUMPs process is based on a process developed at the University of California, Berkeley Sensors and Actuators Center, during the late eighties and early nineties. PolyMUMPs is an inexpensive way to produce low quantity proof of concept MEMS structures. The production process includes the creation of seven physical layers and eight lithographed layers. The deposition order of the seven layers from the substrate are silicon nitride, polysilicon 0, oxide 1, polysilicon 1, oxide 2, polysilicon 2, and metal. Lithography is the process used to layout the pattern that will be produced on each physical layer which is then etched to remove unwanted material. The oxide layers are sacrificial layers and, when removed, can allow the polysilicon layers above them to become mobile [13].

Each layer in the PolyMUMPs process has a specific purpose and provides flexibility in the design of numerous structures. The n-type [100] oriented silicon wafer has a 1-2 Ω-cm resistivity and is highly doped with phosphorous to reduce charge build-up in the substrate from surface structures. The silicon nitride (Nitride) layer acts as an isolating layer to electrically separate the surface and the substrate. The initial polysilicon layer (poly 0) is an electrical layer allowing the creation of contacts, conduction paths or ground planes. Next is the first oxide (1st oxide), the first sacrificial layer, that can provide space between the layers above and below it. The following layer is the first releasable (mechanical) layer which can be mobile and is made up of polysilicon (poly 1) . The second oxide (2nd oxide) follows and serves the same purpose as the 1st oxide. The second mechanical layer is next and is also the final polysilicon layer (poly 2). Finally, the metallic layer is added to provide electrical conduction [13]. A good example of the final product can be seen in Figure 4.1.

The process consists of several steps, providing enough capability to create designs to meet most users needs in design construction. The PolyMUMPs process

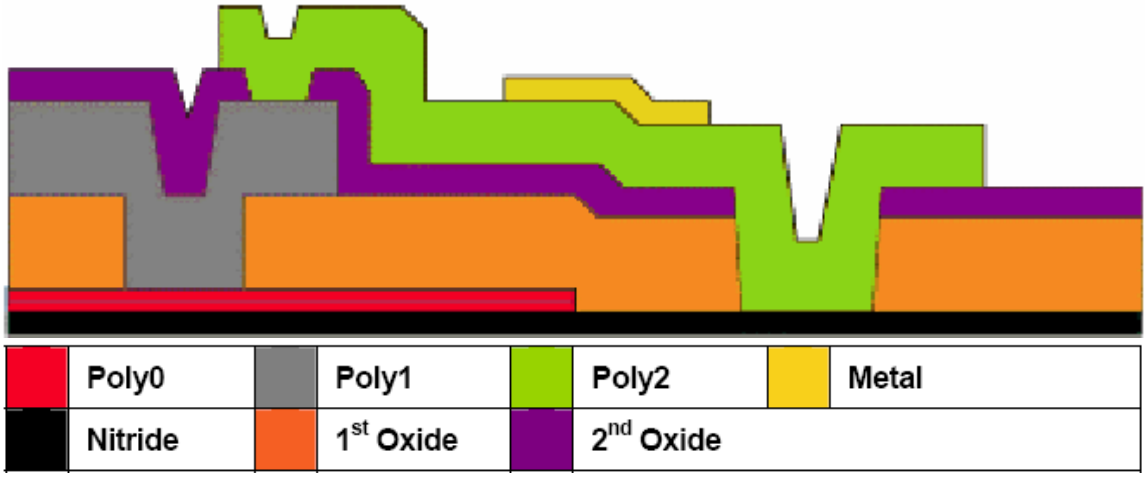

Figure 4.1: Cross sectional view of PolyMUMPs structure [13].

starts with a 100 mm n-type (100) silicon wafer coated with a 600 nm layer of silicon nitride deposited by low pressure chemical vapor deposition (LPCVD). This is followed by a 500 nm coating of poly 0. The poly 0 is then patterned with photolithography and reactive ion etched (RIE). A layer of phosphosilicate glass (PSG) oxide 1, 2 μm thick is then applied. The wafer is then annealed in argon gas for 1 hour at 1050 °C to both cure and drive phosphorous into the poly 0 layer. The phosphorous dopes the polysilicon giving it the desired conductivity characteristics and the annealing also reduces the inherent stress of each layer. Before any further layers are added, dimples are lithographically patterned and etched resulting in 750 nm deep holes in the PSG. Once that is accomplished, Anchor1 is patterned and etched. Anchor 1 creates a hole through the PSG providing a location for poly 1 to bond with the material immediately below the PSG. Both the dimples and anchor 1 holes will be filled with the next layer of polysilicon, poly 1, during the next deposition step [13].

Poly 1 is applied with a thickness of 2 μm. Followed by a 200 nm layer of PSG and annealing as described above. Next, the wafer is coated with photoresist (PR) and lithographically patterned. Photoresist is a key material in the production of most MEMS structures. PR is reactive to a specific light frequency and energy level

and once cured provides a mask for the application or removal of a layer of material in the desired location. Subsequently, the PSG is etched to create a hard mask, one that can hold up better to the etchant required for etching poly 1. The poly 1 is then etched. The remaining PSG and PR are then removed. This is followed by an application of 750 nm of PSG oxide 2 and annealing. Two processes are completed via RIE etching prior to the addition of the next polysilicon layer. First, the poly 1-poly 2-via is created by photolithography and etching which creates a path for poly 2 and poly 1 to make electrical/physical contact. After completing that step, the PR is removed and another layer of PR is applied and patterned for anchor 2. Anchor 2 provides a path for poly 2 to make contact with the silicon nitride or poly 0 layer as a physical contact point, anchoring poly 2 to the wafer [13].

Poly 2, 1.5 μm thick, is then deposited on the wafer followed by a 200 nm layer of PSG. Similar to the poly 1 process; the wafer is annealed, patterned and both the PSG and poly 2 are etched to create the desired poly 2 pattern. The PSG and PR are then removed and the wafer is ready for the final layer to be added. The wafer is coated with PR, masked, developed and coated with 500 nm of metal. The unwanted metal is removed by the metal liftoff process, soaking the wafer in a solvent that attacks the PR underneath the metal washing the metal away. The die are coated with PR to protect the structures during shipment [13].

This completes the production process. The wafers are then shipped to the user where they complete the process by soaking there structures in hydrofluoric acid for 2 - 5 minutes to remove the sacrificial layers, PSG oxide 1, and PSG oxide 2. The PolyMUMPs process is fairly constant but each production run has different material characteristics so MEMSCAP creates a data sheet for each production run [13].

4.2 PolyMUMPS Material Properties

4.2.1 Analytical calculation of internal stress of PolyMUMPS. MEMSCAP provides a table of material properties that they have measured and calculated, Table 4.1. This data is on the macroscopic scale and so actual structures vary from

MEMSCAPs values and should be verified. It is accepted that poly 1 and poly 2 have modulus of elasticity (E) of 131 GPa and 162 GPa, respectively. The Poisson ratio (ν) for polysilicon is 0.22 [36].

Table 4.1: PolyMUMPs run 71 data provided by MEMSCAP

150 mm wafers					
Material	Thickness	Standard Dev	Sheet Res	Resistivity	Stress
	(A)	(A)	ohm/sq	$ohm-cm$	MPa
Nitride	6,074	277			96 T
Poly 0	5,118	14	40.4	2.07E-03	26 C
Oxide 1	19,181	461			
Poly 1	20,007	79	16.4	3.28E-03	6 C
Oxide 2	7,432	223			
Poly 2	15,026	115	26.4	3.97E-03	7.3 C
Metal	5,111		0.054	2.76E-06	23.62 T

To calculate the stress in the poly 1 and poly 2 layers, cantilevers with lengths ranging from 50 to 250 μm in 50 μm increments were used and are shown in Figure 4.2. The cantilevers were released per the MEMSCAP instructions and were optically measured using a Zygo NewView 5000 Interferometer.

The cantilever deflections for two wafers were collected and the deflection for identical beams were averaged resulting in the data in Figure 4.3. The curves consist of the data for the maximum deflection for each cantilever length and are linked together. The internal stress of the cantilevers can be calculated using

$$M_1 = wL^2/2 \rightarrow w = 2M_1/L^2 \ \ (\mu m) \ \ [37] \tag{4.1}$$

$$|\sigma_{int}| = |Mt_p/(2I)| \rightarrow |M| = |2I\sigma_{int}/t_p| \ \ \ (MPa) \ \ \ [38] \tag{4.2}$$

$$w = -4I\sigma_{int}/(t_pL^2) \ \ (\mu m) \tag{4.3}$$

$$y_{max} = wL^4/(8EI) \rightarrow w = 8EIy_{max}/L^4 \ \ (MPa) \ \ \ [15] \tag{4.4}$$

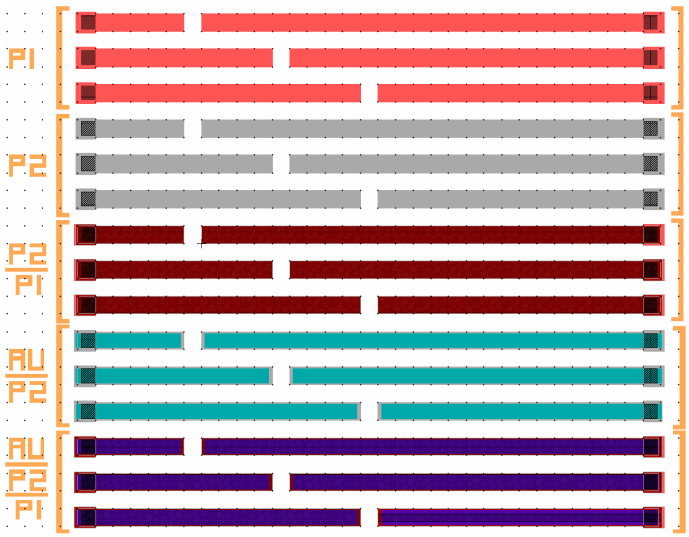

Figure 4.2: Layout of cantilever stress structures made up of five different material combinations and lengths.

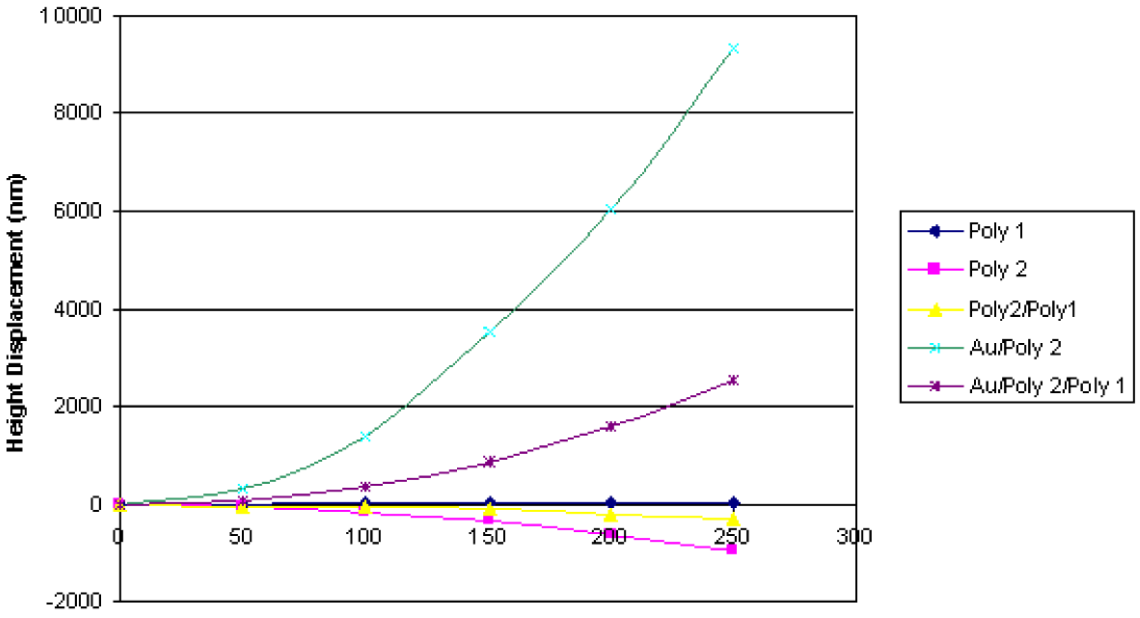

Figure 4.3: Deflection of PolyMUMPs cantilevers, each data point is the deflection for a cantilever of that length and the line is made up of the deflection of the combination of 5 cantilever lengths.

$$\sigma_{int} = 2Et_p y_{max}/L^2 \ \ (MPa) \tag{4.5}$$

where t_p is the polysilicon thickness, L the cantilever length, I the moment of inertia, σ_{int} the internal stress, M the moment, E Young's modulus and Y_{max} the maximum deflection. Substituting Equation (4.1) into (4.2) results in Equation (4.3) and setting (4.4) and (4.3) equal to each other results in Equation (4.5). This allows the calculation of the internal stress of the cantilever from knowing the Young's modulus, maximum deflection, material thickness, and cantilever length. The resulting σ_{int} for both poly 1 and poly 2 are located in Table 4.2. The first two data points for both materials are far removed from the other three data points so the last three data points were averaged, resulting in a calculated σ_{int} for poly 1 of 0.537 MPa and -7.579 MPa for poly 2. This may have been caused by some damage caused during the release on some structures. Cantilever deflections were measured from two sample dies and most results had 10 nm or more difference, these were then averaged and for shorter beams this error is amplified.

Table 4.2: Calculated σ_{int} from measured cantilever beam deflection

Cantilever Calculated Stress		
Cantilever Length μm	poly 1 σ_{int} (MPa)	poly 2 σ_{int} (MPa)
50	-0.103	-5.904
100	1.188	-8.461
150	0.595	-7.618
200	0.56	-7.564
250	0.457	-7.555

The calculated σ_{int} for poly 1 does not compare with those of MEMSCAP. This could be due to poly 1 going through the poly 2 anneal causing the stress to be relaxed from the value previously measured. The reduced stress is caused by further diffusion of dopants through the polysilicon, reducing the dopant gradient. While, at the same time, the σ_{int} for poly 2 closely matches the values published. Poly 2

is only exposed to one anneal, its own. The stress is then measured and the metal is applied at relatively low temperatures and so does not affect dopant distribution causing relaxation of stress.

4.3 PolyMUMPS Structure Designs

PolyMUMPs was used to create test structures that individual carbon fibers could be mounted onto and then tested. Two types of structures have been designed for testing the samples. First, a force device that will consist of pulley (floating bondpad) and anchor structures, shown in Figure 1.5, will be used to measure the deflection caused by intercalated fibers. Calculations using the device design and material properties, along with basic mechanics, will be used to calculate the force generated by the carbon fiber. These devices have armatures that are constructed of poly 1 or poly 1 and poly 2 with various lengths from 120 μm to 40 μm in 20 μm increments. This will vary the required force to obtain specific deflections.

The second device is made up of four conductive contacts as shown in Figure 4.4, equally spaced from each other to perform a four point probe test. This device will provide the data needed to calculate the impedance of intercalated carbon fibers for both the applied direct current and small signal (AC). The two inner contacts have a metal width of 5 μm to reduce the contacts effect on the measured values.

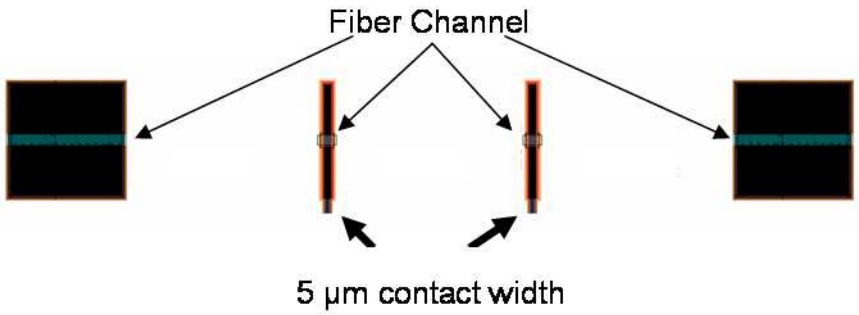

Figure 4.4: Four point probe impedance testing system for Thornel® P-100 carbon fiber. Each structure has 250 μm between them, for a total distance of 1 mm.

The testing process includes securing the carbon fibers onto the PolyMUMPs wafer test devices with silver epoxy followed by metalization with electron beam evaporation. The wafer will then be placed into a chip carrier and wire bonded to the external pins to improve the testing efficiency. The intercalate material will be inserted before the chip carrier is sealed. Once this is completed, the fiber is ready for testing and data will be collected. This will be coordinated with the use of both `Coventorware`® software for mechanical modeling and various computer software programs to determine the mechanical force and impedance models for the `Thornel`® P-100 carbon fibers intercalated with H_2SO_4.

4.3.1 Analytical Modeling of Force for Test Structures. Through the iterative process of design, the structures that were constructed were altered from having four supporting beams to only two, one on each side. Testing of the four beam designs showed that these structures were fragile because of the narrow beam width. The anchors on the substrate were narrow as well to match the four beam design and would often fracture before the beam. These calculations are based on the PolyMUMPs run #74 data when this change was made.

The design change made the calculations only slightly easier by making this a double-clamped beam with a center load. The design utilized the layering of poly 1 and poly 2 and has a different θ_{int}, internal stress, then each layer independently. Since the Young's moduli of both materials are 131 and 162 GPa, respectively, their values were weight averaged with

$$E_{poly12} = E_{poly1}t_{poly1}/(t_{poly1} + t_{poly2}) + E_{poly2}t_{poly2}/(t_{poly1} + t_{poly2}) \text{ (Pa)} \qquad (4.6)$$

where the thickness, t_{poly1} and t_{poly2}, are from Table 4.1 and the Young's modulus, E_{poly1} and E_{poly2}, of each material is used. This provided a reasonable estimate of the combined layers Young's modulus and resulted in a Young's modulus of 144.296 GPa. The θ_{int} for the two layers was then calculated using Equation (4.4) to be -4.767 MPa. This value made it possible to predict the correct height of the poly 1/poly 2

beam for any cantilever longer then 50 μm to within 6 percent of the data in Figure 4.3.

To confirm that the mass of the central pulley was not to great a load on the beam, the vertical displacement of the center mass due to gravity was calculated using

$$z = Mg{a_1}^3/(2Ebh^3) \text{ (m) [39]} \tag{4.7}$$

where the pulley's mass is M, gravity (g), beam arm length (a_1), Young's modulus (E), beam width (b), and beam thickness (h), for better imagery refer to Figure 4.5. This required the assumption that the beam mass was significantly lower than the pulley's mass. The maximum deflection from the pulley mass is calculated to be 11 pm for a 5 μm wide beam, which is negligible, particularly when compared to Figure 4.3.

Equation (4.7) was also used to calculate the potential force applied to the pulley structure by replacing the gravitational force, Mg, with the force (F). So that the deflection (x) of the pulley could be used instead of z, the Equation was

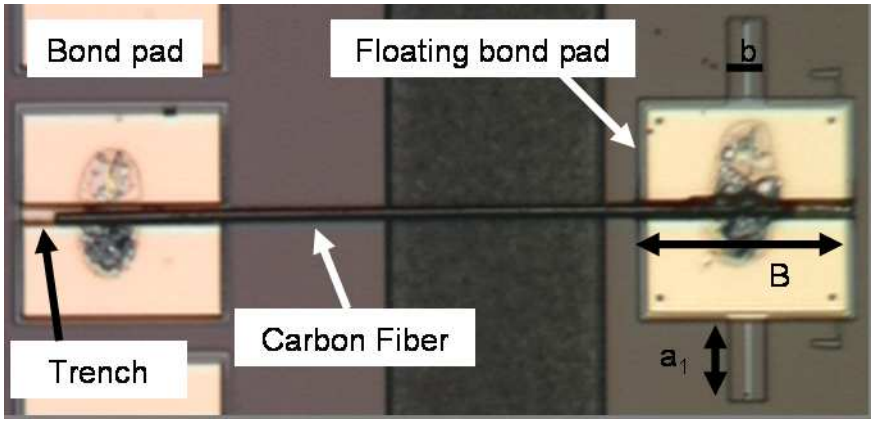

Figure 4.5: Image of redesigned pulley and anchor structure based on Kading design, the bondpad for the anchor has been attached to reduce the possibilities of wire run damage.

then solved for the force

$$force = -2xEhb^3/{a_1}^3 \text{ (N)}. \tag{4.8}$$

Some alterations were made to the inputs due to the change in force direction. The changes include switching the roles of the beam width and thickness. Effectively making h represent b and b represent h from Figure 4.5. This was accounted for by changing the names in Equation (4.8). A beneficial side effect is that the uni-axial internal stress θ_{int} is no longer relevant since the force is now horizontal. To simplify calculations, Equation (4.8) can be consolidated for each design to produce a spring constant given by

$$K = 2Ehb^3/{a_1}^3 \text{ (kg/s}^2\text{)}. \tag{4.9}$$

Kading has performed research with these structures and has previously calculated the tensile strength of PolyMUMPs silicon as 1.51 GPa [40]. This value was used as a basis to calculate the failure point of the designed structures. The maximum force for the structure can be calculated using

$$F_{max} = 2hb^2T_{max}/3a_1 \text{ (N) [39]} \tag{4.10}$$

where T_{max} is the tensile strength of the material. To simplify matters more, the length of travel before breakage of the pulley can be calculated easily by using

$$x_{max} = F_{max}/K \text{ (m)}. \tag{4.11}$$

The data from the above calculations for the structures designed in PolyMUMPs run #74 can be found in Table 4.3.

4.3.2 Coventorware Modeling of Test Structures. `Coventorware`® modeling was accomplished using a fixed-fixed beam 200 μm long and 20 μm wide consisting of poly 1, and poly 2 with a small mass in the middle, that was 2 μm wide

Table 4.3: Analytical modeling data for PolyMUMPs test structure

a_1 Length (μm)	beam width (μm)	K (Kg/s^2)	max Force (mN)	failure point (μm)
100	20	8088.206	14.013	1.733
100	15	3412.212	7.882	2.31
100	10	1011.026	3.503	3.465
100	5	126.378	0.876	6.93

for attaching the displacement load, Refer to Figure 4.6. The beam width was then scaled down in 25 % increments to 15, 10 and 5 μm. The Coventorware models force became non-linear at some point in these results. The 10 μm beam width structure was the first design with a displacement of less than 10 μm that this was apparent in. It produced a non-linear result, with a peak force of 15.310 mN at 9 μm of deflection, while the analytic results were 9.099 mN resulting in a 40.53 % deviation. This could very well be applicable, the narrower the beam width the lower the displacement required before the beams movement becomes non-linear. The analytical approach is simplified and does not take into account the point at which the beams response will become non-linear. Referring to Table 4.3, a displacement of 3.465 μm was the failure point for this structure. The computer model was simulated with the 3.465 μm displacement resulting in a force of 4.122 mN, which is a 15.94 % deviation.

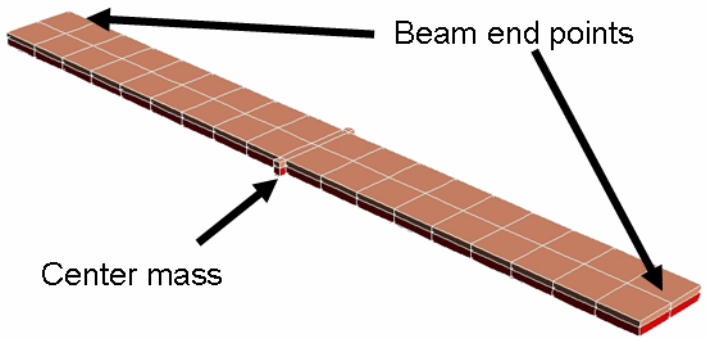

Figure 4.6: Floating bond pad model, 200 μm long and 20 μm wide with 2 μm wide center mass used for `Coventorware`® modeling.

The diversion between the two techiques is shown in Figure 4.7. This procedure was done for the remaining structures and is shown in Table 4.4.

Table 4.4: Comparison of analytical and software force results at the analytically calculated deflection distance of structural failure

Beam Details		Failure	Analytical	Coventorware	Percentage
a_1 length (μm)	beam width (μm)	deflection (μm)	failure point (mN)	failure point (mN)	deviation %
100	20	1.733	14.013	13.852	1.149
100	15	2.31	7.882	8.365	5.774
100	10	3.465	3.503	4.122	15.940
100	5	6.93	0.876	2.252	61.100

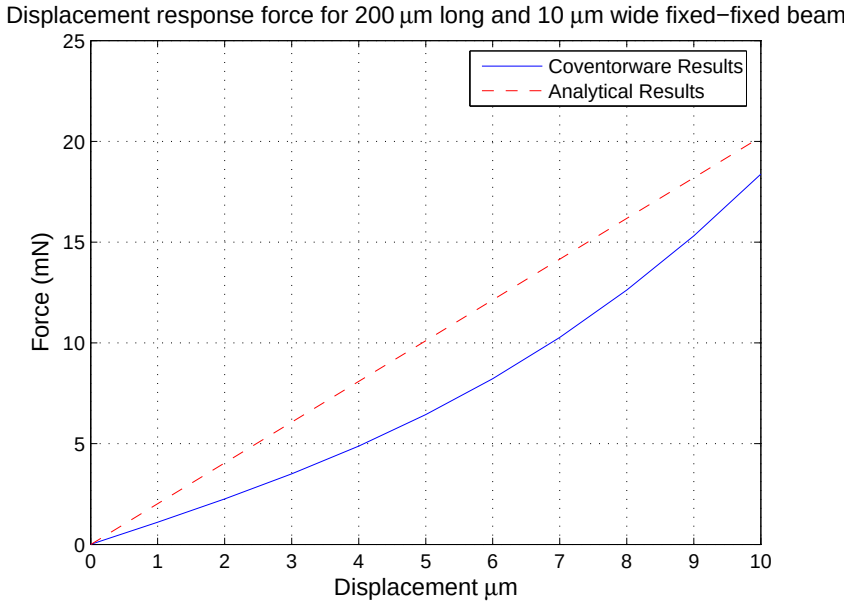

Figure 4.7: Force response to displacement of a 200 μm long by 10 μm wide fixed-fixed beam with center load.

4.4 Fabrication of Test Devices

The following process was followed to complete the research of mechanical and electrical characterization of carbon fibers intercalated with sulfuric acid. First,

the fibers were placed into depressions designed into MEMS structures with two micromanipulator probe station tips as shown in Figure 4.8. The MEMS structures were created to measure the PECT effect and electrical characteristics. During this process, the fibers were bonded into place so that they would be electrically and mechanically bonded to the MEMS structures. Once mounted, the PolyMUMPs die was placed into a chip carrier and secured with crystal bond and wire bonded to the external pins. While at this stage, a cathode material (in our case gold but usually this is platinum) was bonded into the chip carrier to an external pin to complete the electrochemical circuit. The cathode was not always added since it was incorporated into the PolyMUMPs die in later iterations. The chip carrier was either covered and sealed with a glass cover or the container filled with sulfuric acid and then sealed. All of these tasks provided their own set of difficulties that needed to be overcome. The following paragraphs will go into the methods that were developed and tested to effectively complete the above process.

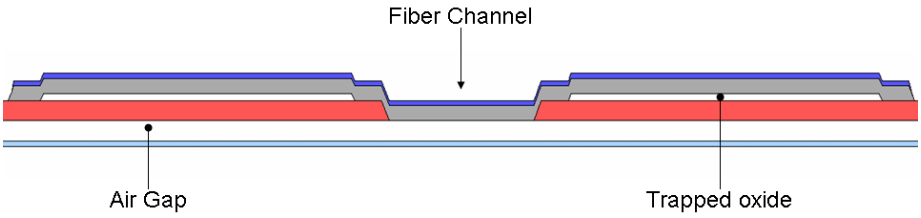

Figure 4.8: Cross section of PolyMUMPs pulley structure.

4.4.1 Fiber Mounting. The most difficult and time consuming portion of completing this research involved securing the fibers so that they would stay in place once exposed to sulfuric acid and sealing the chip carrier from the atmosphere. Sulfuric acid is very corrosive and destroys most materials. Through the previous personal experience of Kading, it was known that the Epotech H-27D silver epoxy was unable to stand up to H_2SO_4 even after curing [40]. The Epotech H-27D did not dissolve instantaneously when placed in contact with sulfuric acid so its use was

continued with the understanding that if bonding with it, the epoxy needed to be protected from the H_2SO_4. When mounting fibers they often need to be broken to the desired length the actions are shown in Figure B.7.

4.4.1.1 Electron beam with photoresist mounting attempt. One of the first methods attempted was to electron beam (e-beam) evaporate gold over the bond pads. Originally, this process was envisioned as a way to both electrically and mechanically bond the fiber in place using metal. In this case, the H-27D was used to hold the fibers in place until metalization occurred. Due to the expense of gold and the thicknesses that can be achieved by this method, a trench was created in the bonding pad so that approximately half of the fiber would be cupped in place, providing a smoother transition for the gold to bond between the bond pad and the carbon fiber [40]. Otherwise, the height difference was too significant, 10 μm, and the gold would never be able to bond the two surfaces together. A thin layer of titanium (Ti), 500 Å to aid gold (Au) adherence was used followed by 2000-5000 Å of Au. To perform this, two types of photoresist (PR) were used, Micro-Chem LOR-3A followed by Micro Chem SU8-5, a negative PR. At first, three layers of 0.3-μm LOR-3A PR were used to increase the thickness of the PR to make certain there was a drop off for metal liftoff and to ensure the carbon fiber was protected from metalization. A layer of SU8-5 PR 3-μm thick was then spun into place, soft baked, and exposed with the Karl Süss MJB3 UV contact mask aligner. LDD-26W developer was then used to develop the PR; opening holes for the e-beam evaporated gold to deposit on the desired locations of the wafer. After the deposition of Ti and Au, the residual metal was removed by placing the wafer into 1165 stripper at 90 °C leaving the metal on the mounting fixtures. The fiber was then ready for testing as shown in Figure 4.9.

There were many issues with this process and numerous modifications were made to try and account for them. First, the LOR-3A PR was soft baked at 170 °C for two minutes for each layer. This caused the lower layers to become very hard to remove when developed. The application process was modified and only one layer

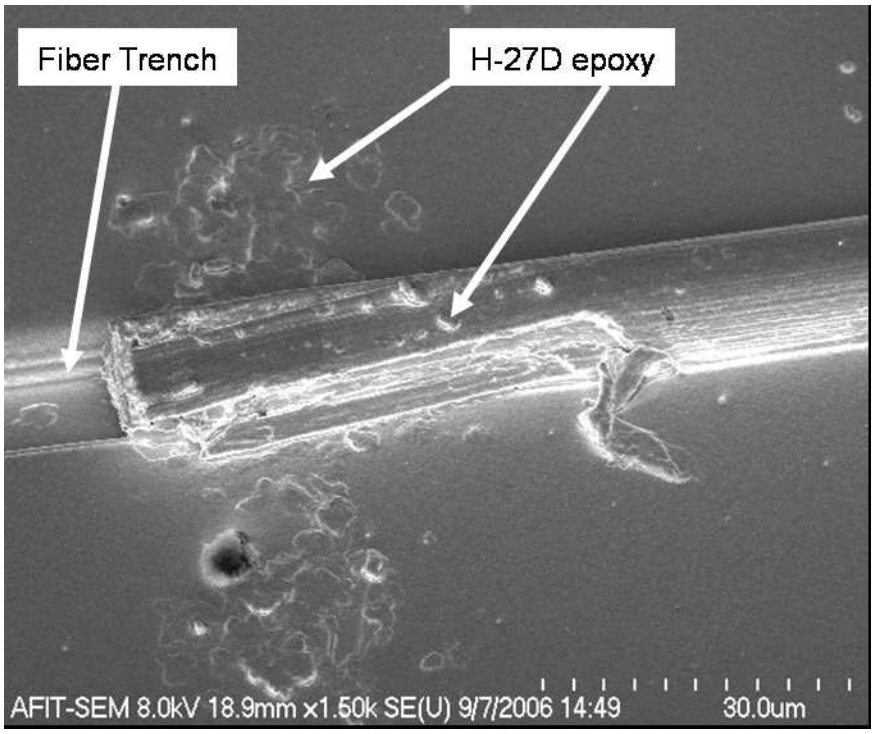

Figure 4.9: Gold plated fiber in trench on mounting fixture, drops of epoxy are seen on the fiber and surface

of LOR-3A was applied followed by the second type of PR. The strength of the LOR-3A and SU8-5 PR was also a problem, often fracturing the fiber during the exposing, developing and stripping processes. Edge beading was a critical issue, the wafers were 3200 μm x 3200 μm, which led to the creation of very large edge beads that degraded the exposure process causing the PR to not develop properly. This left residue on the surface of the wafer and possibly even coated the surface of the fibers. To correct this, the spinning speeds for PR application was modified. One other variation was tried sputtering 5000 Å of gold on the die instead of using e-beam evaporation.

Some modest success was achieved with this method, a few fibers were actually intercalated and provided mechanical results that could be processed as discussed in Section 5.5. In most cases the fibers were damaged and not testable. The remaining fibers would start to intercalate and the Au coating would lift and begin to peel away,

eventually detaching from the MEMS structure and obscuring the fibers movement as shown in Figure 4.10. This could have been caused by the reaction of the epoxy and/or Ti layer with the H_2SO_4. When fibers were intercalated, their width would increase by approximately 10 %, and then decrease in size when de-intercalated. This action would allow the acid to move underneath the Au and react with the epoxy and Ti. We did notice that most of the fibers that did perform as desired had the epoxy covering the fiber, this was a sign that the Au even at 5000 Å was not strong enough to bond the fibers.

Some of the structures tested would not move, this appeared to be caused by floating bond pads that were still attached to the substrate. This could have been caused by not releasing the structures long enough or the bonding of the trench in the floating bond pad to the substrate. This led to a reduction in floating bond pad dimensions on subsequent PolyMUMPs runs so that the hydroflouric acid (HF) exposure time would not need to be increased. In addition, an anchor 1 layer was

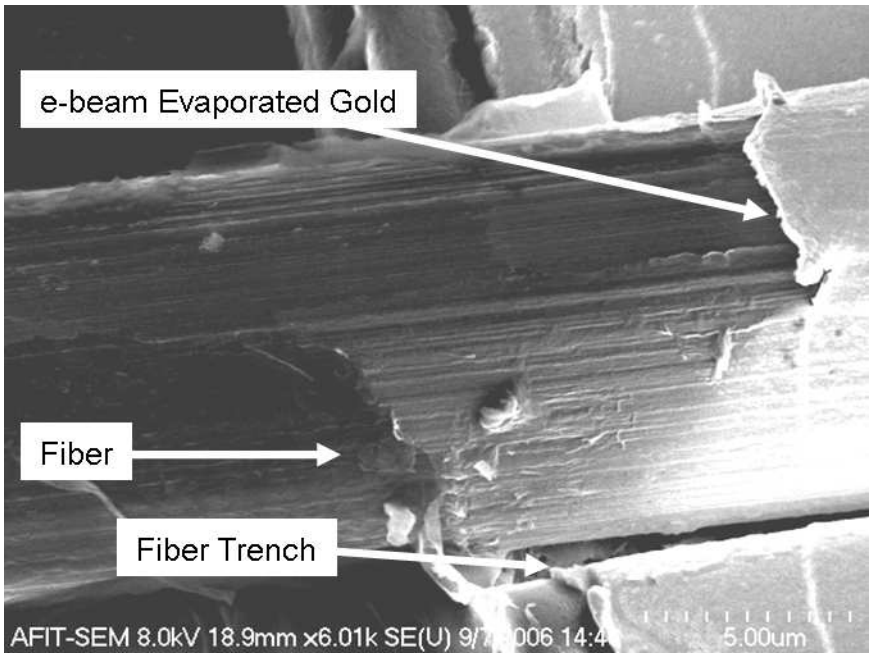

Figure 4.10: e-beam evaporated Au on fiber in trench created in mounting fixture with approximately 2000 Å of gold applied.

placed under the poly 2 layer of the trench to provide more clearance for the floating bond pad so that the HF could remove the oxide layers.

4.4.1.2 Paraffin protected epoxy mounting attempt. A previous researcher used wax to seal the chamber where a carbon material was exposed to an intercalation material [41]. To test the usefulness of wax e.g. paraffin, silver epoxy was placed onto two glass slides and a piece of silicon wafer. A droplet of paraffin was melted over the epoxy and the samples were then placed into separate sulfuric acid baths. After 1.5 hours, the glass slide samples showed minor signs of paraffin loss. The paraffin did not appear to flow as desired over the epoxy on the glass slides. The epoxy on the silicon wafer was unharmed and completely sealed. The silicon wafer was then submerged in HF for ten minutes to identify any degradation and no loss of mass was noted. With these promising results, further research was accomplished to test the feasibility of using paraffin for the intercalation of H_2SO_4.

It was observed that paraffin melted freely at 57 °C and was solid at 50 °C when no liquid was in contact with it. Several carbon fibers were mounted onto a PolyMUMPs die. The sample die was then placed on a heated stage for the micromanipulator probe station. The heating stage was set to 53.9 °C and a 3-μm probe was used to pick up small droplets of paraffin. The paraffin was applied to the bond pads to cover the epoxy. After releasing the die structures in HF, rinsing with DIW and then isopropanol, the die needed to be dried, removing any liquid. This was done by placing the die onto a hotplate at 45 °C causing the wax to become slightly liquidus where it interfaced with the die substrate. When exposed to a liquid the paraffin began to liftoff. At completion of the production process, the graphite fibers, paraffin, and silver epoxy were no longer bonded, thus demonstrating that coating structures with paraffin was not a viable option to protect the epoxy from sulfuric acid.

4.4.1.3 Solder powder fiber mounting attempt. Since the silver epoxy was reacting to sulfuric acid, other options to mount graphite fibers had to be ex-

plored. One potential option was the use of solder balls but they were still too large for our purposes. After further research, solder powder comprised of spheres that were of the proper scale to bond graphite fibers onto the PolyMUMPs test devices was found. Amtech Incorporated produces several lines of solder powder with various particle diameters. For the highest potential of success, the solder powder required good electrical conductance and low sulfuric acid reactivity. Tin is highly reactive and so a low tin content was required. One of Amtech's products fit this requirement with 10 % Sn/88 % Pb/2 % Ag, and particle sizes ranging from approximately 15-25 μm and a liquidus temperature of 290 °C and solidus temperature of 268 °C. To test the usefulness of this material, solder powder was applied to a PolyMUMPs die at various temperatures ranging from 265 °C to 340 °C, with and without flux. All results showed little promise. At times, the solder powder would flow over the gold contact on the MEMS structures and after a few minutes congeal into droplets on the structure causing discoloration and damage, stopping the addition of any more solder, reference Figure 4.11. The gold/silicon eutectic temperature is near 290 °C, therefore a 270 °C application temperature was expected to be optimal for the desired results. This was not the case and the temperature could not be reduced

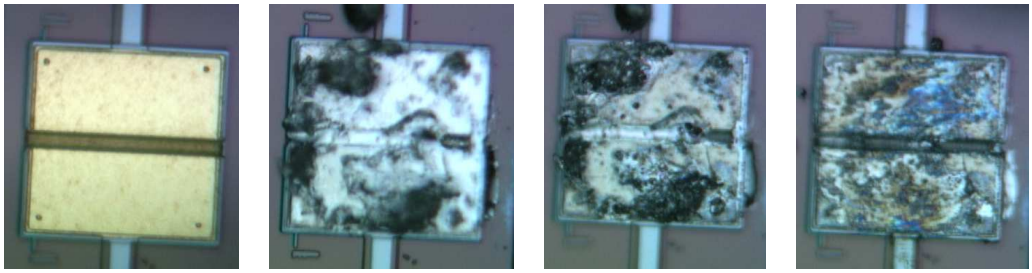

(a) (b) (c) (d)

Figure 4.11: 270 °C solder powder test: (a) original contact pad prior to application of solder, (b) solder covers contact pad after initial application, (c) five minutes after solder application the solder pulls in and creates pools of solder leaving gold on contact exposed, (d) reapplied solder removing the previous solder with no new solder adhering to pad surface

further because of the solidus temperature. There was one other composition 5 % Sn/92.5 % Pb/2.5 % Ag that could have worked but had a solidus temperature of 280 °C, 12 °C higher then the currently tested product removing it as an option.

4.4.1.4 Revisiting metal liftoff to mount fibers. The solder powder mounting attempt led to revisiting the metal liftoff process. In this approach, one of the photoresists was changed. The negative PR, SU8-5, was exchanged with a positive PR, Shipley 1805. Fibers were mounted to the PolyMUMPs die using the Epotech H-27D silver epoxy. The epoxy was put onto the mounting pads and the fibers put into place. To try and ensure that the fiber would not rip out of position, the epoxy was also placed over the fiber. If required, the epoxy was applied twice: first to secure the fibers in the channel and once more to ensure the epoxy covered the fiber. The epoxy was cured at 150 °C for one hour after each application. The die was then rinsed with DIW, blown dry with N_2 and dried on a hotplate at 125 °C for 5 minutes. The sample dies were 3200 μm square and could not be secured to the chuck on the spinner. Therefore, a standard glass slide was cut in half and Micro Chem SU8-5 epoxy was spun onto the glass slide. The sample chip was placed in the middle of the slide and soft baked. This provided a suitable base for securing the die to the spinner chuck. LOR-3A was spun on with a 500 RPM ramp speed for 10 sec up to 5500 RPMs for 30 sec. The die was then softbaked for 2 minutes at 170 °C. Next, 1805 was applied and spun at 4000 RPMs for 30 seconds. The die was softbaked again for 75 seconds at 110 °C. The sample was exposed for 5.5 seconds on a Karl Süss MJB3 UV contact mask aligner at 274 Watts/cm^2 (λ_0=405 nm). The sample was developed on a spinner with a constant flow of LDD-26W for approximately 75 seconds. The sample was rinsed with DIW and dried with N_2. The fibers broke at some point in the process, most likely at the development step. The SU8-5 PR is considered an epoxy and is hard to remove. When SU8-5 does come off it is in chunks and would place excessive force on the fibers, snapping them off.

4.4.1.5 Fiber mounting with gold using electroplating. Electroplating became an option when all other attempts failed. This technique involves placing a conductive material into a gold solution and applying a voltage to the metal to be plated. This voltage attracts the gold molecules which are then separated from the solution and deposited on the metal. The hopes were that if a carbon fiber was laying across a gold pad it would make electrical contact and hold a charge, gold plating the fiber, with the gold pad eventually bonding both the fiber and pad after the addition of approximately 5 μm of gold. To test this theory, glass slides were cleaned with buffered oxide etch to roughen the surface. Then 1500 to 2000 Å of gold were evaporated producing two gold pads a quarter of an inch apart and a quarter of an inch in width. A fiber was attached to the glass slide spanning both gold pads with H-27D epoxy. This was done because of the concerns that the acid was consuming the epoxy underneath the gold, causing the gold to peel off, the decision was made to let the acid remove the epoxy and attempt to bond the fiber to the gold with the newly added electroplated gold. We tried to maximize the PR height by using two application methods to make sure that the 10 μm thick fiber was covered between the two gold bond pads. If the fiber had a charge on the surface and was exposed to the electroplating solution anywhere but over the bond pad undesired electroplating would occur. Two slides were coated with 4 layers of Shipley 1813 photoresist resulting in a PR thickness of 2.25 μm. Another two slides were coated with 3 layers of Micro Chem LOR-3A and 4 layers of 1813 with a PR thickness of 4.01 μm. The 1813 was soft baked at 110 °C for 75 seconds for each layer. The LOR-3A was soft baked for 2 minutes at 170 °C per layer. The 1813 and 1813/LOR-3A PR samples were then exposed for 40 seconds using the Karl Süss MJB3 UV contact mask aligner and developed with LDD-26W to expose the gold lines for electroplating. The 1813/LOR-3A PR was approximately 1.75 μm thicker than the 1813 layers alone. The LOR-3A fibers were broken off not far from the PR boundary but enough of the fiber remained to complete the test. The 1813 had some

PR trapped under the fiber on the gold and even with subsequent development could not be removed, as demonstrated in Figure 4.12.

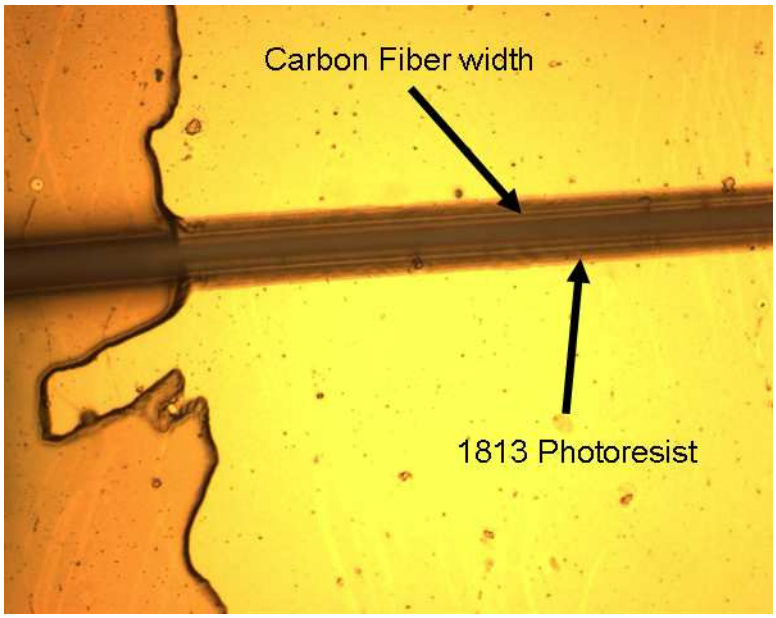

Figure 4.12: Carbon fiber mounted onto a glass slide after development with LDD 26W with 4 layers of 1813 PR, note the line where the PR ends and the shadow under the fiber which is 1813 PR

The samples were transported to AFRL where they were electroplated with gold. During the electroplating process, gold only bonded to the gold pads that had direct contact to the voltage source. The fibers were not making good enough contact to conduct electricity across the fiber to the pad on the opposite side. One fiber was electroplated with increasing voltage and current limits. The pads on this sample showed a considerable increase in gold thickness but with the naked eye no sign of electroplating was occurring near the fiber. After the test, this was verified by placing the sample in question into the SEM. Some gold electroplating of the fiber had occurred as shown in Figure 4.13. This was after about an hour and a half of electroplating. Figure 4.13 also shows very prominently the layer of PR trapped underneath the fiber.

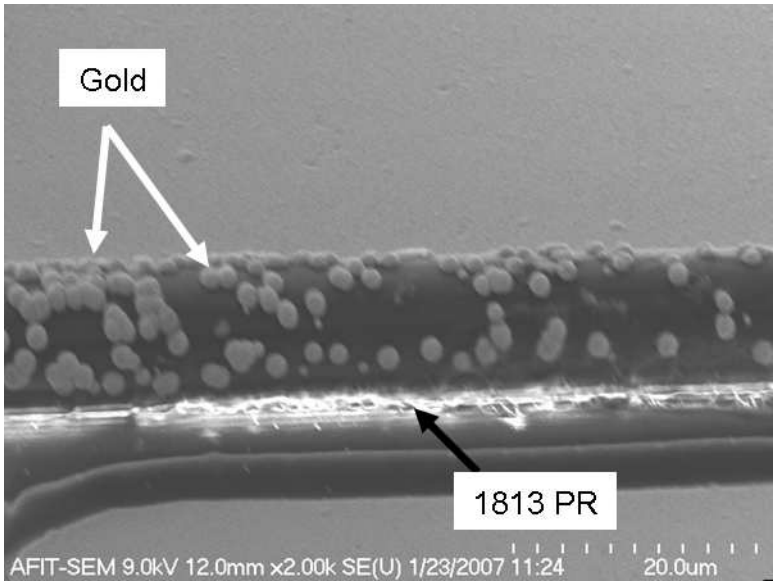

Figure 4.13: Gold electroplated fiber after approximately 1.5 hours of electroplating with 1813 PR trapped underneath

The goal of this test was to determine if it was worth moving forward to electroplate a die with fibers mounted. This would have required the production of a holding fixture for the die. Also, the voltage source would only be able to make contact with one of the bond pads and the reaction would depend on the fiber as a conductor to place the voltage on the other bond pad. This was clearly not feasible so testing in this direction ceased.

4.4.2 Chip carrier sealing. While trying different methods to mount carbon fibers onto PolyMUMPs dies, the opportunity arose to find ways of sealing the chip carriers so that they could contain the 96 % H_2SO_4. The chip carriers that were on hand came with glass and ceramic lids. Since, the desire was to observe and monitor the reaction the glass lids were chosen. Crystal bond 509 (CB) manufactured by Electron Microscopy Sciences, a material that melts at approximately 120 °C was used to secure the testing die inside the chip carrier, so this became an obvious choice. Unfortunately, the covers needed to be placed after the addition of the acid exposing it to high temperatures. Paraffin was then tried since it had a low

melting temperature and could be placed around the edges of the chip carrier opening prior to adding the acid. This was not very useful, paraffin was very sensitive to temperature and if the temperature was too high it would flow down and into the carrier potentially bonding onto the fibers. Sulfuric acid has a high viscosity and will wick onto a glass lid when it comes in contact. This proved to have the same effect as our approach to seal epoxy on the fibers with paraffin, the paraffin would get wet from the acid while hot and begin to peel off and quickly come off. While performing this test, a method to apply paraffin without heating the die was found. A low temperature hot glue gun was used to melt the paraffin onto the desired location on the outside of the chip.

It became apparent that the chip carrier needed to be sealed or mostly sealed prior to adding acid, allowing the sealant to bond properly. Efforts were made to drill through the bottom of the chip carrier, so that the carrier could be sealed on the top and then have acid injected through the bottom taking care not to get the surface wet and then sealing it. The ceramic of the chip carrier proved to be too hard and brittle to drill. The next obvious step was to place holes in the glass lid. To achieve this, diamond dremel bits for glass work were used to drill two very small holes into the glass lids. Two holes were needed to provide a path for the air pocket trapped under the lid to escape as the acid was added. Crystal bond was used to seal the lid by heating the chip carrier to 120 °C without acid present. CB was applied by grasping a small piece with tweezers and rubbing it along the outer edge of the chip carrier. The lid was then put into place and another layer of CB was added to the outside of the chip carrier on the edges of the lid as shown in Figure 4.14. Another technique was found after several tests were completed. This technique created mounds of CB around the acid holes prior to adding the acid. Once filled with acid these mounds were capped with CB, sealing the chip. This allowed us to seal the chip and stop the acid from leaking prior to testing. During the intercalation process hydrogen was released inside the chip carrier eventually building up enough

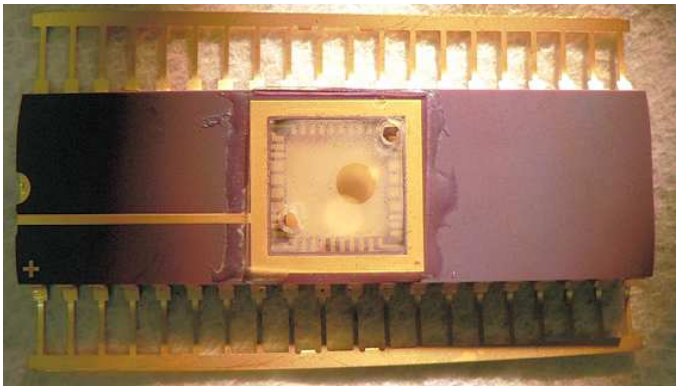

Figure 4.14: Chip carrier cover with 2 holes for the addition of H_2SO_4 and secured with CB.

pressure to cause the acid to seep out from around the CB. This meant that a perfect seal could not be provided in these cases.

4.4.3 Data Collection. Previous AFIT researchers have written some programs using `Vee`® software, similar to `LabVIEW`® . They wrote three programs. Fiber.vee was written to work with Agilent 4284a Precision LCR meter, and the Agilent 6624a DC power supply. This program measured the impedance versus phase (ZTD), series capacitance versus series resistance (CSRS), and series inductance vs series resistance (LSRS). This program would start off applying a base intercalation voltage and increase this voltage in steps up to the desired ending voltage where it closed. At each voltage step the 4284A would measure ZTD, CSRS, and LSRS for frequencies ranging from 20 Hz to 1 MHz. The second program Fiber2.vee was identical to fiber.vee except that it would step the intercalation voltage back down once the peak voltage was reached. The last program FIBER_SWITCH_SPEED.VEE collected the ZTD, CSRS, and LSRS from the 4284A while applying a pulsed wave to the fiber using an Agilent 33250 function/arbitrary waveform generator. During the process of completing this research, the Fiber.vee program was modified to enable the creation of one file for each fiber run. The software now allows the operator to select upper and lower intercalation voltage limits, step sizes and incorporated a file naming process. The operation and setup for this program is located in Appendix A.

4.5 Chapter Summary

Chapter four discussed the PolyMUMPs process, and material properties modeling. Providing both Equations and a description on how the internal stress of a material can be calculated. Two methods were also used to calculate the force produced by the movement of the floating bond pad using analytical and computer aided modeling. This chapter culminated in the various fabrication processes that were tried throughout this research.

V. Results and Analysis

Through the process of completing this research six types of surface treated Thornel P-100 fibers were tested and evaluated, although no intercalated impedance measurements were completed. The fibers were subjected to SEM examination, probing with a Raman microscope, and impedance measurements, which were taken using an Agilent 4284A Precision LCR meter. Also included are the results from a test where a graphite fiber was intercalated with sulfuric acid culminating in the movement of a MEMS actuator.

5.1 Fiber Treatment

The Cytec, formerly BP Amoco, `Thornel`® P-100 fibers were received from AFRL. The fibers were heat treated at 400 °C for 30 minutes to remove the sizing put in place by the manufacturer to bond the fiber strands into 2000 fiber tows. These were the fibers from which all testing was based. Some of the carbon fibers were sent to Oklahoma State University where they all underwent anodic oxidation in nitric acid for 30 seconds to 2 minutes and two of the samples were also heat treated in a vacuum at 1150 °C for 1 hour. These methods were discussed in several articles by Peter Sherwood's research group [42, 43, 44].

Sherwood's research group used X-ray photoelectron spectroscopy (XPS) to study the effects of electrochemically oxidizing E-120 carbon fibers with 1.0 M nitric acid. As a side note, this procedure does not create a graphite-nitric acid GIC. Graphite-nitric acid GICs are synthesized by exposing graphite to nitric acid vapor [45]. Kozlowski verified that no signs of nitrogen were present in their samples via XPS or infrared measurements [46]. Chemically, the C-C bonds on the outer surface of the fiber breaks and hydroxide (-OH^-) bonds form at low voltage potentials producing hanging C-O-H bonds. As the potential is increased, the bonds change to "bridged" structures, which are defined as C-O-H-O-C. To accomplish this, one of the C-O-H bonds loses a hydrogen atom and then bonds to the hydrogen atom of its neighboring carbon atom and makes a hydrogen-bridge oxide structure (HBS) as

shown in Figure 5.1 [42,43,44]. The physical effects on the fibers include roughening of the surface when exposed to concentrated nitric acid with no effect observed in diluted acid. With electrochemical oxidation and exposure periods of twenty minutes, the fibers form slits parallel to the surface and if treated for extended periods of time, the outer surface will deteriorate [46]. Further, the conductivity of the fiber could decrease with anodic oxidation in nitric acid. Xie observed that when a fiber was exposed to 2.5 V or greater, the fiber would release a large amount of H_2 and O_2 for a short period coinciding with a ramp in the current. This surge in current quickly dissipated and approached zero, also reducing the reaction rate. Xie then theorized that either the carbon fiber became an insulator or the bridge structures had formed on the exterior surfaces of the fiber and between graphene layers so completely that the reaction was complete [42]. It has been determined that when electrochemical oxidation occurs at 0.5 Amps, the carbon hydroxide bonds are replaced with HBS bonds on the surface of the carbon fiber. This occurs very quickly, in the first 10 seconds of the reaction, and then starts to trail off. After extended treatments, the conversion moves into the bulk and tell-tale signs of disordering in the structure are noted [44].

The results of Sherwood's research group was intriguing and provided the opportunity to test fibers with the sizing and surface treatment removed, as well as increased surface area. This could potentially cause the fibers to intercalate more efficiently causing the fiber to create yet more force when intercalated. The treatment applied to each fiber is shown in Table 5.1.

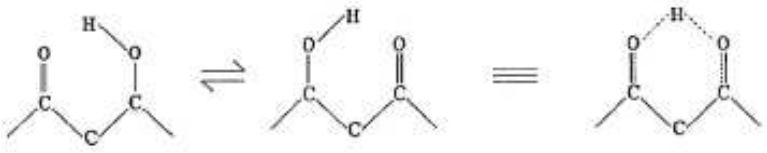

Figure 5.1: "Hydrogen-bridged oxide structure" [42]

Table 5.1: Fibers used for research and treatment

Fiber description	Anodic oxidation time (min)	1150 °C detreated? yes / no
F1	N/A	no
F2	0.5	no
F3	1	no
F4	2	no
F5	1	yes
F6	2	yes

5.2 Surface structure of fiber

To gain insight into the fibers physical appearance, the SEM was used. The following SEM images were taken using a Hitachi S4700. Wang stated that the physical texture of the fiber surfaces were changed after being electrochemically anodically oxidized in nitric acid [44]. Each fiber had different treatments so a visual comparison seemed appropriate.

Fiber F1, the original fiber is observed to have a smooth undulating surface without any holes or damage. Some of the fibers appear to have some material adhering to them and this might be left over sizing from the processing at the factory during production as shown in Figure 5.2. Sizing is the bonding material used to keep all of the fibers together for use in a tow, the fiber bundle. Figure 5.2(a) shows an image of a group of fibers to provide a feeling of the overall state of the fibers at this point. The second image in Figure 5.2(b) provides a closer view to provide better definition of the surface.

The second fiber, F2, shows some surface roughening as can be seen in Figure 5.3. The fibers have only slightly more materials on the surface then the original fiber F1 but definite grooves are observed on the surface parallel to the fibers length. Figure 5.3(b) shows a crack in the surface of the fiber and some surface roughening, this crack is much narrower then those observed on most of the other fibers as evidenced by the need to magnify the surface 15k times to obtain this image.

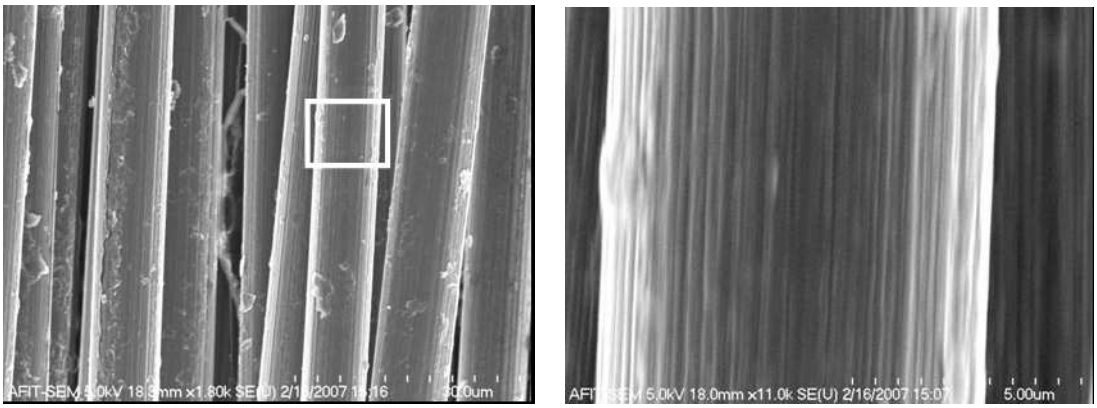

(a) (b)

Figure 5.2: Base `Thornel`® P-100 fiber, F1, with heat treatment at 400 °C for 30 minutes to remove sizing, all subsequent fibers have this treatment. (a) Wide view of group of fibers, (b) image of individual fiber at 11k times view.

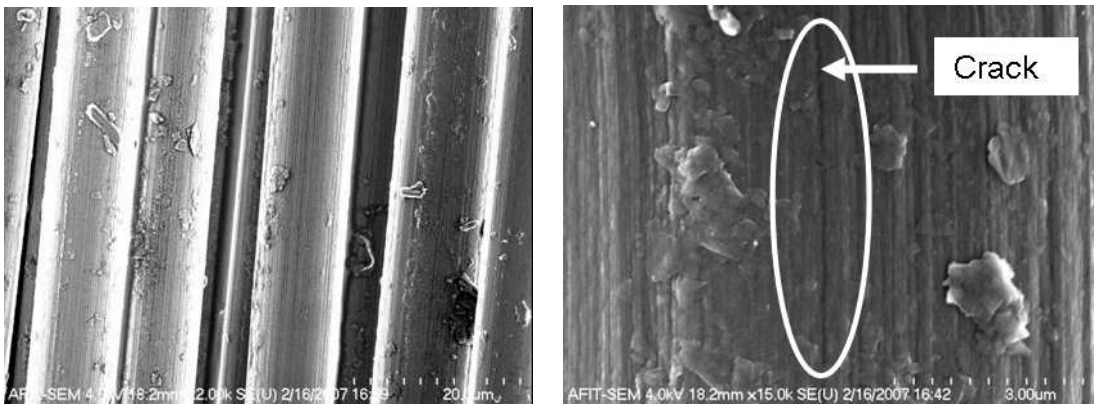

(a) (b)

Figure 5.3: Sample F2. (a) Wide view of group of fibers, (b) image of individual fiber at 15k times, note the fissure in the fiber and surface roughening.

Fiber F3, as shown in Figure 5.4, does not appear to differ much from F2 except that the surface of the fibers appear to have more material attached to them. Some deep grooves are seen in the surface of the fiber in Figure 5.4(b).

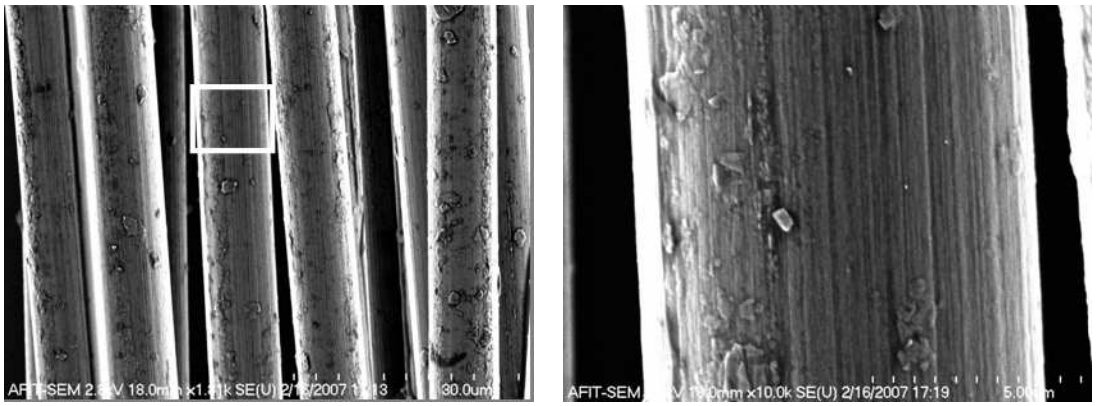

(a) (b)

Figure 5.4: Sample F3. (a) Wide view of group of fibers, (b) image of individual fiber at 10k times.

Sample fiber F4 shows a large number of fissures on the surfaces of the fibers in the zoomed out view, see Figure 5.5(a). The single fiber in Figure 5.5(b) shows the most surface damage thus far having both fissures and cracks that are visible on the surface of single fibers.

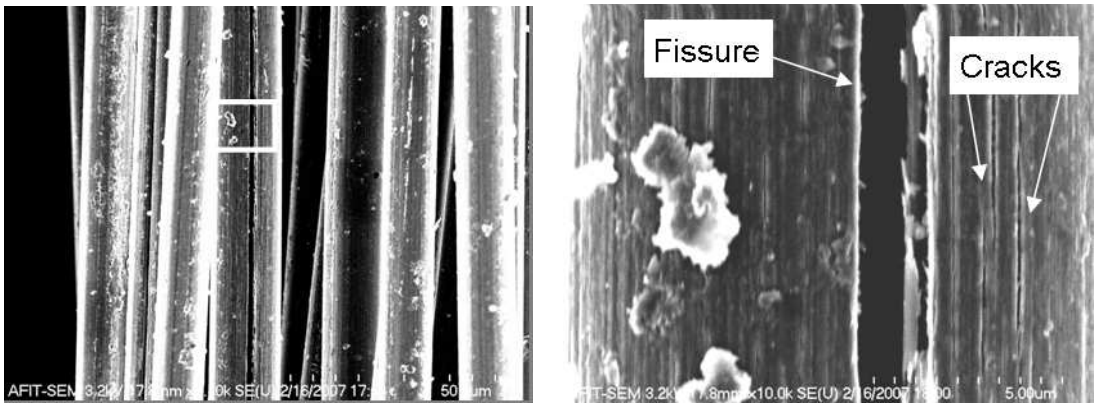

(a) (b)

Figure 5.5: Sample F4. (a) Wide view of group of fibers, (b) image of individual fiber at 9k times magnification, note the fissure and cracks in surface structure of fiber.

The remaining fibers were detreated in a vacuum at 1150 °C prior to their oxidation in nitric acid. The additional heat treatment for these fibers was to eliminate any surface treatment applied to the fiber surface by the manufacturer. Fiber sample F5 shows signs of exterior structure wear, a fiber on the left side of the wide angle view, referencing Figure 5.6(a), shows a prominent crack running down the side. Many of the other fibers have a roughened surface with particles attached, possibly dust. The single fiber on the right in Figure 5.6(b) shows what appears to be delamination of the fibers outer layer with the surface peeling away from the interior. This may have been caused by handling of the fiber after weakening of the surface from the treatment applied.

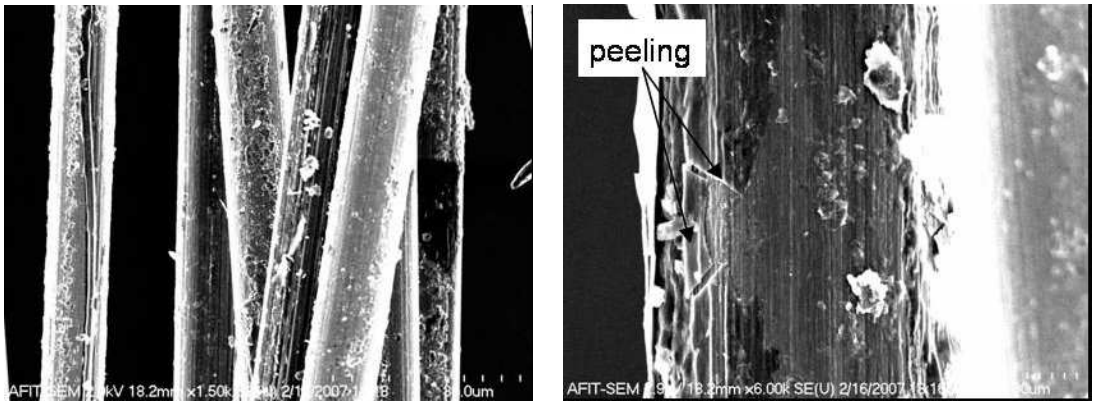

(a) (b)

Figure 5.6: Sample F5 (a) Wide view of group of fibers, note surface damage including a fissure in one and deep ruts in another, (b) image of individual fiber at 6k times magnification, this image shows the surface peeling away from the body of the fiber through some form of delamination.

Fiber F6, the last fiber, had less material on the surface than sample F5 despite the fiber in the middle of Figure 5.7. This result may have been caused by the removal of the material from the surface by the oxidation treatment. Figure 5.8(a) and (b) show the effects on the surface of the fiber and minute holes and a crack can be seen in the surface.

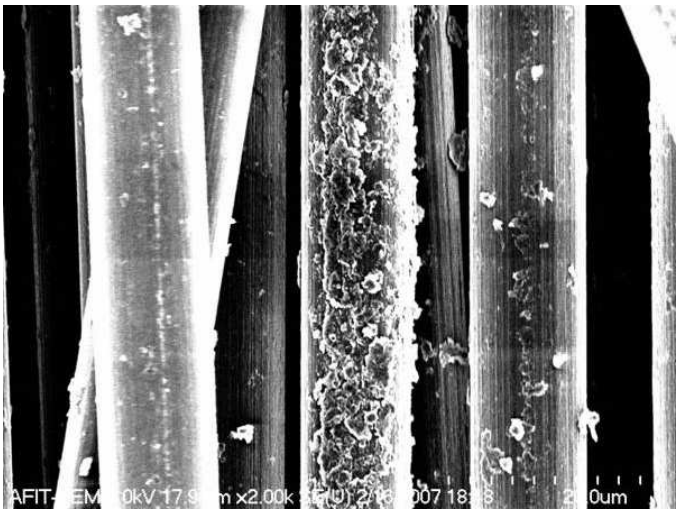

Figure 5.7: Sample F6 shows rutting on the surface in the wide view image of some of the fibers and yet another with a roughened surface that looks like it was in the early stages of delamination of the outer surface

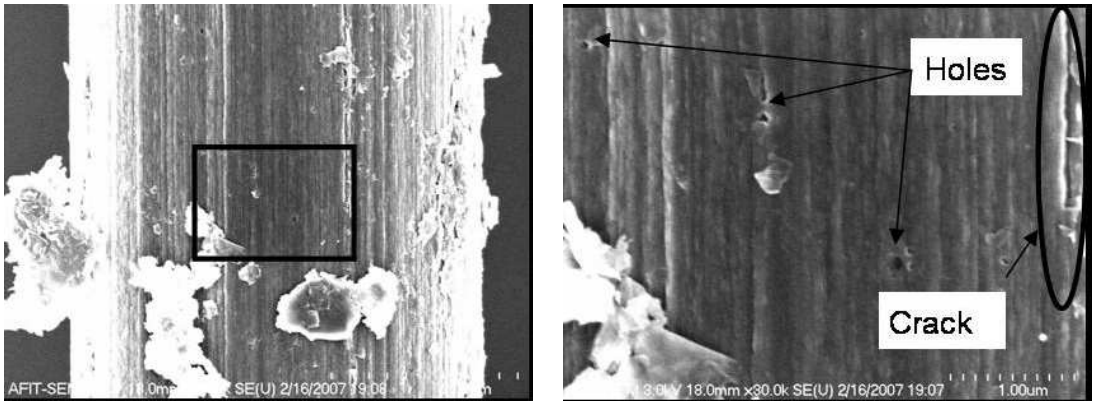

(a) (b)

Figure 5.8: Sample F6. (a) Image of individual fiber at 9K times magnification where rutting in the surface is evident as are pin holes enclosed in a box. (b) Box from (a) zoomed in to show definition of surface to include holes and a crack in the surface at 30k times magnification

5.3 Raman Spectroscopy of Thornel P-100 Fibers

Raman spectroscopy is a method that can be used to identify molecules by their vibrational frequencies. A monochromatic light source is directed at a sample and the frequencies reflected to the sensor are made up of three components. The three components consist of the original frequency from elastic scattering ω (Rayleigh scattering) and two sidebands. These sidebands are emitted by the sample and are offset from the original frequency ω by the vibrational frequencies of the molecules nuclear motion, Ω. When struck with the monochromatic frequency ω, the molecule returns a frequency of ω-Ω (stokes radiation) and ω+Ω (anti-stokes radiation). From quantum-mechanical modeling, the Rayleigh scattering frequency is returned when an electron moves to an excited state and then drops back into its original state. Stokes scattering occurs when the electron is excited and then falls back to a state higher then its original position. Anti-Stokes radiation does not always occur and requires the electron be in an elevated state prior to being driven with frequency ω. This causes the electron to be further excited and then when it returns to the ground-electron state, it produces a frequency that is ω-Ω [47]. These phonons are detected by the Raman spectroscope and data is collected about the number of phonons which translates into the intensity, and their frequency.

Carbon has three first order spectrum Raman shifts. Highly ordered graphitic carbon has a single peak at $\approx$1580 cm^{-1} and is the interior layers, E_{2g_2} with an intensity I_G. The second peak, D, is caused by disorder in graphite and occurs at $\approx$1360 cm^{-1} with an intensity I_D. The final peak is another disorder peak standing at $\approx$1620 cm^{-1} and is referred to as the bounding E_{2g_2}. When a carbon material is intercalated, the bounding E_{2g_2} peak becomes more prominent and the peak at 1580 cm^{-1} eventually disappears. Of the three, the first two are the primary peaks and a ratio of their intensity, I_D/I_G, provides insight into the disorder and provides a means to predict L_a, the dimensions of the in-plane crystallite in the structure [48]. The I_D/I_G ratio is tied to the number of graphitic edges, an increase in this ratio means there are more graphitic edges [49], but does not discount the validity of the previous

work. The 1580 cm^{-1} is the only peak that will be narrow and the width of the peak demonstrates the order within the carbon structure [27]. Eklund determined that the shift in the E_{2g_2} from 1580 to 1620 cm^{-1} is caused by the contraction of the in plane carbon to carbon bond, d_{c-c}, as discussed in Section 3.1.2 [50].

Data was collected using a Renishaw "InVia Raman Microscope" with a laser wavelength of 632.8 nm for specific testing setup details, see Table A.1. To validate the power level used for this test, a point on fiber F6 was tested with 10 %, 50 % and 100 % power with no sign of fiber degradation. The Thornel P-100 fiber is highly graphitic and should have a large narrow peak at approximately 1580 cm^{-1} and a smaller one at approximately 1360 cm^{-1} and possibly a small peak at 1620 cm^{-1} . The original fiber, F1, Raman plots produce the expected results as shown in Figure 5.9.

The other five fibers were also tested. A scan of fiber F2 is shown in Figure 5.10 and is representative of all of the remaining fibers. The Raman frequency shifts of the oxidized and detreated/oxidized fibers from the original fiber are not very substantial but the width and I_D/I_G ratios provide some insight as shown in Table 5.2. The ratio of I_D/I_G has been found to be a relation to the number of graphitic edges in the carbon structure. The intensity, I_D, is driven by broken edges or non-continuos crystals. Further, Wang stated that the D peak size was increased by breaks in the symmetry of the crystal structure [49]. Although, the frequency of the D peak is not affected by the cause of the symmetry change. This can be directly related to the Raman plots for the tested fibers. As stated in Section 5.1, the carbon bonds on the edges of the graphitic planes were broken and bonded with hydroxides or hydrogen-bridge oxide structures. This would create a large number of graphitic edges and break up the symmetry of the crystal structure. The width of the Raman shows that the frequency response of the structure is fairly wide; meaning disorder and a lot of variation.

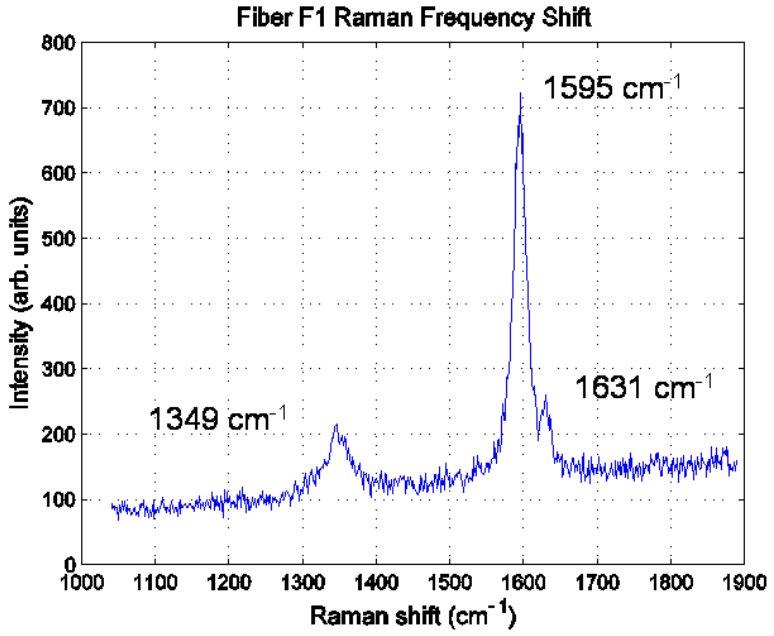

Figure 5.9: Raman results of fiber F1, frequency peaks can be seen at 1349, 1595, and 1631 cm^{-1}.

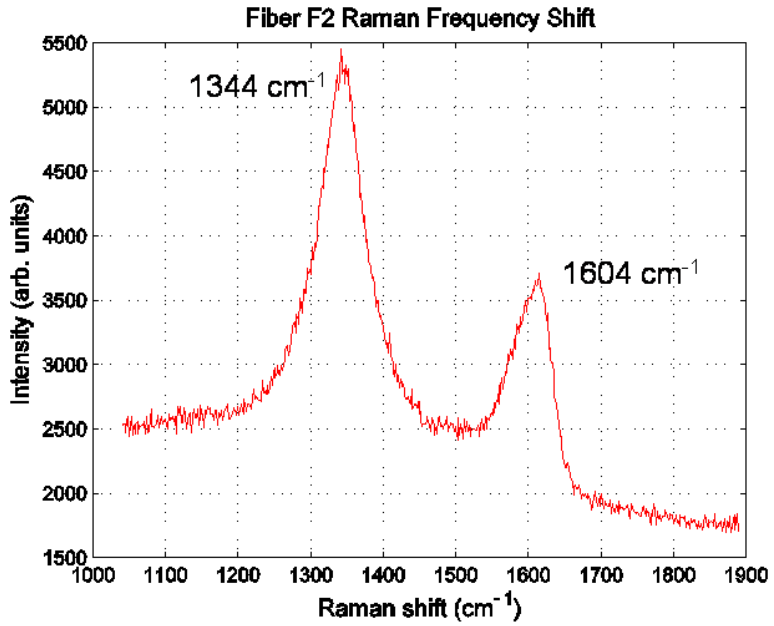

Figure 5.10: Raman results of fiber F2, frequency peaks can be seen at 1344, and 1603 cm^{-1}.

Table 5.2: Carbon fiber samples F1 through F6 Raman results

Property	Units	F1	F2	F3	F4	F5	F6
I_{1360}/I_{1580}	%	16.5	177.9	165.2	171.3	186.5	164.0
Peak position	cm^{-1}	1349	1344	1345	1343	1343.2	1345.6
Intensity	arb. units	92.3	3005.0	3829.0	4257.7	3715.33	4814.0
width	cm^{-1}	40.9	86.4	114.0	128.1	103.9	116.1
Peak position	cm^{-1}	1595	1603.4	1597.7	1596.2	1598.0	1596.0
Intensity	arb. units	559.3	1662.8	2313.5	2563.0	1992.8	2948.8
width	cm^{-1}	21.3	63.8	82.0	82.9	79.2	82.3
Peak position	cm^{-1}	1631	N/A	N/A	N/A	N/A	N/A
Intensity	arb. units	69.6	N/A	N/A	N/A	N/A	N/A
width	cm^{-1}	14.9	N/A	N/A	N/A	N/A	N/A

5.4 Resistance, Capacitance, and Inductance Analysis

Although unable to collect resistance, capacitance, and inductance data for the six types of fibers during intercalation, the computer routine created with the Vee® software was used to collect data on two samples of all fibers. The Agilent manual for the 4284A Precision LCR Meter proved to be a useful resource both during programming and data analysis. Prior to testing, the Agilent 4284A was left on for at least 24 hours and the correction routines for an open and short connection were run. The adapter used for fiber testing was the 16092A and allowed the testing of the sample up to 1 MHz. The 4284A has the capability of running in several modes including: impedance and phase, parallel and series capacitance and resistance, parallel and series inductance and resistance. All of this data was collected for these fibers but we will be concentrating on the impedance and phase since these are the basis on how the system was analyzed [51].

Impedance is normally referred to as Z and phase as θ. The values of impedance and phase allow the derivation of the circuits resistance (R), reactance (X), capacitance (C) and inductance (L) as given by

$$Z = |Z| \angle \theta \ \ (\Omega) \tag{5.1}$$

$$|Z| = \sqrt{R^2 + X^2} \ (\Omega) \tag{5.2}$$

$$\theta = arctan(|X|/R) \ (degrees) \tag{5.3}$$

$$X_C = 1/(2\pi fC) \ (\Omega) \tag{5.4}$$

$$X_L = 2\pi fL \ (\Omega) \tag{5.5}$$

where f is the frequency in Hz. The values X_C and X_L reference the reactance due to the capacitor or inductor and is determined by the sign of the phase (θ). When θ is (-), the capacitance is greater than the inductance. The inductance is greater than the capacitance when the θ is (+). The Agilent 4284A measures data for a black box. The components are unknown and it injects an input and measures the output. It then uses some internal mathematics to calculate the overall circuit response, not the internal component response. The impedance and phase are the basis for calculating the system components at each frequency starting with Equation (5.2), solve for the reactance, $|X|$, see Equation (5.6). The resistance, R, can then be calculated by substituting (5.6) into (5.3), resulting in (5.7). Then Equation (5.2) can be used to calculate the impedance. This leaves the capacitance and inductance which is a trivial matter to solve for but is included here for completeness

$$|X| = \sqrt{R^2 + Z^2} \ (\Omega) \tag{5.6}$$

$$R = Z/\sqrt{1 + tan\theta^2} \ (\Omega) \tag{5.7}$$

$$C = 1/(2X_C\pi f) \ (F) \tag{5.8}$$

$$L = X_L/(2\pi f) \ (H) \tag{5.9}$$

These equations do not tell the whole story: the internal capacitances and inductances interact and affects the phase of the circuit. When a resonant frequency

is applied, the phases from the inductance and capacitance cancel each other out and the phase becomes zero. At that point, the result is dependent on the make up of the circuit. If the circuit is a parallel RLC circuit, then the impedance will be at a maximum. Then the impedance for any frequency other the the resonant frequency will be lower. If the circuit in question is a series RLC circuit, then when the phase crosses zero the impedance will be at a minimum.

5.4.1 Impedance Testing Results of Tested Samples. As a preliminary test, a F1 fiber was placed on top of a glass slide and mounted directly onto the 16092A test fixture. The fiber was then tested with FIBER_FREQ_Measurement.vee program at the frequencies in Table A.2. The resistivity of the fiber is virtually identical to the impedance based on the measured phase and impedance. The resistivity is approximately 2.74 $\mu\Omega$-m. This is very comparable to Cytec's website which provides a typical value of 2.5 $\mu\Omega$-m [52]. The fiber has two points where the phase crosses zero, between 20-50 Hz and 150,000-200,000 Hz, see Figure 5.11. A parallel or series RLC circuit would result in either a maximum or a minimum resistance at this transition but this does not occur for this fiber, which could mean many things. A few of these include, first, the phase is so small that the capacitance and inductance play too small a role in the results for clear points to be observed. Second, and possibly more likely, the circuit is made up of a combination of serial and parallel circuits that cause the circuit to not behave in an easily identifiable manner.

The first fibers length was physically measured but the diameter was estimated to be 10 μm based on the Cytec website for the purpose of calculations [52]. The calculations for the remaining fibers were made based on dimensions determined from optical measurements, i.e. via the microscope. The dimensions of a known object pictured under the microscope using a lens objective that provided the best view of the fiber was used to define the length of each pixel. Then the associated fiber dimensions were calculated by counting the pixels in the given direction and multiplying by the pixel length. These results are shown in Table 5.3. The values

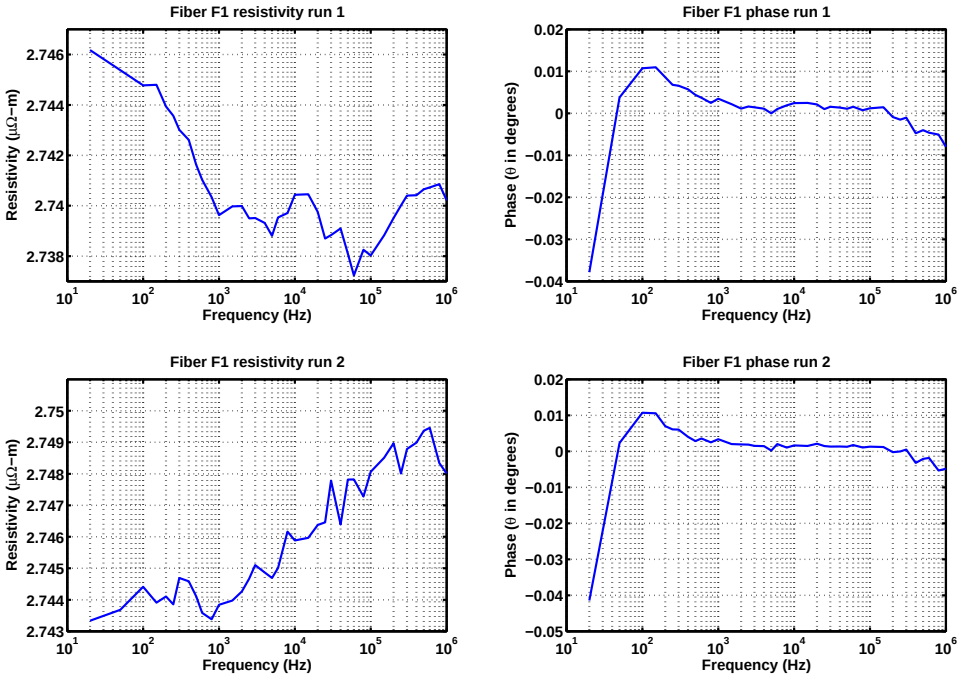

Figure 5.11: F1 fiber sample mounted directly onto 16092A with a cut glass slide separating it from contact with the fixture between probe points

were then used to calculate the resistivity based on the resistance from Equation (5.7). These calculations utilized

$$\rho = RA/L \ (\mu\Omega\cdot\mathrm{m}) \ [53] \tag{5.10}$$

where ρ is the resistivity , R is the resistance, A is the cross-sectional area and L is the fiber length. The area is simplified to $2\pi r^2$, the area of a circle with radius r. This calculation takes into account the fiber size and allows easy comparison between fibers.

The remainder of the testing involved mounting the tested fibers onto a glass slide where E-Beam evaporated gold had previously been applied with a thickness of 1500 to 2000 Å and a quarter inch distance between pads. The fiber was then secured into place with the Epo-Tek® H-27D silver epoxy, see Figure 5.12. Each

Table 5.3: Calculated carbon fiber sample dimensions

fiber type	sample number	length mm	diameter μm
F1	1	6.329	10.512
F1	2	6.306	10.034
F2	1	6.358	10.512
F2	2	6.406	10.99
F3	1	6.377	12.423
F3	2	6.229	10.99
F4	1	6.484	14.334
F4	2	6.261	11.945
F5	1	6.317	10.512
F5	2	6.439	10.512
F6	1	6.285	12.423
F6	2	6.285	13.857

fiber was tested twice. Once with the end of the fiber exposed and again with the epoxy covering the end of the fiber. After the first measurement, the fiber was carefully fractured after the point where it was originally bonded and the fiber ends were covered with `Epo-Tek`® H-27D epoxy. This was accomplished to identify any electrical change to the internal structure of the fibers from the chemical treatment. The data collected with the fiber ends uncovered is most comparable with the data in Figure 5.11. The data for Figure 5.11 was of a fiber with its ends exposed since it was clamped into the testing assembly. Several of the fibers, F3, F4, and F5, produced bad data when the fiber ends were uncovered due to a poor electrical connection and are not included. The rest of the data was collected and processed using `Matlab`® to calculate the resistivity of the tested fibers over the frequency range. This data was then placed into plots and is shown in Figures 5.13 to 5.21

5.4.2 Comparison of Impedance Testing Results. The results of these test produced a lot of variance. Referring to Figures 5.13 and 5.14, the two F1 samples had very similar impedance and phase results. When the fiber ends were covered the resistivity more then doubled with waves forming in the phase response. This is

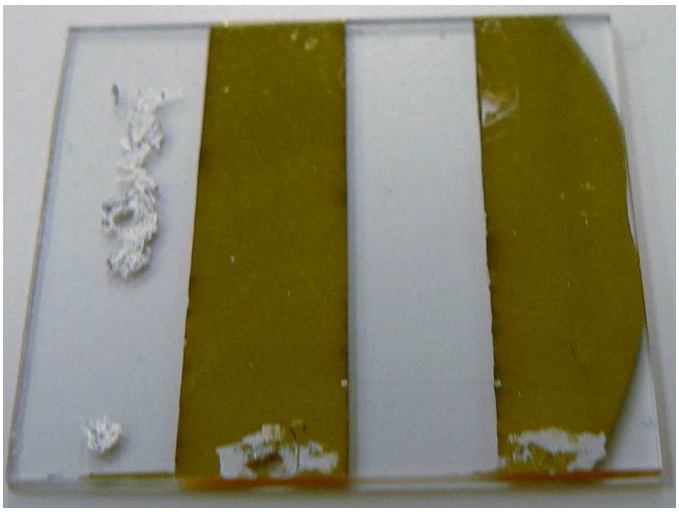

Figure 5.12: e-beam evaporated gold approximately 1500 Å thick and 0.25 inches apart with a carbon fiber mounted across the gap and secured with H-27D epoxy

probably caused by the graphite planes in the fiber and their inductive and capacitive interaction. The results are counter intuitive, it would be expected for the resistance to decrease based on parallel resistance of the graphene planes inside the carbon fiber. That would be true if the fiber was made up of contiguous graphene sheets like pure graphite but that is not the case. Breaks in the internal graphene sheets and the molecular bonds between the graphene layers would hinder electron movement.

Fiber F2 had similar results, independent of covering the fiber ends or not, see Figures 5.15 and 5.16. This could make fiber F2 a viable option for continued testing. The fiber would not necessarily have to be sealed on the ends, and if it was the resulting impedance, would be similar. The phases were only marginally different with a slight shift in the upper resonant frequency. The covered end results resistance is similar to the covered end results of F1, this could be due to the nitric acid treatment on the surface.

The only results for fiber F3 were for the graphite fiber's ends being covered and used for the circuit. The results for both fibers as seen in Figure 5.17 were similar to fiber F2. The phase was not very consistent until about 20 KHz, where the capacitance began to build, as noted by the decrease in phase.

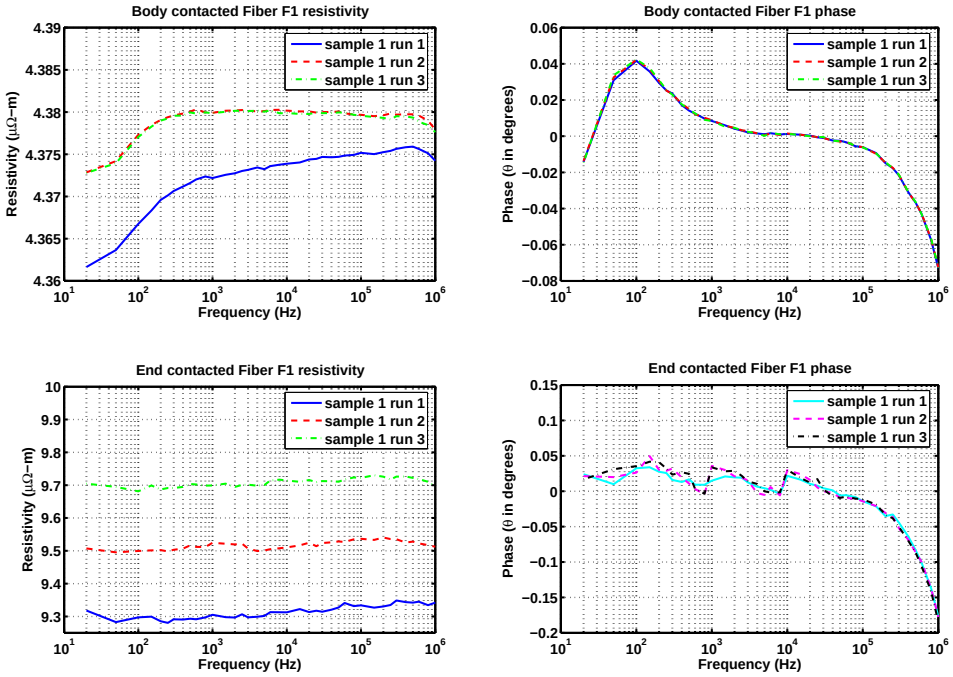

Figure 5.13: F1 sample 1 mounted onto a glass slide, resistivity and phase are provided for each frequency tested and all plots are created from a single fiber.

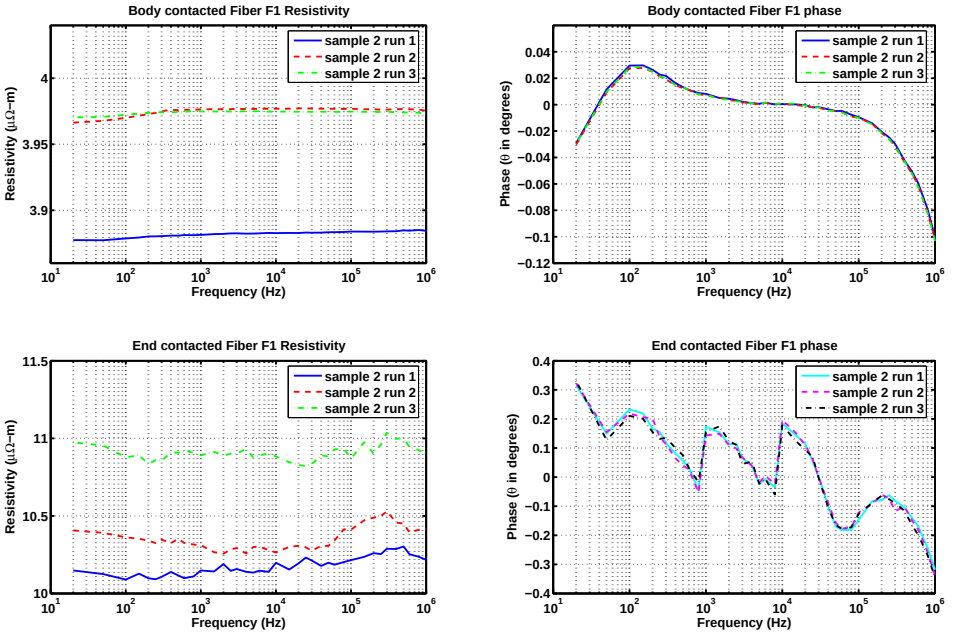

Figure 5.14: F1 sample 2 mounted onto a glass slide, resistivity and phase are provided for each frequency tested and all plots are created from a single fiber.

Fiber F4, from Figure 5.18, shows a dramatic increase in the fiber end covered resistance. This is probably due to the 2 minutes of oxidation in HNO_3. As seen in the SEM images of Section 5.2, the fibers surface was heavily damaged and from these measurements, the interior was also damaged due to the excessive resistivity of this fiber.

The results for fiber F5, with the ends covered, were not very consistent, reference Figure 5.19. One fiber had twice the resistance of the other with phases that were similar to all of the other fibers. This could mean that the heat and oxidation treatment did not have sufficient time to react to all of the fibers or one of the fibers was damaged in one fashion or another. The sample size and response divergence does not allow for any insight into why this has taken place.

Fiber F6 is the only fiber where the covered end fiber has a lower resistivity then the exposed end fiber. By referring to Figures 5.20 and 5.21 and Figures 5.13 and 5.14, the resistivity is still 3 to 4 times higher then the original F1 fiber. The F6 fiber has a stable phase between approximately 60 Hz and 20KHz.

Overall, what appears to be the most promising fibers from those tested are fibers F1, F2, and F3. Fiber F4 was to badly damaged from the treatment and fibers F5 and F6 had resistivities that were substantially higher then the other fibers. This will probably cause the intercalation reaction to slow down and reduce the effectiveness of the reaction.

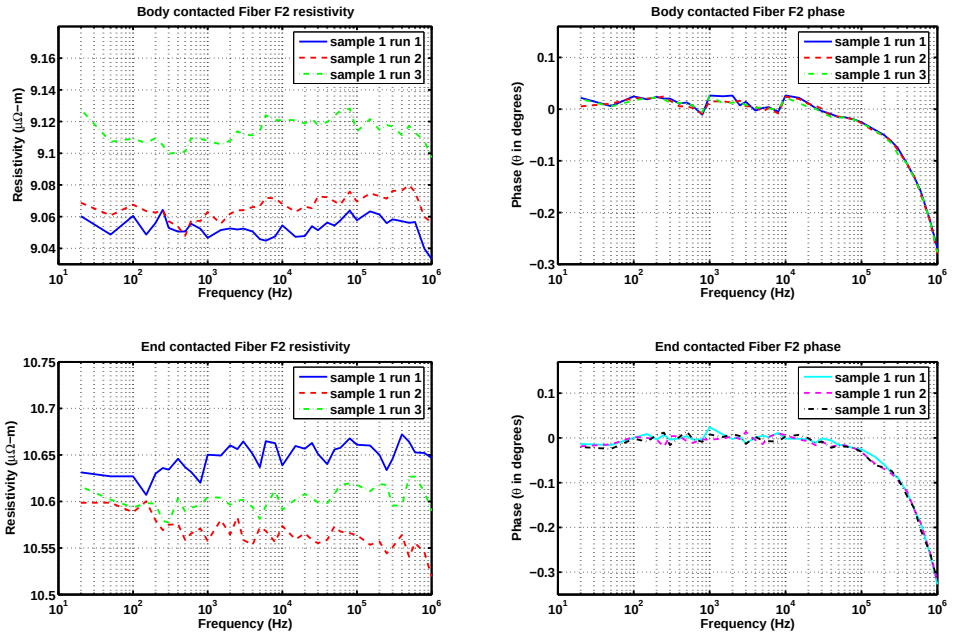

Figure 5.15: F2 sample 1 mounted onto a glass slide, resistivity and phase are provided for each frequency tested and all plots are created from a single fiber.

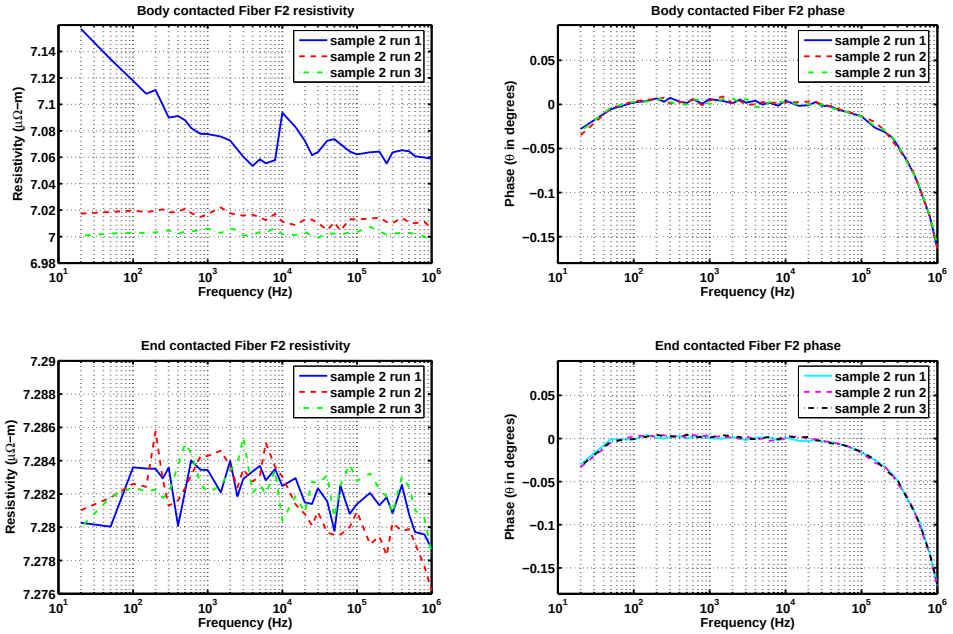

Figure 5.16: F2 sample 2 mounted onto a glass slide, resistivity and phase are provided for each frequency tested and all plots are created from a single fiber. The top two plots were from three runs where the fiber ends were exposed.

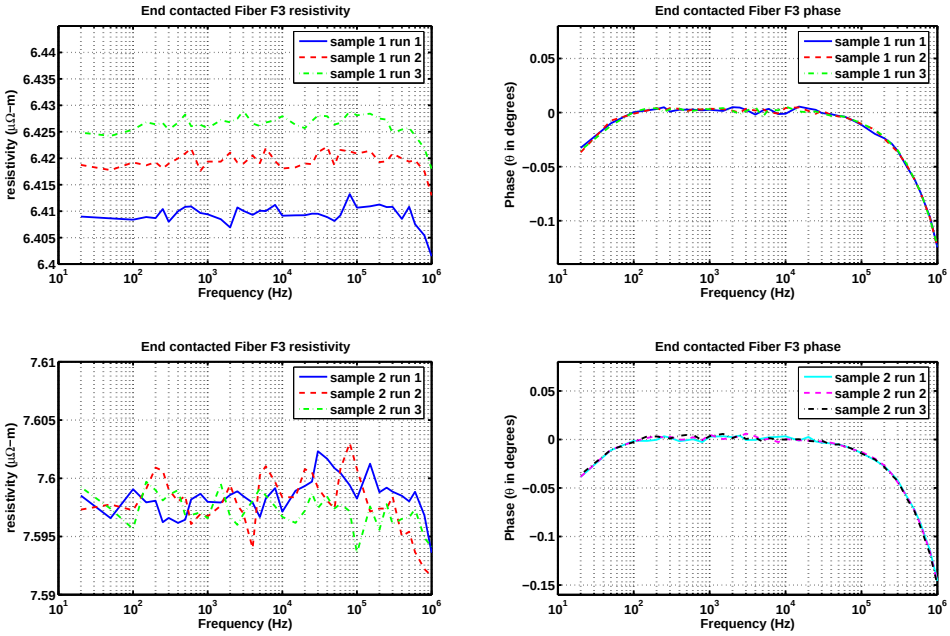

Figure 5.17: F3 samples 1 and 2, this data represents 2 fiber samples with the fiber ends covered with Epo-Tek® H-27D epoxy. The top two plots were from three runs for fiber F3 sample 1. The bottom two plots were from three runs for fiber F3 sample 2.

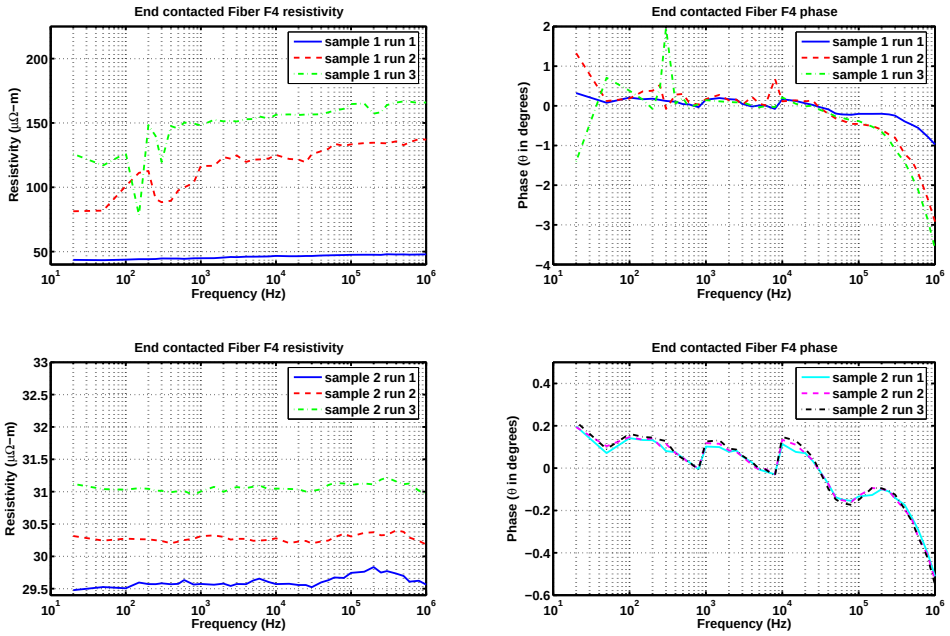

Figure 5.18: F4 samples 1 and 2, this data represents 2 fiber samples with the fiber ends covered with Epo-Tek® H-27D epoxy. The top two plots were from three runs for fiber F4 sample 1. The bottom two plots were from three runs for fiber F4 sample 2.

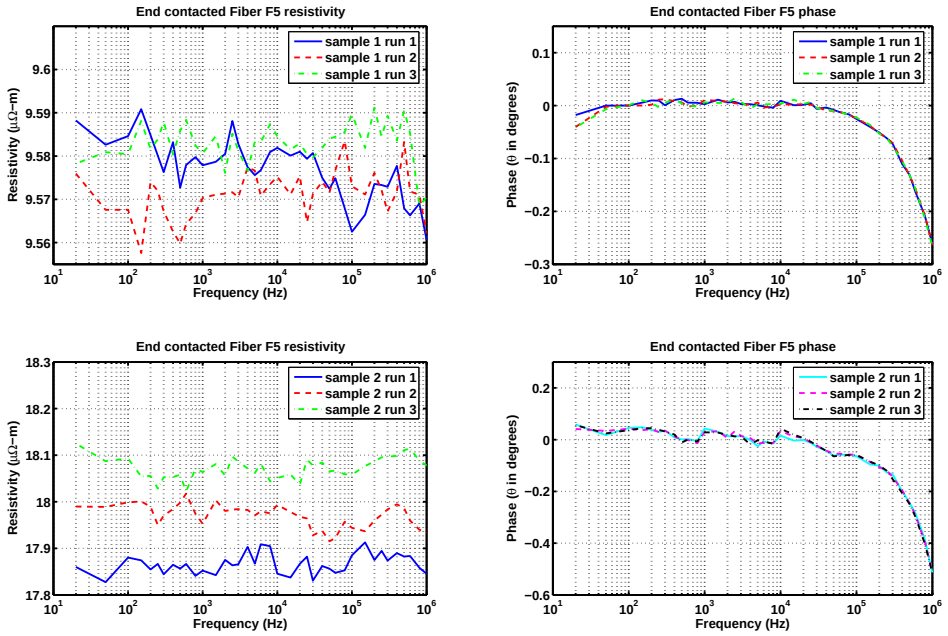

Figure 5.19: F5 samples 1 and 2, this data represents 2 fiber samples with the fiber ends covered with Epo-Tek® H-27D epoxy. The top two plots were from three runs for fiber F5 sample 1. The bottom two plots were from three runs for fiber F5 sample 2.

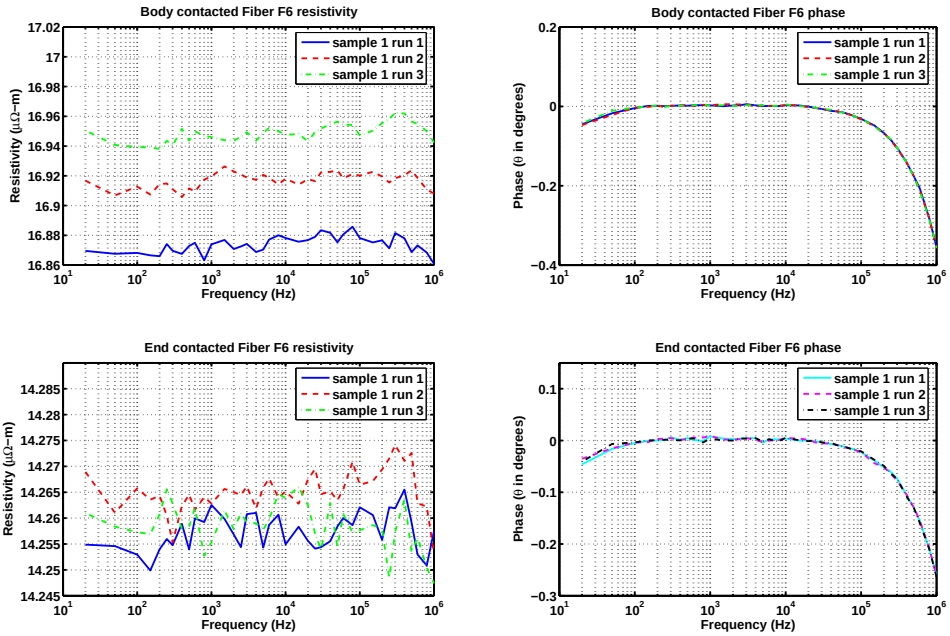

Figure 5.20: F6 sample 1 mounted onto a glass slide, resistivity and phase are provided for each frequency tested and all plots are created from a single fiber.

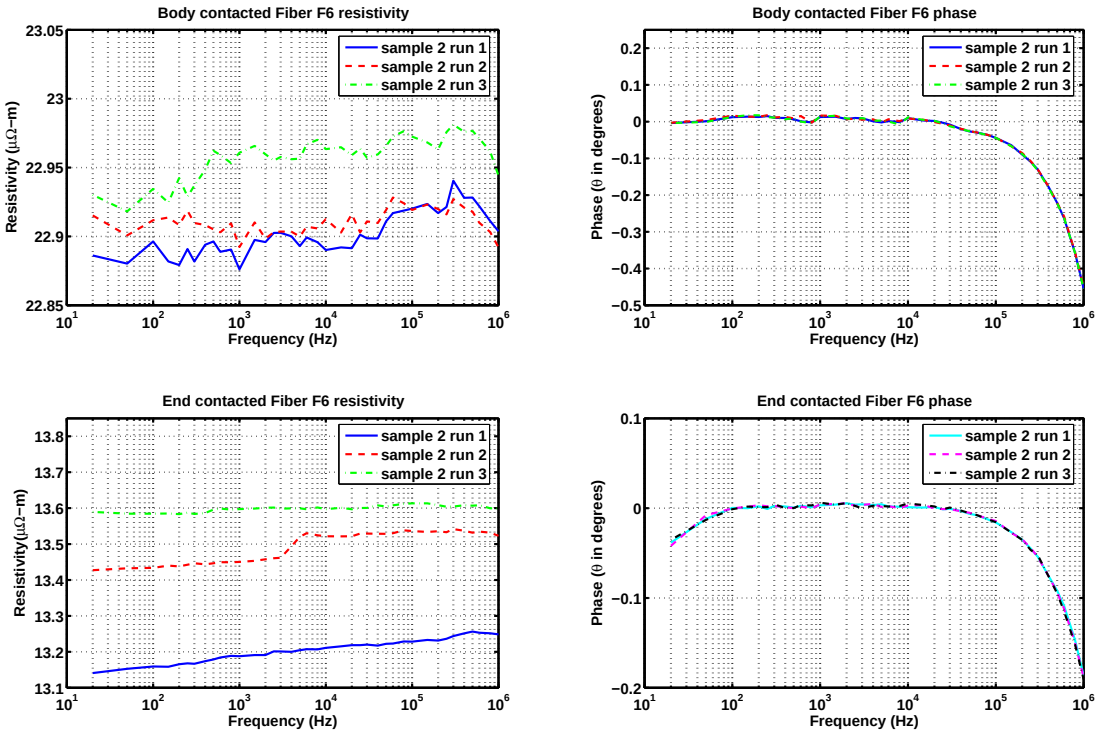

Figure 5.21: F6 sample 2 mounted onto a glass slide, resistivity and phase are provided for each frequency tested and all plots are created from a single fiber.

5.5 Strain and Force Analysis

Through the process of completing this research the intercalation of carbon fiber was achieved and some data was collected but related to the stress and strain that the fiber was able to produce and fit more in line with Kading's research. This research was to characterize the electrical and physical characteristics of the `Thornel`® P-100 carbon fiber when intercalated with 96 % H_2SO_4. As a side benefit, but not necessarily a requirement, actuation of MEMS structure was intended to be a portion of this research. Kading's disertation is investigating the PECT effect in intercalated graphite as a mechanism for actuation of MEMS. While working on two linked research projects, work was often done together to advance the techniques that were common between the two areas. During one of these periods a prime example of the PECT effect as discussed in Section 2.4.2 was observed.

5.5.1 Strain and Force Data from Tested Samples. During the testing of a fiber mounting process using a single layer of LOR-3A, SU8-5 photoresists and sputtered gold, the fiber was mounted onto a floating bond pad, with a distance between bond pads of 720 μm, and secured into the fiber channel with H-27D epoxy and 5000 Å of gold. A electrochemical cell similar to Figure 3.6 was created by placing the chip to be tested into a ceramic chip carrier, wire bonding the chip into place as shown in Figure 5.22 and bonding a gold wire within the carrier for use as a cathode. Sulfuric acid 96 % pure, was then added to the container and the lid was sealed with crystal bond. The chip carrier was then placed into a specially fabricated test fixture to ensure good electrical contact with the chip carrier pins demonstrated in Figure 5.23. A voltage was then applied using an Agilent E3631A DC power supply and current monitored by a 34401A DMM.

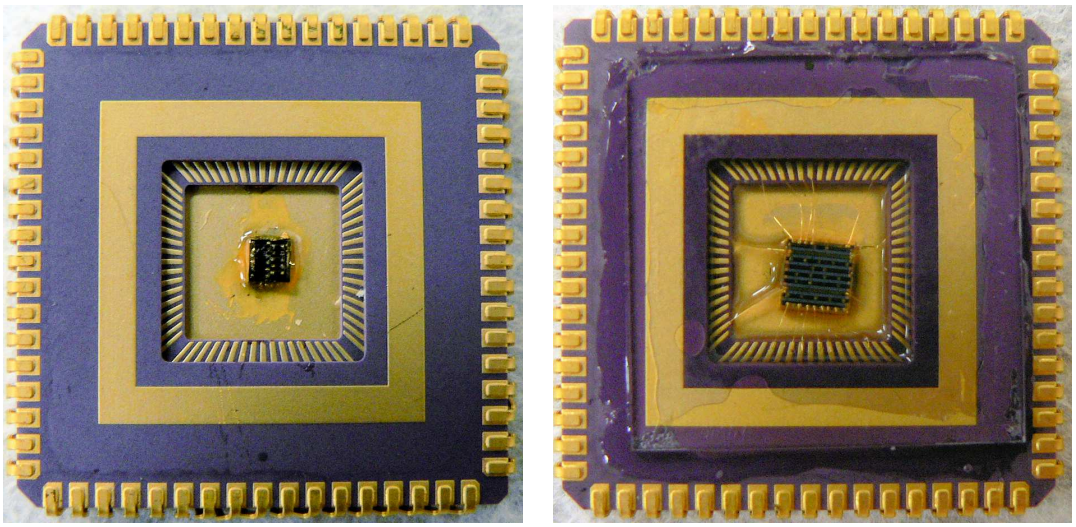

(a) (b)

Figure 5.22: Die mounted into a chip carrier. (a) shows a chip die secured in a chip carrier, (b) chip die prepared and ready for testing. The chip is secured into chip carrier, wire bonded, with acid inserted into the chamber, and a glass lid has been attached with crystal bond 509.

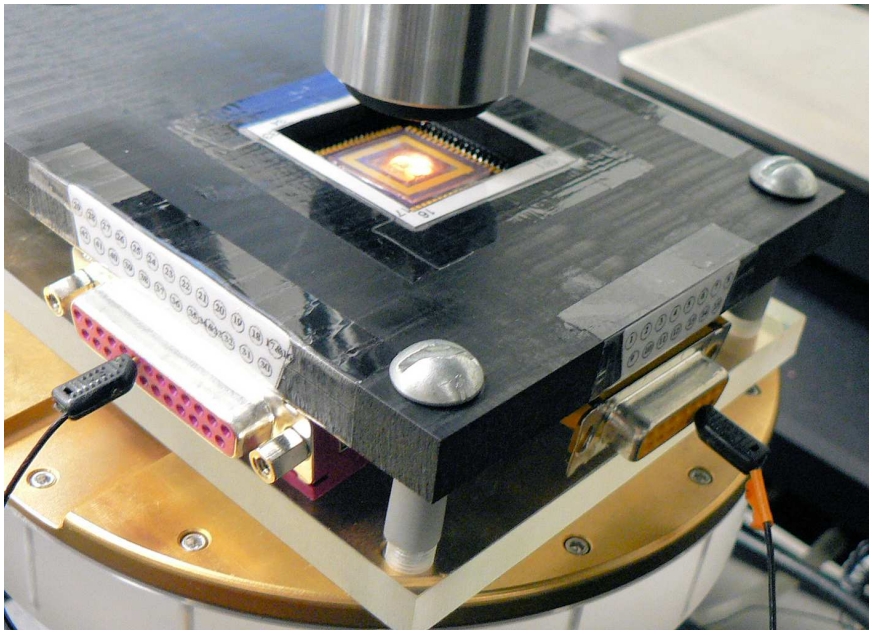

Figure 5.23: Test fixture with chip carrier used for intercalation testing of MEMS structures on micromanipulator probe station, test leads were used for the application of power to the assembly

The voltage was applied, starting at 0.0 volts and was stepped up to 1.4 V in 0.1 V increments. Through this process the floating bond pad was observed to move 1.5 μm from the force generated by a carbon fiber with a peak applied voltage of 1.4 V. The fiber achieved a total strain of 0.21 %. Using `Coventorware`® to process the results, the tested fiber produced a force of 1.712 mN and an internal stress of 21.79 MPa. During this same testing period we also tested an unsecured fiber, i.e. one attached to an anchor bond pad but not attached to a floating bond pad. This fiber deflected 5.3 μm achieving 0.74 % strain with 1.4 V applied [54].

5.6 Chapter summary

In this chapter the results of testing on six types of surface treated fibers was presented and evaluated. The fibers were inspected with a scanning electron microscope (SEM) and the most damaged fiber appeared to be fiber F4, that was anodically oxidized for two minutes without any additional heat treatment. The

fibers were also probed with the Raman microscope. These results showed that the oxidized fibers had a very high intensity D peak, ≈1345 cm^{-1}, with a wide 3 dB point. The highest I_D/I_G in the Raman data was fiber F5. This ratio correlates to the number of graphitic edges in the graphite. In this case, the edges would be accounted for by the number of hydroxide or hydrogen-bridge oxide structures created during the anodic oxidation. The third test was the impedance measurements. The fibers were tested with an Agilent 4284A Precision LCR meter. All of the fibers including the untreated fibers had similar phase plots. The resistivity varied from sample to sample, but the resistance peaked in fiber F4. The last test discussed, was the intercalation of an F0 carbon fiber resulting in the movement of a MEMS actuator.

VI. Conclusions and Recommendations

6.1 Thesis Summary

The Air Force and industry are always seeking out new types of MEMS actuators, with low power requirements and weight. Carbon fibers or related materials could be used for this task. This research was the first step, with the goal of characterizing the electrical and physical characteristic changes of intercalated carbon fibers and incorporating the use of MEMS structures for testing purposes.

MEMS were used for this purpose because they allowed the testing of carbon fibers in an isolated micro-scale environment with mathematically proven physical models that simplified the mathematics to characterize the carbon fibers. MEMS structures were created using the PolyMUMPs process in which individual carbon fibers could be mounted and tested. Two types of structures were designed, four point probes and bond pads with floating bond pads. The four point probe was made to measure the electrical characteristics of fibers in pristine and intercalated condition. The bond pad and floating bond pad system was created to examine the physical and electrical characteristics of a fiber when intercalated, while being biased by a small signal voltage. Throughout this research, these designs have been modified and improved to make testing more efficient and the results more accurate.

During the production of this thesis, a fiber was intercalated with 96 % H_2SO_4 and the change in fiber dimensions was measured and the force was calculated. This test was not repeatable. The majority of the work for this thesis involved the identification of a repeatable and consistent method for mounting the carbon fibers that would not deteriorate when exposed to 96 % H_2SO_4. The standard photolithographic practices were applied using photoresist and often left residue in place or fractured the fiber during its removal. Alternative approaches were tried with limited success. Paraffin was applied to the fiber ends over the epoxy but when heated in a liquid would melt and peel off. Solder powder was placed on the bond pads, and although the correct dimensions, melted at to high of a temperature and would damage the bond pad and eventually not adhere. Electroplating was also tried with little suc-

cess. A lot of the issue comes down to cost. Gold may bond the fiber down fine if applied thick enough, the dip created in the bond pad reduces the height of the exposed carbon fiber in half, to 5 μm. To cover this with gold another 5 μm may be necessary but is cost prohibitive.

The remainder of the research was accomplished on the six versions of the `Thornel`® P-100 carbon fiber that we had for testing. These fibers were studied with a SEM to note any physically observable changes from the surface treatment that they received from the anodic oxidation in nitric acid and the detreating heat treatment. Raman spectroscopy was also completed on the fibers to look into the structure of the fibers and they were found to be more disorganized after the treatment with a high I_D/I_G which translates into a large number of non-continuous crystal structures or broken edges. The fibers were then tested electrically with small signals to compare their responses to stimuli. The resistivity of each fiber was calculated and the treated fibers consistently had greater resistivities then the original fiber although all of the fibers had similar phase response.

Once the PolyMUMPs wafers returned from MEMSCAP the carbon fibers were to be secured onto the test devices with conductive silver epoxy and permanently mounted with metal. The wafer was then to be placed in a chip carrier and wire bonded to the external pins to improve testing efficiency. The intercalant material would be inserted into the chip carrier then the chip carrier is sealed making the fibers ready for testing and data collection. This would have led to the use of both `Coventorware`® for mechanical modeling and other computer software programs to determine the mechanical force and impedance models for the `Thornel`® P-100 carbon fibers intercalated with H_2SO_4.

6.2 Recommendations for Continued Work

Continued testing of the six fiber types would be beneficial. The impedance data collected for the six types of fibers shows a zero phase crossing around the 50 to 100 Hz and 15 KHz to 20 KHz ranges. One way to try and isolate or improve

the granularity of the data would be to decrease the distance between the data points around these phase crossings. Possibly, making the calculations for the fiber capacitance and inductance per unit length of the fiber more clear. The number of fiber samples tested for impedance was limited in number since this was not the primary goal of this research. For truly meaningful data, the numbers should be expanded in another thesis. Expanded testing of these six fibers should include X-ray photoelectron spectroscopy to provide further insight into the fiber structure and identify the oxygen and hydrogen bonds that were formed within each of the different fibers. When compared with intercalation tests these results would help discern which fiber treatment would produce the best results for the desired purpose, i.e apply the most force or have the widest variance in resistivity.

The deterioration of the mounting for carbon fibers when exposed to intercalation voltages in sulfuric acid has been a key issue in this research. Other methods of mounting need to be identified and tested. One possible technique is to use a focused ion beam (FIB) to accomplish this. The FIB operates similarly to an SEM except that instead of a beam of electrons it uses an ion beam formed of Ga^+ ions. At low power, this beam can be used to take images like an SEM, but when used at high power can be used to cut or mill materials. With the addition of a gas stream over the sample, a material can be deposited on a surface by focusing the ion beam on the desired location [55]. Platinum deposition is achieved this way. It is recommended that the deposition of platinum on the bond pads over the fibers be accomplished. Resources to perform this task are available in the materials section of AFRL. Further research into other forms of photolithography materials might result in the discovery of a PR or other material that is used by other organizations for their lithography. A positive photoresist might be an excellent choice. As discovered in Section 4.4.1.4, the negative PR becomes trapped underneath the fiber during the developing process and is not removed, increasing the difficulty of bonding the fiber to the bond pad. The biggest concern is the creation of an electrical contact that can take the stress that the carbon fiber will apply.

This research was to be the beginning steps of research into the use of carbon intercalation in the *a*-plane as an actuating material. Use of the *a*-plane will allow the potential use of the graphite structure as a conductor. Possible alternative carbon structures would include highly oriented pyrolitic graphite or thin film graphite. These two materials have very well organized graphene planes and would intercalate well; although, their conductivity may not be as high as carbon fibers.

6.3 Chapter Summary

This chapter included a brief summation of the research accomplished for this thesis. Numerous mounting techniques were accomplished to ensure that the carbon fibers were held in place during intercalation testing in 96 % pure sulfuric acid. Each technique had varying amounts of succes and lessons learned from each technique were carried forward to the next approach. A fiber was intercalated and movement was observed, demonstrating that the use of strain induced in intercalated graphite in the *c*-plane is plausible. Six variations of the `Thornel`® P-100 fiber were tested by observation in an SEM, probing with a Raman spectroscope and finally electrically tested with AC small signals to identify the resistivity of each fiber type.

The recommendations for future work involved expanded testing of the six fiber types on their own. This could then be expanded into the intercalation of these fibers once a repeatable and consistent mounting technique has been developed. This could involve the use of the FIB or even standard lithography. The thickness of the gold or bonding material is an issue as the cost of applying several microns of gold is exorbitantly high and limits its usefulness to bond the fibers. The FIB offers the ability to bond the fiber using minimal material resources. Changing the base material from fibers to film graphite could result in a planar intercalant that is relatively easy to mount and then micromachine in place to the desired shape.

Appendix A. Experimental Setup Details and Operating Procedures

A.1 Setup

Set up for various tests that were accomplished.

A.1.1 Raman Microscope Settings. Table A.1 contains the setup information used for the Raman Spectroscopy.

Table A.1: Renishaw "InVia Raman Microscope" testing setup details [56]

Feature	Setting
Scan type	10 second static
scan dimensions	1040 Hz - 1890 Hz
Laser type	HeNe
laser wavelength	632.8 nm
Objective	50X LWD
Working distance	10.6 mm
Spot size	0.77 nm
Laser power on sample	0.11
Grating	1200 lines/mm
Wavenumber resolution	≈2-3 $(cm)^{-1}$

LWD - long working distance

A.1.2 Fiber Impedance Test Setup. Figures A.1 and A.2 show the proper mounting of the glass slides used for the impedance test

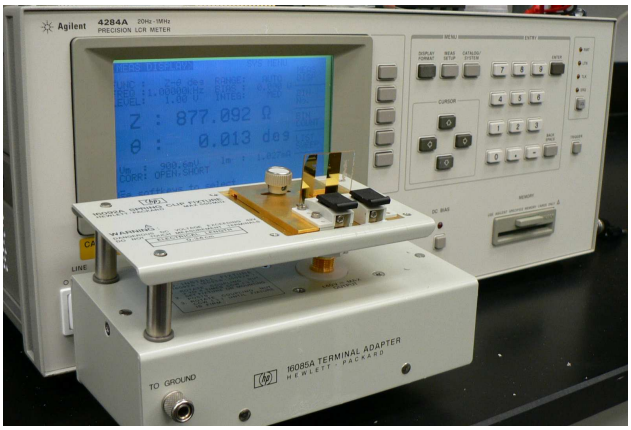

Figure A.1: Setup of e-Beam evaporated gold slide with fiber attached for testing fiber impedance. Note, gold is facing the screen of the Agilent 4284A to make electrical contact

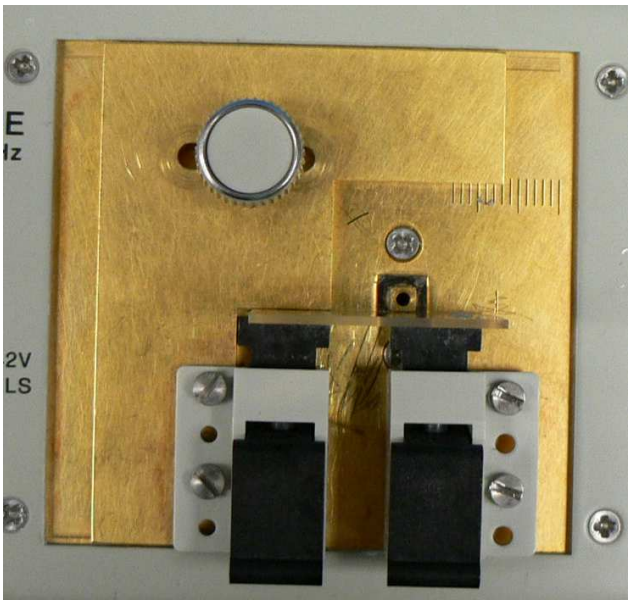

Figure A.2: Image of 16092A testing adapter with e-Beam evaporated gold slide with fiber attached. The gold on the glass slide faces the top of the picture when mounted correctly.

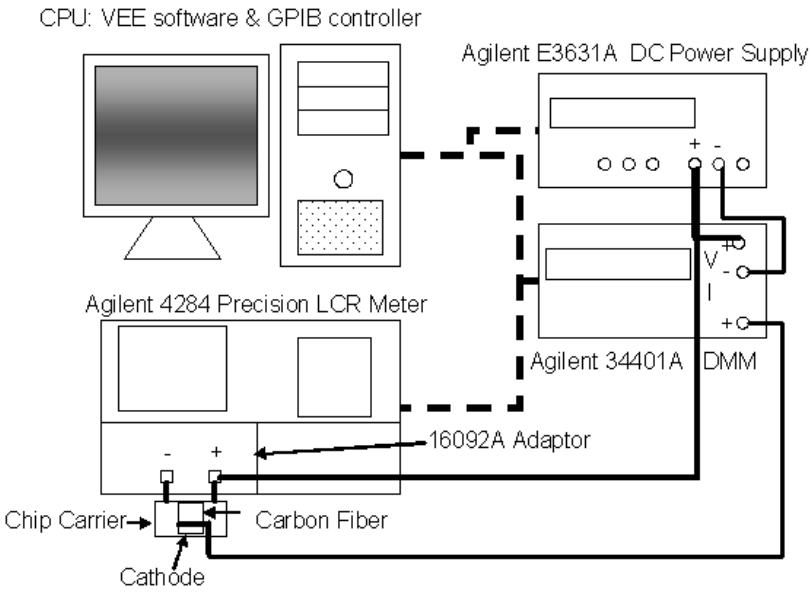

Figure A.3: Small signal frequency response test setup to measure inductance, capacitance and resistance.

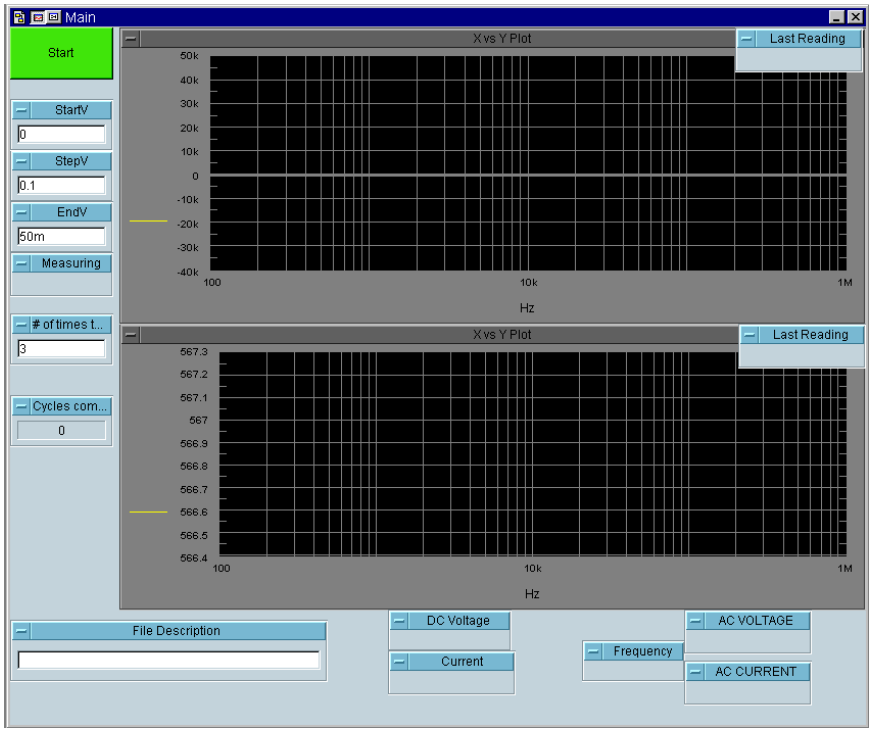

Figure A.4: Small signal frequency response test setup to measure inductance, capacitance and resistance.

Table A.2: Frequencies tested using FIBER_FREQ_Measurement.vee

Frequency	
20 Hz	10 kHz
50 Hz	20 kHz
100 Hz	25 kHz
150 Hz	30 kHz
200 Hz	40 kHz
250 Hz	50 kHz
300 Hz	60 kHz
400 Hz	80 kHz
500 Hz	100 kHz
600 Hz	150 kHz
800 Hz	200 kHz
1 kHz	250 kHz
1.5 kHz	300 kHz
2 kHz	400 kHz
2.5 kHz	500 kHz
3 kHz	600 kHz
4 kHz	800 kHz
5 kHz	1 MHz
6 kHz	
8 kHz	

A.2 Operation

Table A.3: Operating procedures to perform small signal response testing during intercalation of carbon fibers using FIBER_FREQ_Measurement.vee

step	Procedure
1	Turn on Agilent 4284 Precision LCR Meter 30 minutes prior to use
2	Connect IEEE-488 cables to system as shown in Figure A.3 as a dashed line
3	Adjust position of 16092A adapter spring clips to hold sample
4	Perform OPEN, and SHORT correction procedures in the 4284 manual [51] note: OPEN and SHORT correction procedures need to be reaccomplished if the position of spring clips are changed
5	Connect sample to 4284 and complete electrical connections as shown in Figure A.3
6	Start Fiber_Freq_Measurement.vee
7	Enter the following components Intercalation starting voltage (StartV) Intercalation step voltage (StepV) Intercalation ending voltage (EndV) Number of times to run, usually 1 File description, becomes suggested file name (EndV)
8	Press Start
9	Confirm or change file name cycles completed will update after it completes a run
10	When complete replace sample and proceed from step 7

A.3 FIBER_FREQ_Measurement.vee data collected

The data collected by the FIBER_FREQ_Measurement.vee program collects ten pieces of information per frequency pass. "Cycles" identifies the number of times the program has run and counts from 0 to the number of cycles chosen prior to running the program. The measurement mode descriptor, "MSRMT," is next and can be ZTD, CSRS, CPRP, LSRS, and LPRP which stand for impedance and phase, series capacitance and resistance, parallel capacitance and resistance, series inductance and resistance, and parallel inductance and resistance, respectively. The next two pieces of data relate to the intercalation voltage and current "DCVOL" and is the programmed intercalation voltage and "DC CURRENT" is the intercalation current as measured by the digital multimeter. "FREQUENCY" is the small signal frequency at which this data was collected. While "VAC" and "IAC" are the small signal voltage and current applied by the 4284 LCR meter for this frequency. "VARIABLE 1" and "VARIABLE 2" have different meanings depending on the measurement mode and are broken down in Table A.4. A sample table of collected data is located in table A.5.

Table A.4: Variable description for data collected using FIBER_FREQ_Measurement.vee

MSRMT	VARIABLE 1	VARIABLE 2
ZTD	Impedance (Ω)	Phase (°)
CSRS	series capacitance (F)	series resistance (Ω)
LSRS	series inductance (H)	series resistance (Ω)
CPRP	parallel capacitance (F)	parallel resistance (Ω)
LPRP	parallel inductance (H)	parallel resistance (Ω)

Table A.5: Data collected when running FIBER_FREQ_Measurement.vee program

Cycles	MSRMT	DCVOL	DC CURRENT	FREQUENCY	VAC	IAC	VARIABLE 1	VARIABLE 2
0	ZTD	0	9.89E-009	20	0.887812	0.00113944	778.868	-0.013545
0	ZTD	0	-9.89E-009	50	0.886114	0.00113815	778.551	-0.015908
0	ZTD	0	9.89E-009	100	0.88959	0.00114166	778.551	0.00031674
0	ZTD	0	-3.21E-008	150	0.889653	0.0011427	777.087	0.008698
0	ZTD	0	2.96E-008	200	0.88653	0.00113995	778.769	-0.003377
0	ZTD	0	4.9E-009	250	0.887514	0.00113983	779.206	0.006675
0	ZTD	0	-3.45E-008	300	0.89013	0.00114276	779.074	-0.003901
0	ZTD	0	-1.48E-008	400	0.889037	0.0011412	779.939	-0.001191
0	ZTD	0	7.4E-009	500	0.887415	0.00113833	779.269	0.003917

B.1 PolyMUMPS Run Design

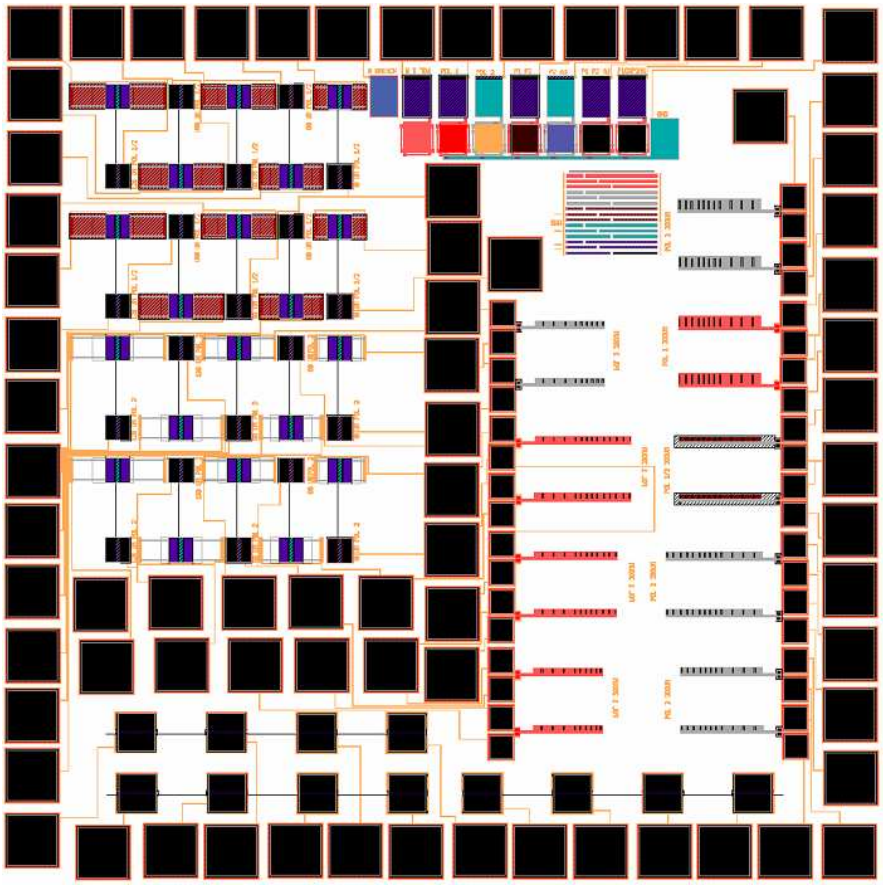

Figure B.1: PolyMUMPs Run 71 with cantilevers, thermal actuators, micromirrors, initial four point probe design and anchor and pulley system

• Poly1/Poly2 and Poly2 pulley and anchors with arm lengths from 40 to 100 μm and distance between bond pads of 200 μm. Floating bondpads had weak anchors and would tear from substrate.

• Wires routed with Poly0, were of different lengths and highly resistive, compromising the usefulness of these designs.

• Fiber anchor bond pad contacts were shorted to the substrate.

• Several wire bond pads around exterior of die had open resistance to wire runs, due to Poly1/Poly2 via being outside PolyMUMPs tolerance.

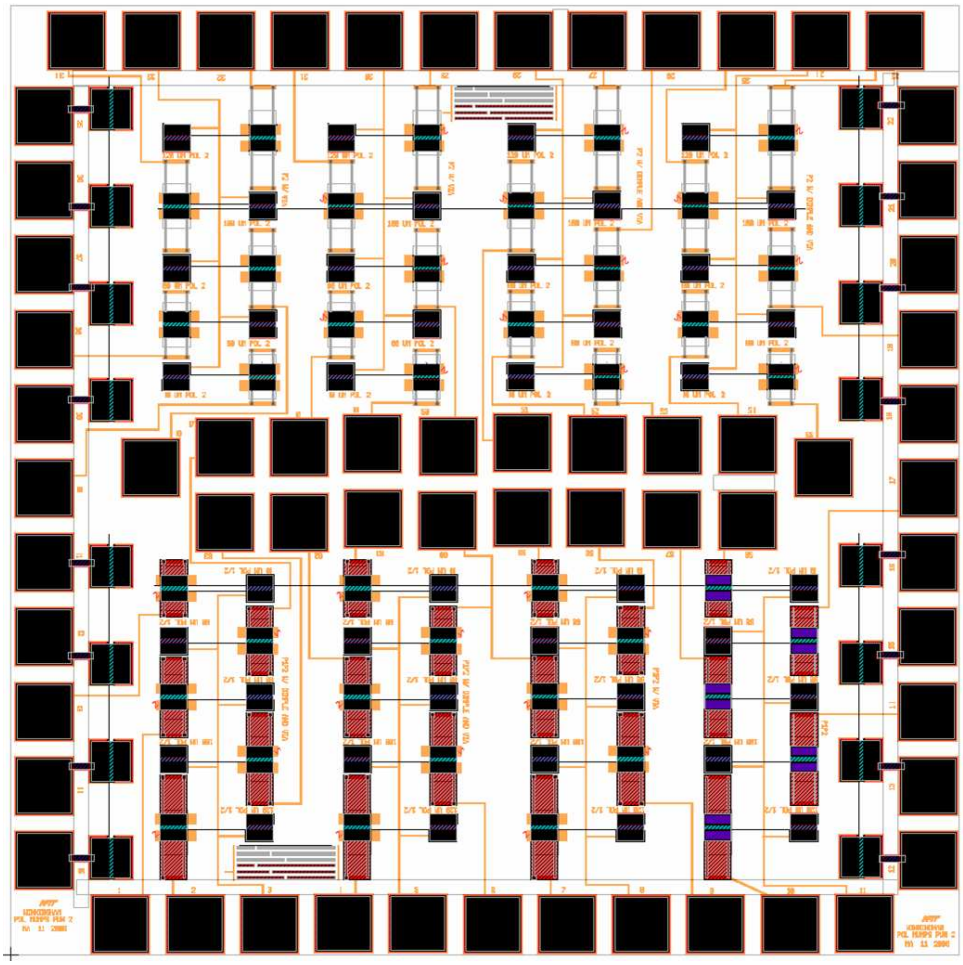

Figure B.2: PolyMUMPs Run 72: has bond pads and floating bond pads, four point probes, and Poly 1 and Poly1/Poly2 cantilevers

- Designs similar to PolyMUMPs run 71.
- Fixed fiber mounts are shorted to substrate.
- Floating bondpads had weak anchors and would tear from substrate.

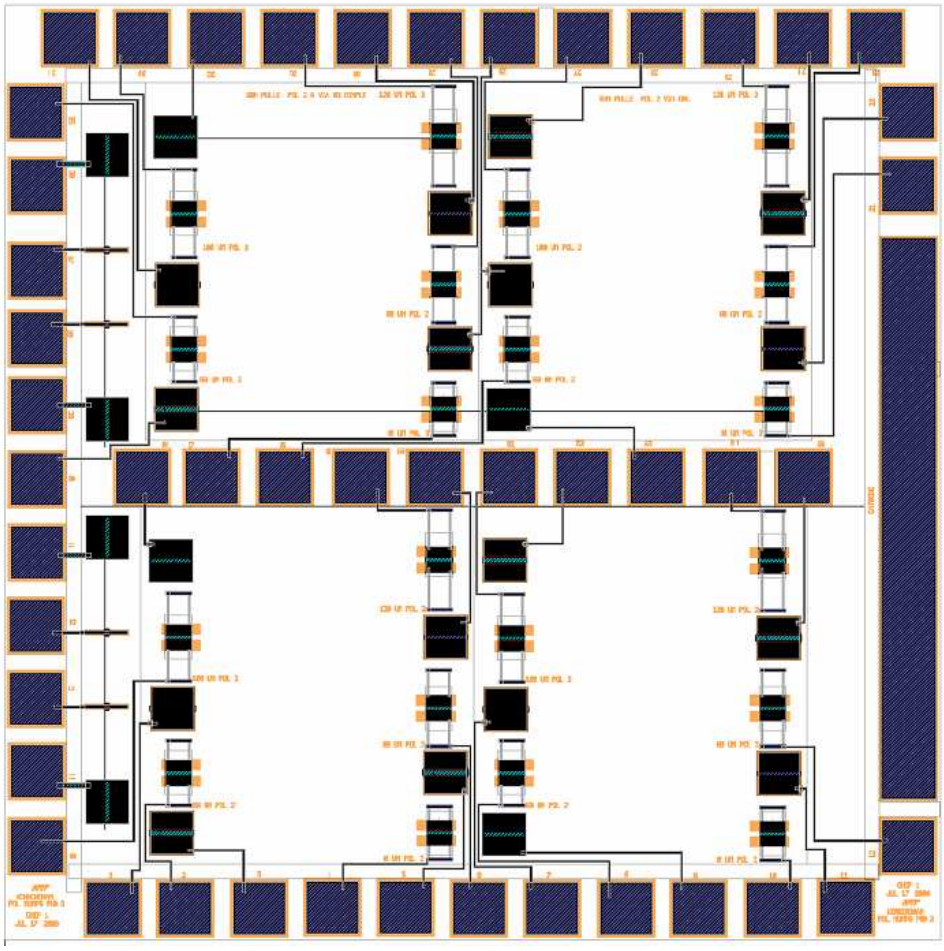

Figure B.3: PolyMUMPs Run 73A: wire runs created with Au over Poly2 to improve conductivity, Poly2 pulley systems, four point probes, and integrated Au cathode

• Poly2 pulley system with Au on anchor for improved conduction, anchors enlarged to strengthen structure.

• Four point probe narrowed to help with accuracy of measurements.

• 3 types of reworked fiber anchor bond pads to improve connection

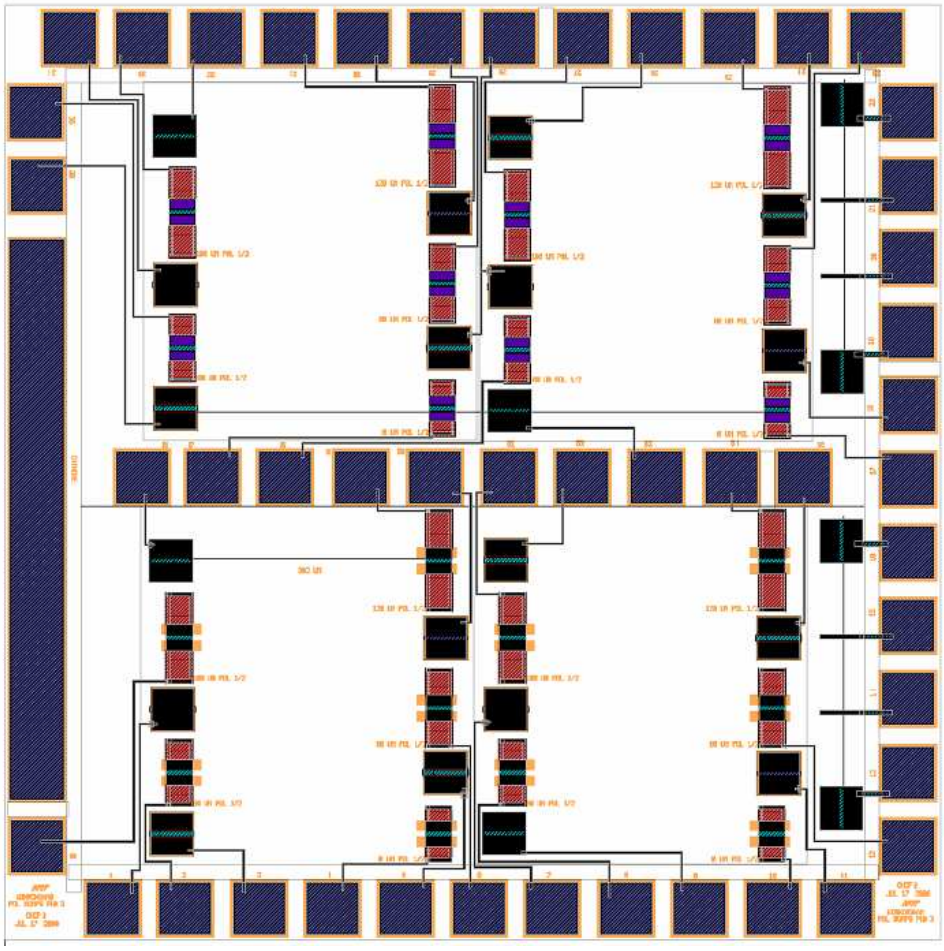

Figure B.4: PolyMUMPs Run 73B: wire runs created with Au over Poly2 to improve conductivity, Poly1/Poly2 pulley systems, four point probes, and integrated Au cathode

• Similar to Run 73A with Poly1 pulley system replaced with Poly1/Poly2 pulley devices

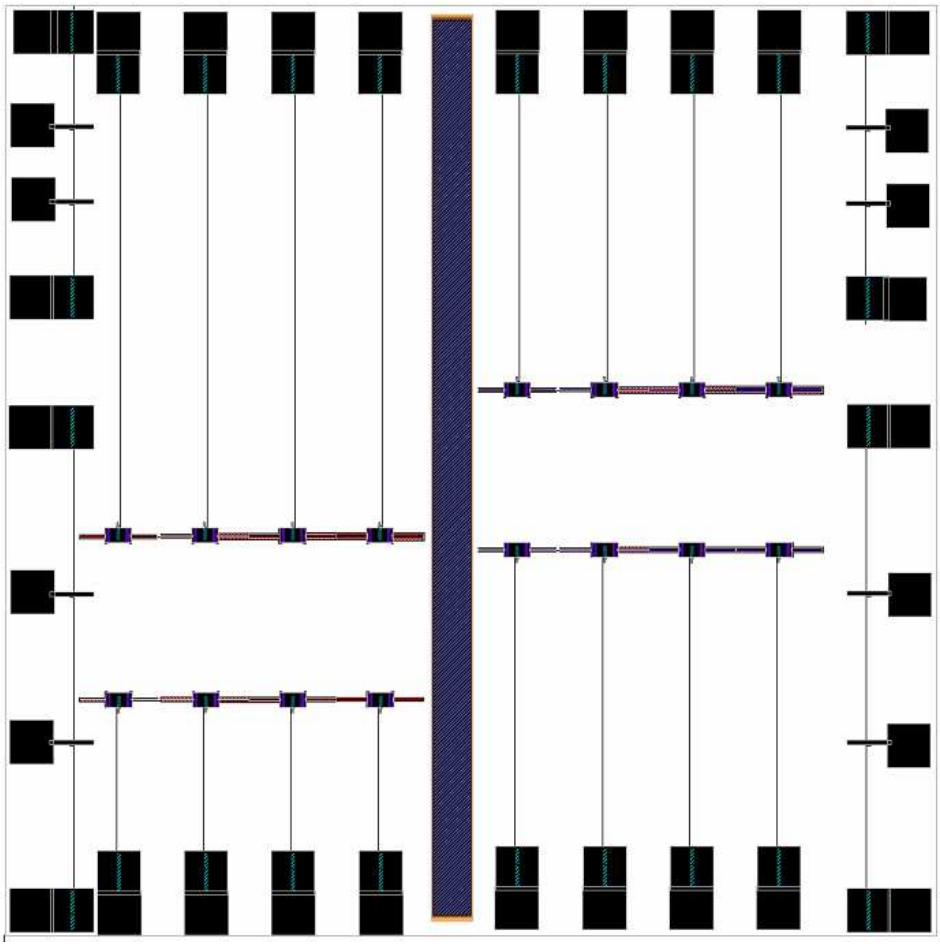

Figure B.5: PolyMUMPs Run 74A: Redesigned Poly1/Poly2 pulley systems with single arms, and four point probes of different lengths

• Floating bond pads were narrowed and anchor2 was placed underneath to make it easier for the structures to be released when placed in HF

• Created conjoined bond pads to eliminate wire runs from increasing resistance.

• Integrated cathode into center of die so that cathode is closer to all mounted fibers.

• Long fibers are sometimes difficult to mount so 2-four point probes of different lengths were created.

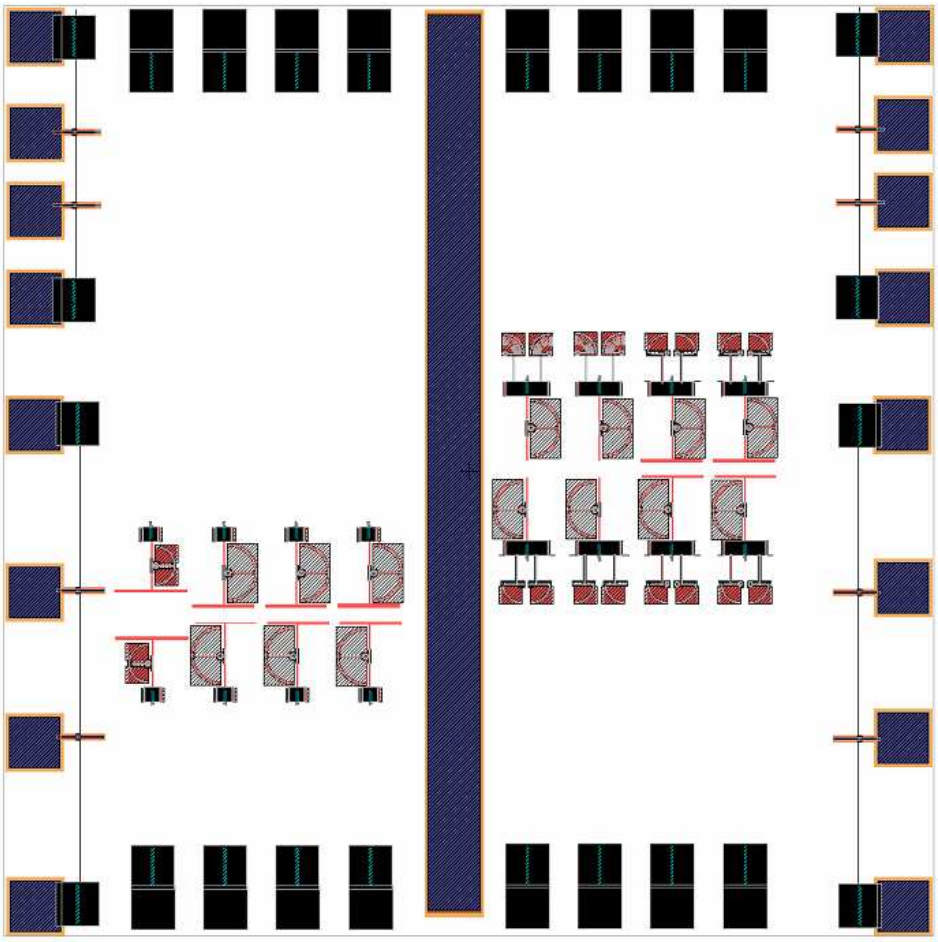

Figure B.6: PolyMUMPs Run 74b: Redesigned Poly1/Poly2 pulley systems with single arms, and four point probes of different lengths

• Cathode and Four point probes similar to run74A.

• Pulley structures created with different types of deflection multipliers to enhance observation of movement. These designs were made with tolerance that were to close to the PolyMUMPs design rules causing many of the independent structures to be combined.

• Used an anchored lip to cover the edges of floating bond pads, caused binding and did not slide smoothly.

B.2 PolyMUMPS Run Images (SEM, ZYGO, and/or Microscope)

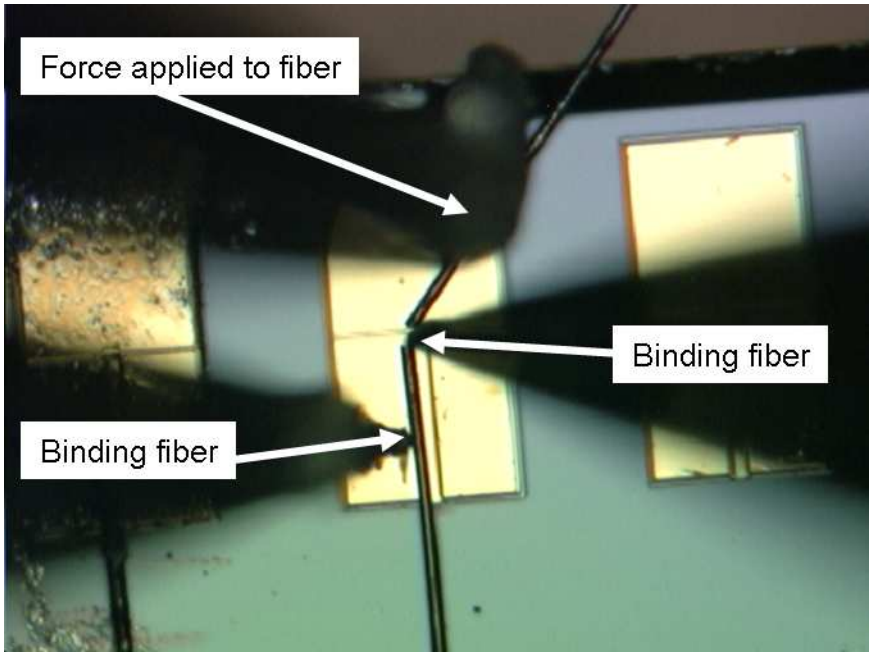

Figure B.7: Method to shorten fibers when to long. First the fiber needs to be in the desired position and loosely bonded to the substrate, in this case, wet H-27D epoxy is holding the fiber in place. Three probes are required: one to the right of the fiber at the point where the break is desired, a second probe on the lower left to stabilize the fiber and a final probe at the top to push against the fiber and break it.

Bibliography

1. A. P. Legrand, S. Flandrois, and North Atlantic Treaty Organization. Scientific Affairs Division, *Chemical physics of intercalation*, vol. 172, Plenum, New York, 1987.

2. F. Lincoln Vogel, "Electrical conductivity of graphite intercalated with superacid flourides: experiments with antimony pentaflouride", *Journal of Materials Science*, vol. 12, pp. 982–986, 1977.

3. D. D. L. Chung, "Review: Graphite", *Journal of Materials Science*, vol. 37, no. 8, pp. 1475–1489, 2002.

4. S Luski, H Selig, I Ohana, C Rettori, and D Davidov, "Study of the mechanism of conduction in intercalated carbon pitch-based fibres", *Synthetic Metals*, vol. 31, no. 2, pp. 251–265, 1989.

5. Mildred S. Dresselhaus and Morinobu ER . Endo, *Relation of Carbon Nanotubes to Other Carbon Materials*, vol. 80, Springer, 01/ 2001.

6. Y. Koyama, T. E. Chin, U. Rhyner, R. K. Holman, S. R. Hall, and Y. M. Chiang, "Harnessing the actuation potential of solid-state intercalation compounds", *Advanced Functional Materials*, vol. 16, no. 4, pp. 492–498, 2006.

7. G. A. Kading, P. E. Kladitis, K. M. Bragg, B. Maruyama, and F. L. Vogel, "Intercalated carbon: a novel electromechanical material for mems actuators and microelectronics", *Midwest Symposium on Circuits and Systems*, vol. 48, pp. 143, 2005.

8. M. S. Salib, A. Petrou, and D. D. L. Chung, "Optomechanical actuation using intercalated graphite", *Carbon*, vol. 35, no. 5, pp. 709–711, 1997.

9. Ray H. Baughman, Changxing Cui, Anvar A. Zakhidov, Zafar Iqbal, Joseph N. Barisci, Geoff M. Spinks, Gordon G. Wallace, Alberto Mazzoldi, Danilo De Rossi, Andrew G. Rinzler, Oliver Jaschinski, Siegmar Roth, and Miklos Kertesz, "Carbon Nanotube Actuators", *Science*, vol. 284, no. 5418, pp. 1340–1344, 1999.

10. Inpil Kang, Yun Yeo Heung, Jay H. Kim, Jong Won Lee, Ramanand Gollapudi, Srinivas Subramaniam, Suhasini Narasimhadevara, Douglas Hurd, Goutham R. Kirikera, and Vesselin Shanov, "Introduction to carbon nanotube and nanofiber smart materials", *Composites Part B: Engineering*, vol. 37, no. 6, pp. 382–394, 2006.

11. James R. Gaier, "Technological hurdles to the application of intercalated graphite fibers", Tech. Rep., National Aeronautics and Space Administration. Lewis Research Center, Cleveland, OH., Boston, MA, 1988.

12. James R. Gaier, Melissa E. Slabe, and Nanette Shaffer, "Stability of the electrical resistivity of bromine, iodine monochloride, copper(ii) chloride, and nickel(ii) chloride intercalated pitch-based graphite fibers", *Carbon*, vol. 26, no. 3, pp. 381–387, 1988.

13. Jim Carter, Allen Cowen, Busbee Hardy, Ramaswamy Mahadevan, Mark Stonefield, and Steve Wilcenski, *PolyMUMPs Design Handbook: a MUMPs Process*, 2005.

14. Sumio Iijima, "Helical microtubules of graphitic carbon", *Nature*, vol. 354, no. 6348, pp. 56–58, Nov 07 1991.

15. Gregory T. A. Kovacs, *Micromachined transducers sourcebook*, Wcb, Boston, Ma., 1998.

16. David M. Burns, *Microelectromechanical optical beam steering systems*, PhD dissertation, Air Force Institute of Technology (AU), Wright-Patterson AFB OH, December 1997, (ADA336796).

17. Francis Szabo, *Demonstrating optothermal actuators for an autonomous MEMS microrobot*, MS thesis, School of Engineering and Management, Air Force Institute of Technology (AU), Wright-Patterson AFB OH, March 2004, (ADA426469).

18. A. Metrot and J. E. Fischer, "Charge transfer reactions during anodic oxidation of graphite in h2so4", *Synthetic Metals*, vol. 3, no. 3-4, pp. 201–207, 4 1981.

19. Yoseph Bar-Cohen, *Electroactive polymer (EAP) actuators as artificial muscles: reality, potential, and challenges*, SPIE Press, Bellingham, Wash., 2004.

20. A. P. Graham, G. S. Duesberg, W. Hoenlein, F. Kreupl, M. Liebau, R. Martin, B. Rajasekharan, W. Pamler, R. Seidel, W. Steinhoegl, and E. Unger, "How do carbon nanotubes fit into the semiconductor roadmap?", *Applied Physics A: Materials Science and Processing*, vol. 80, no. 6, pp. 1141–1151, 2005.

21. Mauricio Terrones, "Science and technology of the twenty-first century: Synthesis, properties, and applications of carbon nanotubes", *Annual Review of Materials Research*, vol. 33, pp. 419–501, 2003.

22. M. Meyyappan, *Carbon nanotubes : science and applications*, CRC Press, Boca Raton, FL, 2005, edited by M. Meyyappan.; Includes bibliographical references and index.

23. J. Fraysse, A. I. Minett, O. Jaschinski, G. S. Duesberg, and S. Roth, "Carbon nanotubes acting like actuators", *Carbon*, vol. 40, no. 10, pp. 1735–1739, 2002/8.

24. James R. Gaier, Max L. Lake, Alia Moinuddin, and Mark Marabito, "Properties of hybrid cvd/pan graphite fibers and their bromine intercalation compounds", *Carbon*, vol. 30, no. 3, pp. 345–349, 1992.

25. James R. Gaier, Nora F. Ditmars, and Andrea R. Dillon, "Aqueous electrochemical intercalation of bromine into graphite fibers", *Carbon*, vol. 43, no. 1, pp. 189–193, 2005.

26. G. Dresselhaus M. S. Dresselhaus, "Intercalation compounds of graphite", *Advances in Physics*, vol. 30, no. 2, pp. 139–326, March/April 1981.

27. M. S. Dresselhaus and North Atlantic Treaty Organization. Scientific Affairs Division, *Intercalation in layered materials*, vol. 148, Plenum Press, New York, 1986.

28. Dong Qian, Gregory J Wagner, Wing Kam Liu, Min-Feng Yu, and Rodney S Ruoff, "Mechanics of carbon nanotubes", *Applied Mechanics Reviews*, vol. 55, no. 6, pp. 495–533, 2002.

29. L. Pietronero and S. Strässler, "Bond-length change as a tool to determine charge transfer and electron-phonon coupling in graphite intercalation compounds", *Phys. Rev. Lett.*, vol. 47, no. 8, pp. 593–596, Aug 1981.

30. W. A. Kamitakahara, J. L. Zarestky, and P. C. Eklund, "C—c bond distance and charge transfer in d2so4 – graphite compounds", *Synthetic Metals*, vol. 12, no. 1-2, pp. 301–305, 1985/0.

31. C. T. Chan, W. A. Kamitakahara, K. M. Ho, and P. C. Eklund, "Charge-transfer effects in graphite intercalates: Ab initio calculations and neutron-diffraction experiment", *Phys. Rev. Lett.*, vol. 58, no. 15, pp. 1528–1531, Apr 1987.

32. Allen J. Bard and Larry R. Faulkner, *Electrochemical methods : fundamentals and applications*, Wiley, New York, 2001.

33. Jean-Baptiste Donnet and Roop Chand Bansal, *Carbon fibers*, vol. 10, M. Dekker, New York, 1990.

34. E. Fitzer, K. H. Kochling, H. P. Boehm, and H. Marsh, "Recommended terminology for the description of carbon as a solid", *Pure and Applied Chemistry*, vol. 67, no. 3, pp. 473–506, 1995.

35. A. A. Bright and L. S. Singer, "The electronic and structural characteristics of carbon fibers from mesophase pitch", *Carbon*, vol. 17, no. 1, pp. 59–69, 1979.

36. LaVern A. Starman, *Characterization of Residual Stress in Microelectromechanical Systems (MEMS) Devices Using Raman Spectroscopy*, PhD dissertation, Air Force Institute of Technology (AU), Wright-Patterson AFB OH, April 2002, (ADA402559).

37. Joseph Edward Shigley, Charles R. Mischke, and Richard G. Budynas, *Mechanical engineering design*, McGraw-Hill, New York, NY, 2004.

38. LaVern Starman, "Class handout, EENG 777, Advanced Microelectromechanical Systems (MEMS)", School of Engineering and Management, Air Force Institute of Technology (AU), Wright-Patterson AFB OH, August 2006.

39. Minhang Bao, *Analysis and Design Principles of MEMS Devices*, Elsevier B.V., Netherlands, 2005.

40. Glenn A. Kading, *Piezo-Electrochemical Transducer Effect (PECT) Micro-Electromechanical Actuators*, PhD dissertation, Air Force Institute of Technology (AU), Wright-Patterson AFB OH, not yet published.

41. S H Anderson Axdal and Deborah D L Chung, "Kinetics and thermodynamics of intercalation of bromine in graphite: I. experimental", *Carbon*, vol. 25, no. 2, pp. 191–210, 1987.

42. Yaoming Xie and Peter M.A. Sherwood, "X-ray photoelectron spectroscopic studies of carbon fibers. part xiv: Electrochemical treatment of pitch-based fibers and the surface and bulk structure changes monitored by xps, xrd, and sem", *Applied Spectroscopy*, vol. 44, no. 10, pp. 1621–1628, 1990.

43. Peter M. A. Sherwood, "Surface analysis of carbon and carbon fibers for composites", *Journal of Electron Spectroscopy and Related Phenomena*, vol. 81, no. 3, pp. 319–342, 1996/9.

44. Y.Q. Wang, F.Q. Zhang, and P.M.A. Sherwood, "X-ray photoelectron spectroscopic study of carbon fiber surfaces. 23. interfacial interactions between polyvinyl alcohol and carbon fibers electrochemically oxidized in nitric acid solution", *Chemistry of Materials*, vol. 11, no. 9, pp. 2573–2583, 1999.

45. M. S. Dresselhaus and American Physical Society, *Intercalated graphite : symposium held November 1982 in Boston, Massachusetts, U.S.A.*, vol. 20, North-Holland, New York, 1983.

46. Carol Kozlowski and P.M.A. Sherwood., "X-ray photoelectron spectroscopic studies of carbon-fibre surfaces. iv: The effect of electrochemical treatment in nitric acid", *Journal of the Chemical Society.Faraday transactions I*, vol. 80, no. 8, pp. 2099–2107, 1984.

47. Joel I. Gersten and Frederick W. Smith, *The physics and chemistry of materials*, Wiley, New York, 2001.

48. F. Tuinstra and J. L. Koenig, "Raman spectrum of graphite", *Journal of Chemical Physics*, vol. 53, no. 3, pp. 1126–1130, 19700801.

49. Yan Wang, Daniel C. Alsmeyer, and Richard L. McCreery, "Raman spectroscopy of carbon materials: structural basis of observed spectra", *Chemistry of Materials*, vol. 2, no. 5, pp. 557–563, 1990.

50. P C Eklund, E T Arakawa, J L Zarestky, W A Kamitakahara, and G D Mahan, "Charge-transfer-induced changes in the electronic and lattice vibrational properties of acceptor-type gics", *Synthetic Metals*, vol. 12, no. 1-2, pp. 97–102, 1985.

51. Agilent Technologies, *Agilent 4284A Precision LCR Meter: Operation Manual, Including Option 001, 002, 006, 201, 202, 301*, eighth edition, January 2001.

52. Cytec Engineered Materials, "Typical properties of thornel p-100s continous pitch-based fiber", http://www.cytec.com/business/EngineeredMaterials/CFInternet/cfThornelP-100Spitch.shtm, February 2007.

53. Donald A. Neamen, *Semiconductor physics and devices : basic principles*, McGraw-Hill, Boston, 2003.

54. Glenn A. Kading, LaVern A. Starman, Bryan W. Winningham, Paul E. Kladitis, , Benji Maruyama, and F. Lincoln Vogel, "Intercalated graphite for mems actuation", submitted 05-Jan-07 for consideration to Journal of Microelectromechanical Systems, January 2007.

55. Fibics Incorporated, "Introduction: focused ion beam systems", http://www.fibics.com/FIBBasics.html, February 2007.

56. AFRL, "Technical specifications for the renishaw invia raman microscope", locally compiled information, February 2007.

REPORT DOCUMENTATION PAGE

Form Approved
OMB No. 0704–0188

1. REPORT DATE *(DD–MM–YYYY)*	2. REPORT TYPE	3. DATES COVERED *(From — To)*
22–03–2007	Master's Thesis	Sept 2005 — Mar 2007

4. TITLE AND SUBTITLE

Characterization of Intercalated Graphite Fibers for Microelectromechanical Systems (MEMS) Applications

5a. CONTRACT NUMBER

5b. GRANT NUMBER

5c. PROGRAM ELEMENT NUMBER

6. AUTHOR(S)

Bryan W. Winningham, Capt, USAF

5d. PROJECT NUMBER

5e. TASK NUMBER

5f. WORK UNIT NUMBER

7. PERFORMING ORGANIZATION NAME(S) AND ADDRESS(ES)

Air Force Institute of Technology
Graduate School of Engineering and Management
2950 Hobson Way
WPAFB OH 45433-7765

8. PERFORMING ORGANIZATION REPORT NUMBER

AFIT/GE/ENG/07-25

9. SPONSORING / MONITORING AGENCY NAME(S) AND ADDRESS(ES)

AFRL/IFTA
Attn: Mr. Robert Ewing
1864 4th Street
Suite 1
WPAFB, OH 45433-7131 DSN: 785-6653 X3592

10. SPONSOR/MONITOR'S ACRONYM(S)

11. SPONSOR/MONITOR'S REPORT NUMBER(S)

12. DISTRIBUTION / AVAILABILITY STATEMENT

APPROVED FOR PUBLIC RELEASE; DISTRIBUTION UNLIMITED

13. SUPPLEMENTARY NOTES

14. ABSTRACT

Research was accomplished to characterize the electrical and physical characteristic changes of the Thornel® P-100 carbon fiber and five variants when intercalated with 96% sulfuric acid and incorporated the use of Microelectromechanical Systems (MEMS) structures for testing purposes. The five fiber variants were oxidized in 1 M nitric acid at 0.5 A for 30 seconds, 1 and 2 minutes, the last two samples were detreated at 1150 °C for one hour prior to the nitric acid treatment. The fibers were mounted onto a MEMS die, placed into a chip carrier, sulfuric acid added, the chip carrier sealed and testing accomplished. This thesis explains the approach and methods that were completed to mount carbon fibers. We have designed MEMS structures with an inset trench that 10 μm carbon fibers can be mounted into for testing. Which reduced the amount of coverage required to bind the fiber in place. The original and five anodically oxidized fibers were inspected with a scanning electron microscope (SEM), studied with Raman spectroscopy, and small signal responses were measured from 20Hz to 1 MHz.

15. SUBJECT TERMS

Intercalation; Carbon fiber; Electrochemical processing; sulfuric acid; H_2SO_4; Graphite; MEMS; Microelectromechanical systems

16. SECURITY CLASSIFICATION OF:			17. LIMITATION OF ABSTRACT	18. NUMBER OF PAGES	19a. NAME OF RESPONSIBLE PERSON
a. REPORT	b. ABSTRACT	c. THIS PAGE			LaVern A. Starman, Maj, USAF
U	U	U	UU	135	19b. TELEPHONE NUMBER *(include area code)* (937) 255–3636, ext 4618; lavern.starman@afit.edu